ISTANBUL TECHNICAL UNIVERSITY ★ GRADUATE SCHOOL

HEXAGONAL BORON NITRIDE REINFORCED THERMAL CONDUCTIVITY IMPROVED COMPOSITE MATERIAL DESIGN: APPLICATIONS IN ELECTRIC VEHICLES

M.Sc. THESIS

Emrullah CEBE

Department of Mechanical Engineering

Materials and Manufacture Programme

AUGUST 2024

ISTANBUL TECHNICAL UNIVERSITY ★ GRADUATE SCHOOL

HEXAGONAL BORON NITRIDE REINFORCED THERMAL CONDUCTIVITY IMPROVED COMPOSITE MATERIAL DESIGN: APPLICATIONS IN ELECTRIC VEHICLES

M.Sc. THESIS

Emrullah CEBE
(503211306)

Department of Mechanical Engineering

Materials and Manufacture Programme

Thesis Advisor: Asst. Prof. Dr. Alaeddin Burak İREZ

AUGUST 2024

İSTANBUL TEKNİK ÜNİVERSİTESİ ★ LİSANSÜSTÜ EĞİTİM ENSTİTÜSÜ

HEGZAGONAL BOR NİTRÜR TAKVİYELİ TERMAL İLETKENLİĞİ İYİLEŞTİRİLMİŞ KOMPOZİT MALZEME TASARIMI: ELEKTRİKLİ ARAÇLARDA UYGULAMALARI

YÜKSEK LİSANS TEZİ

Emrullah CEBE
(503211306)

Makina Mühendisliği Anabilim Dalı

Malzeme ve İmalat Programı

Tez Danışmanı: Dr. Öğr. Üyesi Alaeddin Burak İREZ

AĞUSTOS 2024

Emrullah CEBE, a M.Sc. student of ITU Graduate School student ID 503211306, successfully defended the thesis entitled “HEXAGONAL BORON NITRIDE REINFORCED THERMAL CONDUCTIVITY IMPROVED COMPOSITE MATERIAL DESIGN: APPLICATIONS IN ELECTRIC VEHICLES”, which he/she prepared after fulfilling the requirements specified in the associated legislations, before the jury whose signatures are below.

Thesis Advisor : **Asst. Prof. Dr. Alaeddin Burak İREZ** ....
Istanbul Technical University

Jury Members : **Asst. Prof. Dr. Korhan Şahin** ....
Istanbul Technical University

Assoc. Prof. Dr Berkay Ergene ....
Pamukkale Üniversitesi

Date of Submission : 24 May 2024
Date of Defense : 02 August 2024

To my family,

FOREWORD

The successful completion of this MSc. thesis would not have been achievable without the invaluable help and efforts of numerous outstanding persons.

First and foremost, I express my profound appreciation to my family. Their steadfast support and enduring patience have consistently served as a source of motivation throughout this journey.

I would like to express my sincere thanks to my advisor, Dr. Alaeddin Burak IREZ, for his invaluable guidance and for generously sharing his knowledge and experience. His mentorship has significantly contributed to both my academic and personal development.

In addition, I am grateful to Emine Edis, Cem Okan, Ramazan Kaya, Özgür Kalbaran, and Oğuz Ay for their valuable contributions to the successful completion of my thesis.

I wish to express my profound gratitude to ITU BAPSIS for generously providing the financial support that was essential for the successful completion of my research within the framework of the Master's thesis.

August 2024 Emrullah CEBE

TABLE OF CONTENTS

Page

ABBREVIATIONS

PA6 : Polyamide 6
hBN : Hexagonal Boron Nitride
GnP : Graphene Nanoplatelets
SEBS : Styrene-Ethylene-Butylene-Styrene
LIB : Lithium Ion Batteries
BMS : Battery Management System
RSM : Response Surface Methodology
RVE : Representative Volume Element
BEV : Battery Electric Vehicle
HEV : Hybrid Electric Vehicle
FCEV : Fuel Cell Electric Vehicle
PHEV : Plug in Hybrid Electric Vehicle
FTIR : Fourier-Transform Infrared Spectroscopy
DSC : Differential Scanning Calorimetry
DMA : Dynamic Mechanical Analysis
HT : Halpin Tsai

SYMBOLS

$\mathbf{E_c}$	: Elastic Modulus of Composite
$\mathbf{E_m}$	: Elastic Modulus of Matrix
$\mathbf{E_f}$	: Elastic Modulus of Filler
$\mathbf{V_f}$	: Volume Fraction of Filler
$\mathbf{D_f}$	: Diameter of Filler
$\mathbf{t_f}$	: Thickness of Filler
ξ	: Shape Factor
$\mathbf{k_p}$	: Thermal Conductivity of Polymer Matrix
$\mathbf{k_f}$	: Thermal Conductivity of Filler
$\mathbf{d_p}$	: Density of Polymer Matrix
$\mathbf{d_c}$	: Density of Composite
$\mathbf{V_f}$	: Volume Fraction of Filler
$\mathbf{W_f}$	: Mass Fraction of Filler

LIST OF TABLES

Page

LIST OF FIGURES

Page

HEXAGONAL BORON NITRIDE REINFORCED THERMAL CONDUCTIVITY IMPROVED COMPOSITE MATERIAL DESIGN: APPLICATIONS IN ELECTRIC VEHICLES

SUMMARY

Electric vehicles are essential for ensuring the sustainability of transportation and have the advantage of not emitting environmentally detrimental gases due to their lack of reliance on fossil fuels, such as internal combustion engines. Consequently, they provide a significant contribution to the reduction of air pollution. Multiple studies have been conducted to promote the utilization of electric vehicles in order to capitalize on this characteristic. Nevertheless, battery performance remains a significant barrier to wider use. The functioning of batteries leads to an increase in temperature due to the Joule effect, which in turn negatively impacts the efficiency of the battery. Consequently, ongoing research is being conducted on the thermal regulation of batteries, with a focus on the development of materials that can efficiently disperse heat throughout the battery. The objective of the project is to create a polymer-based hybrid composite material that enhances thermal conductivity and impact strength. This material will be used to manufacture battery module casing for electric vehicles. Polyamide 6 (PA6) was chosen as the matrix material because of its extensive usage and ease of fabrication. Hexagonal boron nitride (h-BN) was used to enhance thermal conductivity. Furthermore, a Styrene-ethylene-butylene-styrene (SEBS) elastomer supplement has been included to enhance protection against probable ground impact damage. Furthermore, graphene nanoplate (GnP) was employed to enhance the mechanical and thermal characteristics, so achieving a synergistic effect with the h-BN reinforcing material. Following the production of the compounds through extrusion and injection molding, samples underwent physical, mechanical and thermal characterization.The addition of 30wt.% h-BN increased 38.7% the elastic modulus. The results demonstrate that the thermal conductivity had a significant rise of 194.3% when 30wt.% h-BN. The addition of 2.5wt.% GnPs led to an 8.9% enhancement in the elastic modulus and a 4.97% improvement in the tensile strength value. The addition of 5 wt.% SEBS led to a significant 45% enhancement in the impact strength. Subsequently, a scanning electron microscope (SEM) was employed to examine the cracked surfaces for the purpose of analyzing the mechanisms that cause the damage to the material. Afterwards, the thermal conductivity and elastic constants of the compositions were determined utilizing analytical methods. The Maxwell-Eucken and Cheng-Vachon models were employed for the analysis of thermal conductivity, while the Halpin Tsai (HT) model was utilized to determine the elastic constants. Furthermore, the mechanical and thermal characteristics of these compositions were assessed by creating a representative volume element (RVE) using Digimat FE. To verify the accuracy of these models, they were compared to experimental data. In

the end, the compositions were evaluated based on several qualities which are tensile strength, elastic modulus, impact strength, thermal conductivity, and price to determine the most effective composite that could be used as battery module casing material. The optimization study utilized the response surface method (RSM) in combination with a Python-based optimization tool. Once the most suitable composite material was chosen, it was utilized for the ground impact investigation during the last phase of the study. The investigation was conducted with the simulation software Abaqus CAE. A simulation model was developed to replicate the ground impact, and an analysis was conducted using two distinct situations. In the first situation, an aluminum battery module casing was utilized, while in the second scenario, a battery module casing with a honeycomb structure incorporating PHS30 was employed. By utilizing the honeycomb form of PHS30 battery module casing, a significant weight reduction of 26.9% was attained, while ensuring the integrity of the battery cells in the design.

HEGZAGONAL BOR NİTRÜR TAKVİYELİ TERMAL İLETKENLİĞİ İYİLEŞTİRİLMİŞ KOMPOZİT MALZEME TASARIMI: ELEKTRİKLİ ARAÇLARDA UYGULAMALARI

ÖZET

Son yıllarda fosil yakıt kullanımının yol açtığı yüksek karbon emisyonu küresel bir sorun haline gelmeye başlamıştır. Artan karbon emisyonu, dünya için bir sürdürülebilirlik problemini de beraberinde getirmektedir. Karbon emisyonunu arttıran unsurlar arasında, ulaşım sektörü önemli pay sahiplerinden biridir. Bu oranın yüksek olmasının ana sebebi ulaşımda kullanılan araçların sıklıkla fosil yakıt kullanan, içten yanmalı motorlu araçlar olmasıdır. Bu araçlar çalışma esnasında doğaya yüksek miktarda karbon salınımı yapmaktadır. Yüksek karbon salınımı sonucunda verilen zararı azaltmak amacıyla otomotiv sektöründe köklü değişiklikler meydana gelmektedir. Bu amaçla yapılan majör değişikliklerden biri, içten yanmalı motorlu araçlardan, elektrikli araçlara yapılan geçiştir. Özellikle hükümetler de elektrikli araca geçişi teşvik etmek amacıyla çeşitli ayrıcalıklar sağlamaktadır. Park önceliği, düşük vergi ve vergi muafiyeti gibi çalışmalar bu ayrıcalıklardan bazılarıdır. Otomotiv sektöründe yaşanan köklü değişimler ve sektöre ilişkin alınan kararlarla birlikte otomobil firmaları da yatırımlarını elektrikli araçlara kaydırmaktadır. Piyasadaki büyük firmalar elektrikli araçları geliştirmeye yönelik önemli yatırımlar yapmaktadır. Elektrikli araçlarla ilgili en kritik konularından biri olan batarya teknolojisine yönelik çalışmalar da hızla ilerletilmektedir. Tüm bu durumlar göz önüne alındığında, elektrikli araçların gün geçtikçe önemini daha fazla arttıracağı öngörülmektedir.

Elektrikli araçlar tamamen elektrikli otomobiller (BEV), hibrit otomobiller (HEV), plug-in hibrit otomobiller (PHEV) ve yakıt hücreli otomobiller (FCEV) olmak üzere dörde ayrılmaktadır. Bu araçlardan BEV, araçlarda sıfır emisyon hedefi için en önemli seçenek olarak öne çıkmaktadır. BEV, içten yanmalı motorlu araçlardaki gibi yakıt deposu işlevine sahip, yüksek voltajlı batarya hücreleri kullanır. Birden fazla batarya hücresi bir araya getirilerek batarya modülünü, batarya modülleri bir araya getirilerek batarya paketi oluşturulur. Batarya paketleri, termal yönetim sistemi ve soğutma sistemleri batarya kutusuna monte edilir. Tüm bu sistemlerin bütününe batarya sistemi denir. Bu sistem, elektrikli araçlara gerekli olan enerjiyi depolar. Batarya hücrelerinin uzun süreli kullanımı için şarj edilebilir olması çok önemlidir. Şarj edilebilir bataryaların birçok farklı türü vardır. Yüksek enerji yoğunluğuna sahip olması, şarj edilebilme özelliği ve uzun kullanım ömrü sebebiyle lityum iyon bataryalar (LIBs) endüstride sıklıkla tercih edilmektedir. Lityum iyon bataryalar, yüksek enerji yoğunluğu sayesinde elektrikli araçların çalışma menzilinin arttırılmasında önemli rol oynamaktadır. Çalışma menzili elektrikli araçların yaygınlaşması için gelişime açık konulardan biridir. Daha verimli batarya sistemleri kullanılarak araç menzili arttırılmaya devam etmektedir. Batarya verimliliği ile çalışma sıcaklıkları

arasında doğrudan bir ilişki vardır. Yüksek sıcaklıklara maruz kalan bataryada, Joule etkisi sebebiyle çalışma veriminde düşüş söz konusu olmaktadır. Bu durumunu kontrol altına almak amacıyla, batarya yönetim sistemleri (BMS) kullanılmaktadır. BMS'nin üç temel hedefi vardır: pili olumsuz çevre ve kullanım koşullarından (sıcaklık, nem, toz ve aşırı amper tüketimi gibi) gelebilecek zararlara karşı korumak, pilin ömrünü maksimuma çıkarmak ve pilin işlevsel ihtiyaçlarını karşılamaya hazır olmasını sağlamak. Bu hedeflere ulaşmak için BMS, hücre dengeleme olarak bilinen önemli bir uygulamadan yararlanır. Hücre dengeleme, pildeki tüm hücrelerin aynı voltaj seviyesinde tutulmasını sağlayarak, pilin ömrünün uzatılmasını sağlayan bir özelliktir. Bu teknoloji, aşırı ısınan pilin sıcaklığını düşürmek için havayla soğutma yöntemini kullanır. Ancak ısıl iletkenliği düşük malzemeler için hava soğutması teknik beklentileri karşılamayabilir. Alternatif bir soğutma yöntemi, soğutucu akışkanın kanallar arasında dolaşmasıdır. Bu yaklaşım daha iyi soğutma performansı sağlar ancak daha yüksek maliyeti de beraberinde getirir. Bir batarya sisteminde soğutmayı bir bütün olarak düşündüğümüzde, bataryalar, batarya kutuları ve elektronik bileşenler de dahil olmak üzere tüm bileşenlerin termal iletkenlik özelliği oldukça önemlidir.

Batarya sistemlerinde termal yönetim dışında, batarya modüllerine zarar verebilecek etkenlerin de göz önünde bulundurulması gerekmektedir. Bir objenin batarya sistemine çarpması durumunda bataryaların hasar görmesi söz konusudur. Hasarı minimize etmek için, batarya sisteminin konumlandırılması oldukça önemli bir konudur. Hibrit araçlarda daha küçük boyutlarda bataryalar kullanıldığı için, çarpışma bölgesinden uzak güvenli bir bölgeye konumlandırılması mümkündür. Ancak elektrikli araçlarda daha büyük bataryalar kullanıldığı için bu durum söz konusu değildir. Bataryaların konumlandırılması için farklı yöntemler kullanılmaktadır. Bunlardan ilki T şeklinde bir konumlandırma yapılarak önden ve yandan meydana gelebilecek çarpışmalara karşı bataryanın korunması mümkün kılınabilir. Ancak bu konumlandırma şekliyle sınırlı bir alan kullanılabilmektedir. Batarya modülleri T şeklinde konumlandırıldığında hem batarya kapasitesi, hem de yolcu konforu için bir sınırlandırma söz konusu olacaktır. Diğer bir yöntem ise bataryaların, sürücü ve yolcu koltukları altına yayılı bir şekilde konumlandırılmasıdır. Bu yöntemle daha fazla miktarda batarya montajı yapabilmek mümkündür. Batarya miktarını arttırma sonucunda aracın ağırlık merkezi zemine daha yakın hale gelecektir. Azalan mesafeyle birlikte sürüş esnasında zeminden gelebilecek herhangi bir darbeye daha müsait olma durumu söz konusudur. Hasar unsurlarından zarar görmemek adına, batarya kutusunda kullanılan malzemenin darbe dayanımının yüksek olması gerekmektedir.

Bu çalışma kapsamında batarya modülü muhafazalarında sıklıkla kullanılan alüminyuma alternatif olması amacıyla bir hibrit termoplastik kompozit üzerine çalışılmıştır. Kompozit matrisi olarak, yaygın olarak kullanılması ve üretim kolaylığı sebebiyle poliamid 6 (PA6) seçilmiştir. Termal özelliklerini iyileştirmek amacıyla hegzagonal bor nitrür (h-BN), darbe dayanımını iyileştirmek amacıyla da Stiren-Etilen-Butilen-Stiren (SEBS) kullanılmıştır. SEBS ile PA6 etkileşimini iyileştirmek için Maleik Anhidrit Aşılanmış Polietilen (MAPE) kullanılmıştır. Ayrıca, kullanımı sonucunda diğer takviye malzemesi h-BN ile arasında sinerji yaratabilmek amacıyla hem mekanik özellikleri hem de termal özellikleri iyileştirmek amacıyla grafen nanoplaka (GnP) kullanılmıştır. Oluşturulan kompozisyon tablosuna göre fiziksel, termal ve mekanik karakterizasyonları gerçekleştirmek için standartlara uygun olarak deney numuneleri üretilmiştir. Parçaların fiziksel özelliklerinin belirlenmesi için yoğunluk testi ve Fourier Dönüşümlü Kızılötesi Spektroskopisi (FTIR), mekanik özelliklerin belirlenmesi için çekme testi, üç nokta eğilme testi ve çentikli Izod darbe testleri yapılıp, kırılma yüzeylerinin taramalı elektron mikroskobuyla incelenmesi ve termal özelliklerinin belirlenmesi için Diferansiyel Taramalı Kalorimetre (DSC) dinamik mekanik analiz (DMA), termal iletkenlik testi yapılmışmıştır. Kütlece %30 h-BN eklendiğinde elastisite modülünde %38.7'lik bir iyileşme, termal iletkenlikte ise %194,3'lük önemli bir artış elde edilmiştir. GnP'lerin eklenmesiyle elastisite modülünde %8,9'luk bir artışa ve çekme dayanımı değerinde %4,97'lik bir iyileşmeye sağlanmıştır. SEBS etkisiyle kompozitin darbe dayanımında %45'lik bir iyileşme elde edilmiştir. Ayrıca son olarak termal iletkenliği iyileştirmek amacıyla ara bir yöntem olarak PHS30 ve alüminyum sac ile sandviç geometrisi hazırlanmıştır. Termal iletkenlik değerinde PHS30 kompozisyonuna göre%85.4'lük bir iyileşme elde edilmiştir. Böylelikle projenin ilk aşaması olan, üretim ve deneysel karakterizasyon tamamlanmıştır.

Çalışmanın sonraki aşamasında termal iletkenlik ve elastisite modülü gibi özellikleri mikromekanik modeller yardımıyla analitik olarak ve simülasyon ortamında temsili hacim elemanı (RVE) oluşturularak elde edilmiştir. RVE oluşturmak için bu alanda özelleşmiş Digimat FE programı kullanılmıştır. Elde edilen değerler deneysel verilerle karşılaştırılıp yorumlanmıştır.

Test sonuçlarını değerlendirildikten sonra çekme dayanımı, elastisite modülü, darbe dayanımı, termal iletkenlik ve kompozisyonların birim fiyatı gibi kriterler kullanılarak optimum kompozisyonu bulabilmek amacıyla nesne temelli optimizasyon çalışması yapılmıştır. Yanıt yüzeyi metodolojisi (RSM) ve Python tabanlı bir optimizasyon kodu kullanılarak 2 farklı optimizasyon çalışması yapılmıştır. İki yöntemle de elde edilen sonuçlara göre optimum kompoziyon olarak PHS30 seçilmiştir. En uygun kompozisyon seçildikten sonra, çalışmanın son aşamasında zemin etkisi incelemesinde kullanılmıştır. Bu çalışma Abaqus CAE isimli simülasyon programı kullanılarak gerçekleştirilmiştir. Malzeme tanımlaması yaparken Digimat FE kullanılarak oluşturulan RVE'den elde edilen elastisite modülü, kesme modülü ve Poisson oranı kullanılmıştır. Zemin etkisini simüle edecek şekilde model kurulup iki farklı senaryo üzerinden analiz gerçekleştirilmiştir. İlk senaryoda alüminyum kullanılarak oluşturulmuş bir batarya modülü muhafazası, ikinci senaryoda ise PHS30 kullanılarak oluşturulmuş bal peteği formu eklenmiş bir batarya modülü muhafazası kullanılmıştır. İki senaryo mekanik olarak olarak karşılaştırılmıştır. Elde edilen sonuçlara göre bal peteği formuyla PHS30 kullanıldığı durumda gramaj olarak %26.9'luk bir azalma sağlanarak batarya hücrelerinin hasar görmediği bir tasarım oluşturulmuştur.

1. INTRODUCTION

In recent years, the high carbon emissions resulting from fossil fuel usage have become a global issue. The transportation sector, responsible for 25% of carbon emissions, is a major contributor to this problem [6, 7]. The primary reason for this high percentage is the widespread use of internal combustion engine vehicles, which predominantly run-on fossil fuels, leading to significant CO_2 emissions. Efforts to address this issue in the automotive sector aim to increase sustainability in transportation. One of the key objectives of these efforts is to reduce the carbon footprint caused by CO_2 emissions. One major change undertaken to mitigate this issue is the transition from internal combustion engines to electric vehicles. Governments, in particular, provide incentives to encourage the adoption of electric vehicles, such as priority parking, low taxes, and tax exemptions for electric vehicle owners [8]. An important step towards promoting the use of electric vehicles was taken by the European Union, which announced a ban on the sale of gasoline and diesel vehicles starting in 2035 [9]. In addition, the United Kingdom government has established a goal to completely halt the production of petrol and diesel vehicles starting in 2035 [8]. This decision is expected to increase the utilization of electric vehicles and decrease vehicle expenses, indicating the growing importance of electric vehicles in combating climate change.

Together with radical changes in the automotive sector and sector-related decisions, automobile companies are moving their investments towards electric vehicles. In addition to firms that focus directly on electric vehicles, such as Tesla, Lucid Motor, and TOGG, brands such as Ford, BMW, and Volkswagen are also making significant investments in electric vehicles. With this shift in investment focus, work on battery technology, one of the most critical issues for electric vehicles, is rapidly progressing. TOGG has taken significant steps in this area by opening a vehicle production facility in Gemlik, as well as a battery development and production campus [10].

The battery system is a crucial and indispensable component in an electric vehicle. The vehicle's cost is directly impacted by the battery use. Customers' low-cost expectations for electric vehicles are pushing car manufacturers to produce different types of electric vehicles. As a result, variables such as charging time, driving range, fuel prices, and environmental concerns are taken into account in vehicle production. There are four main types of electric vehicle platforms: battery electric vehicles (BEV), hybrid electric vehicles (HEV), plug-in hybrid electric vehicles (PHEV), and fuel cell electric vehicles (FCEV). Among these, BEV offers the most promising zero-emission transportation technology. In BEVs, energy is stored in high-voltage batteries, and the vehicle's range is directly related to battery performance. Improving this parameter is crucial for the widespread adoption of electric vehicles, and efforts are often focused on the thermal properties of batteries. Battery thermal management systems are used to control the thermal conditions of batteries by adding cooling systems to the battery system. Improving the cooling system of the battery involves considering the thermal properties of the components it interacts with. The thermal conductivity of the material used to produce these components directly affects the cooling performance. The battery module casing, where the battery assembly is located, is one such component, and its thermal conductivity is crucial for cooling performance.

Another method to increase range is to increase the number of battery modules used in electric vehicles. However, increasing the number of battery modules leads to a reduction in passenger space, which may deter consumers. To address this issue, a positioning study for the battery casing can be conducted to reclaim the lost space while increasing the number of battery modules. This reclaimed space can be used as passenger space. However, increasing passenger space may bring the battery module casing closer to the ground due to the added weight, making it more susceptible to external damage. Therefore, the material used for the battery module casing must have high impact resistance to withstand potential damage [11].

In this study, the researchers selected the composite compounds to be produced and mixed the polyamide 6 (PA6) matrix with hexagonal boron nitride (h-BN), graphene nanoplatelets (GnPs), styrene ethylene butylene styrene (SEBS), and maleic anhydride-grafted polyethylene (MAPE) using a twin screw extruder. The resulting composites were produced in granular form. The samples have been manufactured in compliance with the specifications of the scheduled tests using the process of injection molding, utilizing the granules that were collected. Following the manufacturing of the samples, various experimental characterizations were conducted to assess their properties. These characterizations included measuring the density and using Fourier-transform infrared spectroscopy (FTIR) for physical characterization. Mechanical characterization involved conducting three-point bending tests, tensile tests, notched Izod impact strength tests, and microscopic observations. Thermal characterization was carried out through differential scanning calorimetry (DSC), dynamic mechanical analysis (DMA), and thermal conductivity tests. The aforementioned examples demonstrate that previous research has consistently examined the individual impact of h-BN and GnPs on the mechanical and thermal characteristics of polymer composites. Furthermore, studies have been conducted to investigate the impact of incorporating elastomers into the polymer matrix on its strength against impacts. Unfortunately, the author could not find any existing research on the simultaneous utilization of SEBS, GnPs, and h-BN fillers with surface activating agents in polyamide 6 matrix composites. Furthermore, the possible combined benefits of employing many fillers simultaneously in hybrid composites in this manner have not been thoroughly examined. Hence, the objective of this study is to address the existing void in this domain by fabricating composites and conducting empirical analysis.

Following these tests, analytical modeling was employed to identify the thermal conductivity values and elastic constants of composites. The Halpin Tsai (HT) method was used to calculate the elastic constants, while the Maxwell-Eucken and Cheng-Vachon methods were employed to get the thermal conductivity values. Furthermore, the elastic constant and thermal conductivity values of the compositions were determined using the Representative Volume Element (RVE). The results derived from micro-mechanical models were compared to the findings from experiments.

Ultimately, optimization studies were performed to evaluate the composites based on multiple parameters. The optimization investigation identified the most efficient composite material by employing the response surface method and an optimization tool implemented in Python-based algorithm. After selecting the best suitable composite material, it was used for the ground effect investigation in the final stage of the study. The investigation was carried out using the simulation software Abaqus CAE. The material parameters, such as the elastic modulus, shear modulus, and

Poisson ratio, were found by the analysis of the RVE created using Digimat FE. A computational model was developed to replicate the occurrence of the ground effect, and a comprehensive analysis was performed.The study compared the damage status of battery cells in two different scenarios: one with an aluminium battery module casing and the other with a PHS30 battery module casing.

1.1 Purpose of Thesis

The aim of this thesis is to produce and characterize an alternative composite material for battery module casing. Various aspects of the composite have been examined in the study. The lightweight nature of a battery casing is a crucial parameter that impacts the total weight of an electric car significantly. Since the battery occupies the entire middle-bottom section of the car and represents nearly one-third of the total weight, achieving a lightweight design is essential. There are several reasons for opting for a lightweight design. Firstly, a heavy battery casing design necessitates a heavier chassis for the car to bear the increased load, resulting in higher material and manufacturing costs. Additionally, heavier battery casings require larger brakes to stop the car, leading to the need for bigger wheels and other components, further increasing costs. Therefore, weight becomes a parameter that also affects other components. Therefore, the aim in this study is to make improvements on this issue. The increasing weight will result in a higher cost, which will consequently raise the selling price of the electric vehicle. Improvement regarding weight will have a positive impact on cost as well. As a result of reducing weight in battery systems, the reduced cost of chassis and brakes will contribute to lowering vehicle costs, thus making electric vehicles more economically accessible.

Another critical parameter is the thermal properties of an electric car battery unit. The design and material selection of the casing must efficiently dissipate heat generated by the cells to maintain battery efficiency and prolong its lifespan. Failure to manage heat properly can result in thermal runaway, where one overheated cell triggers others, leading to a dangerous increase in heat within the unit that may cause a fire if left unchecked. Moreover, the thermal expansion characteristics of the product are crucial, especially in cold climates, as insufficient tolerances can subject the battery cells to compression due to structural shrinkage, potentially damaging the battery system.

Conversely, a well-designed thermal system should shield the battery cells from extreme environmental conditions. The working temperatures significantly impact battery performance and longevity, highlighting the importance of effective thermal management in battery module casing design.Two distinct filler materials that have a beneficial impact on thermal conductivity were used in this study: h-BN and GnPs. The purpose of the work was to demonstrate how these two filler elements worked in synergy.

Factors that might damage battery modules need to be considered in battery systems in addition to temperature management. The batteries might suffer damage in a collision. Additionally, efforts have been made to reduce the possibility of damage coming from ground impact. Studies to improve the composition's impact strength have been conducted in order to improve the performance of the resultant composite in such circumstances.

1.2 Literature Review

Electric vehicles have become an important option due to their advantageous position in terms of sustainability in transportation. Therefore, electric vehicles, which are increasingly being used with the goal of reducing CO_2 emissions, are crucial for reducing carbon footprint. In a study conducted in Florida, carbon footprint analysis of two vehicles was compared. Two similar-sized vehicles were examined in five stages: raw material production, manufacturing, transportation, operation, and disposal. The study found that the use of electric vehicles would lead to a 22.6% reduction in carbon footprint [6]. In addition to having low carbon emissions, it is also important for electric vehicles to be more affordable in order to become widespread.

High-voltage batteries used in electric vehicles serve as the fuel tank in internal combustion vehicles. The energy required by the electric motor is stored in the battery, so the battery must be rechargeable. There are several types of batteries that are rechargeable. Gaston Plante, a French inventor, created rechargeable batteries in 1859 [12]. Thick-acid batteries are utilized in various applications due to their superior significance compared to their weight and expense. Nickel-cadmium cells, also known as NiCd cells, were developed forty years later than the aforementioned discovery and have since been extensively utilized in low-power applications. An inherent drawback of NiCd batteries is the decline in battery capacity that occurs when they are only partially charged and discharged. This is a phenomenon known as the partial charging and discharging of batteries. These batteries pose a threat to the environment due to their cadmium content. Lithium-ion and nickel-metal-hydride (NiMH) batteries were developed and introduced to the market throughout the 1990s [13]. Lithium-ion cells utilize lithium, the most lightweight metal accessible, as their primary constituent. This feature enhances the power-weight intensity while simultaneously lowering the weight of the battery. Lithium-ion batteries possess advantageous characteristics such as low weight, high energy density, high conversion efficiency, and a long life cycle. Specifically, the chemical composition of intricate metal alloys enables the creation of lithium-ion devices that can be tailored for extended, unique charging and discharge patterns, lasting for several cycles [14]. Due to their high energy density and long service life, electric vehicles often use lithium-ion batteries (LIPs). Due to their high energy density and long-term usability, LIBs are essential for clean and rechargeable energy [15] Producing vehicles using long-range batteries has become a race in the industry. Lucid Air Dream Edition R 685 km, Mercedes-Benz EQS 450+ 635 km, and Tesla Model S Dual Motor 575 km lead this race [16]. Achieving and further improving these levels is only possible by increasing battery efficiency. There is a direct relationship between battery efficiency and operating temperatures. The optimum operating temperatures of batteries range from 15 to 40 C (with a tolerance of 5 C) [17]. If the temperature remains within this range, high temperatures due to the Joule effect negatively affect efficiency in batteries where maximum efficiency is achieved. Therefore, studies are being conducted to thermally improve the battery system and increase battery efficiency [18]. Battery management systems (BMS) are used especially to reduce the effects of this problem in batteries. The BMS has three main tasks: preventing cell damage under unfavorable environmental and usage conditions (temperature, humidity, dust, high amperage draw, etc.), ensuring the longest possible battery life, and ensuring that the battery is ready to meet its functional requirements. To fulfill these tasks, BMS employs a crucial process: cell balancing. Cell balancing is a process that maintains cells in the battery at the same voltage level, extending the battery's life while preserving its functionality for an extended period. Cell balancing is a procedure that ensures all cells in a battery are kept at the same

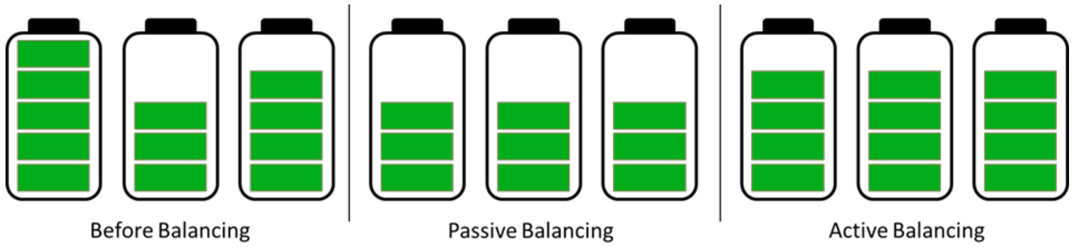

Figure 1.1 : Active and passive cell balancing.

voltage level, hence increasing the battery's lifespan and maintaining its usefulness over a longer length of time [19]. This technology uses a cooling system to lower the temperature of the overheated battery. BMS developers can perform this process actively or passively. In active balancing, cells achieve equal voltage by charging each other, while in passive balancing, cells expend energy through a resistor that generates heat and depletes cells with higher voltage levels. In the case of passive balancing, there is no need for complicated electronic components, but the voltage level of the battery is determined by the cell with the lowest voltage capacity. This situation is illustrated schematically in Figure 1.1. Instead of cooling with air, more effective cooling can be achieved in batteries by circulating liquid through air channels [20]. This approach provides better cooling performance but brings with it a higher cost. Considering the necessity of the cooling phenomenon in the battery system along with the laws of heat transfer, the thermal conductivity coefficient of all components becomes important.

The battery system is formed by the combination of multiple components. Electrodes are located at the lowest level of these components. As shown in Figure 1.2 battery cells are produced using electrodes. In the automotive industry, there are three different types of cell units commonly used in battery cases: Cylindrical, Prismatic, and Pouch type cell units. These three can be produced in various sizes. Cylindrical cells are the most common type of unit cells because they are already widely used in daily life. Computers, remote controls, wall clocks—all powered by cylindrical cells. They are easy to produce, and there is already mass production capacity for them, making cylindrical cells cheaper and more accessible. However, due to their circular cross-sectional area, the packaging efficiency of cylindrical cell battery cases is low. Prismatic cells have higher energy capacity and offer the opportunity to deal with fewer parts during production, reducing the potential for errors. Additionally, the hard

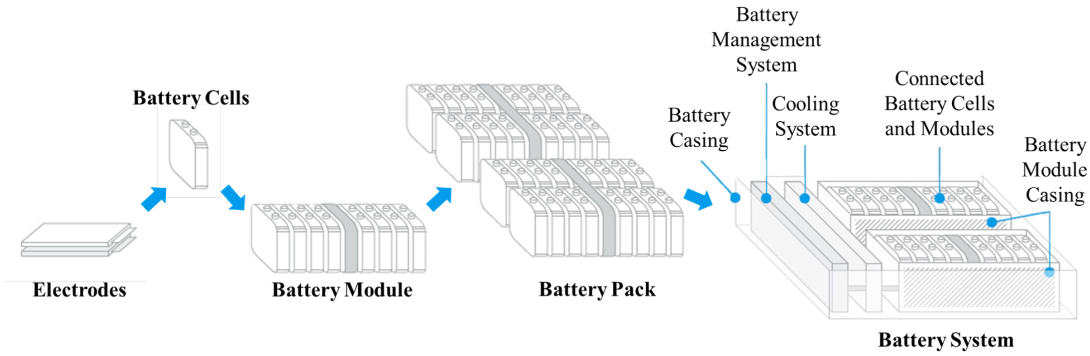

Figure 1.2 : Battery system and its sub-components.

casing used in packaging offers the opportunity to create a more compact design with its rigid shape. Pouch cells have higher energy capacity compared to cylindrical and prismatic cells, and they offer the highest module design flexibility. However, there are concerns due to their cell design. This cell type is relatively new, and there is not enough capacity to satisfy the demand of the automobile industry. After selecting the appropriate battery cell, multiple cells are combined to form a battery module, and a battery pack is created by combining multiple battery modules. Battery modules with battery module casing, thermal management systems, and cooling systems are mounted on the battery casing component. The combination of all these systems is referred to as the battery system. The battery pack serves as the electrical reservoir, and therefore, it is the most susceptible area to heating due to the Joule effect. Cooling systems operated under battery thermal management control are used to cool this area. The cooling system utilizes air channels in battery module casing surrounding the battery modules. By passing airflow through these air channels, it helps reduce the temperature in this area. In addition to air cooling, the thermal conductivity coefficient of the added battery module casing, aimed at enhancing heat transfer, directly affects cooling performance. Therefore, studies are being conducted regarding the material used for the battery module casing. Industry frequently uses aluminium as a material for battery module casing. Aluminium has high thermal conductivity as well as low cost, which makes it significantly fit their design requirements [21]. The material to be used for the battery module casing is expected to have high thermal conductivity and thermal capacity. Additionally, the material's glass transition temperature should be suitable for the battery's operating temperatures. Moreover, the material used should not be flammable or toxic.

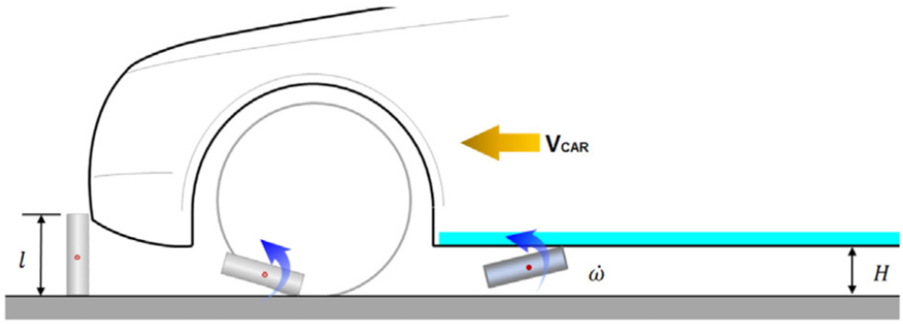

Figure 1.3 : Schematic representation of ground effect [1].

In addition to thermal management in battery systems, factors that could potentially damage battery modules should also be considered. Damage to batteries is possible in the event of a collision. Proper positioning of the battery system is crucial to minimizing damage. In hybrid vehicles, smaller batteries are used, allowing them to be positioned in a safe area away from the collision zone. However, in electric vehicles with larger batteries, this is not the case. Various methods are used to position batteries. One approach is to position the batteries in a T-shape to protect them from front and side collisions. However, this positioning limits the available space. When battery modules are arranged in a T-shape, there will be limitations on both battery capacity and passenger comfort. Another method is to distribute the batteries under the driver and passenger seats. This approach allows for more battery assembly. Nevertheless, as the battery capacity expands, the vehicle's center of mass shifts closer to the ground. As a result, the distance between the vehicle and the ground decreases, making it more susceptible to impacts from the road surface. In this regard, Xia et al. conducted a study to investigate the ground impact on lithium-ion battery packs in electric vehicles. In this study, a hypothetical global finite element model depicted in Figure 1.3 was utilized to develop a general methodology. The model accurately predicted the deformation modes of battery packs during both impact and penetration processes. Additionally, simulations were performed on various configurations, including monolithic plates, plates with polymeric foam foundations, sandwich plates, and their combinations, to assess ground effects. Different scenarios were compared to evaluate the outcomes [1]. Battery module casing is crucial in battery systems in terms of both thermal and mechanical properties. Aluminium is commonly used as the battery module casing material in the industry. Aluminium meets the requirements significantly due to its high thermal conductivity and affordability.

Another requirement is for the battery module casing to be lightweight. Electric vehicles are approximately 300 kg heavier than vehicles with internal combustion engines, primarily due to the battery system [22]. Therefore, using a composite material instead of alumininum would not only provide similar thermal and mechanical properties but also contribute to weight reduction. Composites, consisting of two or more different components brought together to form a superior material, are becoming increasingly common in many industries due to notable advantages. One of the most significant benefits of composites is their low density and exceptional strength-to-weight ratio, making them invaluable in industries where weight reduction is crucial, such as aerospace and automotive [23]. Composites typically consist of a matrix phase (usually a polymer, metal, or ceramic) and a reinforcing phase (such as fibers or particles). This combination allows for the utilization of the outstanding properties of each component, resulting in a material that outperforms its individual components in various aspects. In the industry, polymer materials are predominantly used in their virgin form. Polymers intended to be used as alternatives to aluminium typically require the addition of fillers because their material properties alone are not sufficient. Thus, there are two main types of composites: thermoset and thermoplastic. Thermoset composites generally use matrices such as polyester and epoxy, which are cross-linked and cannot be remolded once cured. On the other hand, thermoplastics can be melted and relatively easily recycled back to their original monomers. Polymers belonging to the polyamide group can be given as examples of thermoplastic materials. Therefore, their reuse is possible [24]. By adding reinforcing materials to the matrix, the electrical, thermal, and mechanical properties of the composite are improved. The properties of the composite are shaped according to the final requirements, depending on the application. In battery casings, thermal conductivity is crucial to mitigate the hazards of the Joule effect. Various studies have been conducted in the literature to enhance thermal conductivity, primarily focusing on reinforcing materials that increase thermal conductivity. Ceramic-based reinforcement materials such as (Al2O3) [25], boron nitride (BN) [26], silica [27], aluminium nitride (AlN) [28]. and carbon-based fillers: carbon fiber (CF) [29], graphite [11], graphene oxide [30]. and carbon nanotube (CNT) [31]. are commonly used as thermally conductive reinforcement materials. Temel conducted a study to investigate the alteration in thermal conductivity in both liquid and solid stages by incorporating 7% of graphene nanoplatelets (GnPs) into paraffin. It was discovered the thermal conductivity of solid and liquid phases increased by 230% and 130%, respectively [32]. Khan et al. conducted a comparative analysis of the thermal conductivity of various carbon-based fillers with different load contents in the polyphenylene sulfide (PPS) matrix. They found that using 30% of the mass resulted in a thermal conductance of 1.94 W/mK, which was greater than that of other carbon-based fillers. It was discovered that utilizing 30 wt% GnPs led to a thermal conductivity of 1.94 W/mK, which is the highest value compared to other carbon-based fillers [33]. Hexagonal boron nitride (h-BN), also known as white graphene due to its similar atomic structure, is another reinforcing material that provides high thermal conductivity. Various studies have examined the thermal performance of h-BN in different types of composites. For example, Meng et al. used 30% silicone rubber and 70% h-BN, increasing thermal conductivity by 400.4% compared to silicone rubber alone [34]. The thermal conductivity of epoxy reinforced with carboxyl-ended polybutadien (CTPB) and h-BN was investigated in a study conducted by Gong et al. The unprocessed group utilized for the surface activation of h-BN was also analysed as a control group in this investigation. Raman et al. discovered that the thermal conductivity of the through-plane was around 5.2 W/mK, which is nearly 20 times more than that of the pristine resin when it contained 60wt.% of h-BN [35]. Due to its layered structure, h-BN forms thermally conductive networks in the polymer matrix and reduces thermal resistance during heat transfer [22]. It is estimated that hexagonal boron nitride (h-BN) has an in-plane thermal conductivity value of approximately 550 W/mK at room temperature [36]. This property makes it an important reinforcing material for increasing thermal conductivity. In a study conducted by Gong and colleagues, the properties of epoxy were modified using cured epoxy, carboxyl-terminated polybutadiene (CTPB), and h-BN, and the thermal conductivity of the modified epoxy was examined. Within this study, two types of h-BN were used: raw and silane-treated. Experimentation was conducted with h-BN quantities ranging from 10% to 40%. The results indicated that by using 40% by mass of raw h-BN, thermal conductivity improved by approximately 200%, while using silane-treated h-BN led to an enhancement of approximately 300% in thermal conductivity. The results obtained from the study are presented in Figure 1.4 [2].

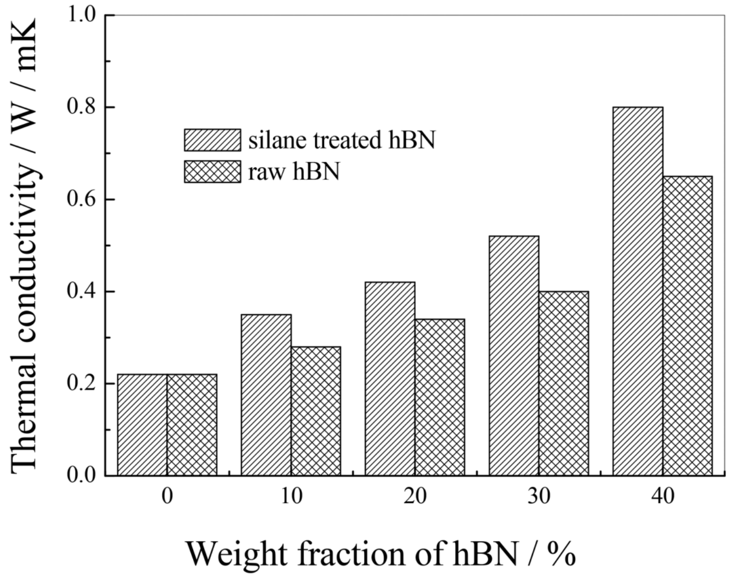

Figure 1.4 : Thermal conductivity of hexagonal boron nitride (h-BN) with epoxy and carboxyl-terminated polybutadiene (CTPB) [2].

During battery assembly, the battery module casing is positioned closer to the ground to regain the area sacrificed in the passenger area. Due to this change, potential damage elements from the ground have become critical. For the battery casing to fulfill its function without being damaged, it must have high impact strength. Various studies have been conducted on reinforcing materials that increase impact strength in composite materials. Gong et al. reported that the elastic modulus of the compound increased as the amount of h-BN increased. When a mass of 40% h-BN was added, the tensile strength of the material decreased by 32% compared to the neat matrix. Similarly, the flexural strength decreased by 47% and the impact strength decreased by 61% [2]. Zhou et al. developed composites by incorporating h-BN (hexagonal boron nitride) into the epoxy at varying mass fractions, ranging from 10% to 50%. They performed experiments to quantify the tensile strength, flexural strength, and impact strength. Based on the acquired data, it was found that h-BN had a detrimental effect on the impact resistance of the composite [37]. SEBS, one of the most commonly used elastomeric materials due to its positive impact resistance, is frequently used. Observations show that the composite's impact damping performance improves when 5% SEBS by mass is used [38]. The study carried out by Savadekar and colleagues exhibited that the addition of 5% to 15% SEBS to poly trimethylene terephthalate led to an improvement in impact strength [39]. In order to address the issue of insufficient interfacial strength when using SEBS alone, maleic anhydride-injected polyethylene (MAPE) is employed to assure intermediate surface activation of SEBS with other materials. Gao and his colleagues discovered that incorporating SEBS, which was modified with 5 wt.% maleic anhydrite, into the thermoplastic polyurethane mixture resulted in a 100% increase in impact strength [40]. Ishak et al. found that mechanical properties decreased when maleic anhydride-grafted SEBS was used in addition to Polyamide 6 (PA6) and polypropylene [41]. Therefore, in this study, efficient nanofillers were used to compensate for the decrease in mechanical properties that occurred as a result of the addition of SEBS. GNPs, when used as a nanoscale filler, improve the mechanical characteristics of polymeric materials by serving as a stiff backbone inside the matrix, owing to their exceptional strength and stiffness [42]. Al-Maqdasi et al. discovered a substantial increase in impact strength by adding 2 wt% GnPs to high-density polyethylene (HDPE), resulting in a maximum improvement of approximately 54% [43]. Okan and his colleagues conducted a study where they found that when s are evenly mixed with the matrix, it enhances the flexural strength and modulus [38]. Suresha et. al. carried out a study investigating how the addition of graphene nanoplatelets (GnPs) affects the physical and mechanical properties of composites made of polyamide 66/thermoplastic copolyester elastomer reinforced with short carbon fibers (SCF). The results indicated that GnPs had a positive effect on tensile strength, flexural modulus, and impact strength [44]. When polymers used in the automotive industry are examined, polyamides form an important group among engineering polymers. Polyamide 6 (PA6) is commonly used in industries such as white goods and automotive, thanks to its ease of manufacture, advanced mechanical properties, and high chemical resistance [45].

After the manufacturing stage, prior to directly proceeding with the production of the battery module casing, preliminary work is conducted. Within this scope, simulations are performed to observe the ground effects. This allows for checking the adequacy of the outputs before any investment in molds. In mechanical simulation studies, introducing the effective mechanical properties of composite materials is crucial. Homogenization is applied to determine the effective mechanical properties of composite materials formed by the combination of multiple materials. There are various approaches for this purpose. One of the most important practices in simplifying complex systems in engineering is modeling. Modeling is achieved by

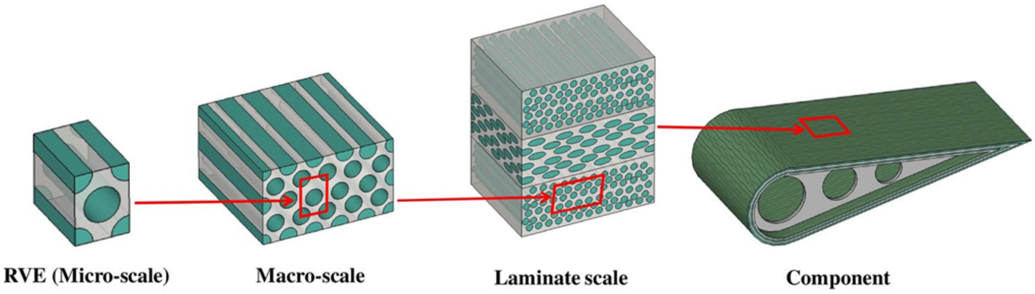

Figure 1.5 : Schematic representation of the derivation of the RVE model [3].

the integrated and balanced use of mathematical and physical models. Representative Volume Elements (RVE) of composites are created to perform homogenization. Due to simplicity reasons, most micromechanical models assume a periodic arrangement where an RVE or unit cell can be isolated. The RVE has the same elastic constants and fiber volume fraction as the composite [46]. The representative diagram of the formation of a two-phase composite component is shown in Figure 1.5.

By using the RVE that reflects microstructure properties, an attempt is made to understand the material's macroscopic behavior. The dimensions of RVE vary depending on the scale of the properties under investigation and the heterogeneity of the material. RVEs are subjected to different loading conditions to determine their mechanical properties.These situations may include biaxial and uniaxial loading [47]. Several commercial software options exist for creating RVE and calculating their effective mechanical properties. Digimat FEA is a software application utilized for material modeling and analysis in the field of simulation. This tool facilitates the comprehension of the behaviors shown by intricate materials, hence enabling the conduction of optimization studies. Its capacity to simulate intricate behaviors of diverse composites renders it suitable for use in numerous sectors [48].

Mechanical properties obtained using RVE are utilized in the finalization of the ultimate product. Determining the specifications, a product needs to meet according to standards in product design is a challenging process. Experimental studies can be employed in this process to ascertain whether a product meets these standards, but such experiments often demand high costs and long lead times. Additionally, traditional strength calculation methods for product designs have become increasingly challenging and time-consuming. However, thanks to advancing technology and processing power, FEA is being employed in designing automobile components.

Designs conducted through FEA result in cost and time savings [49]. Computer-aided analyses have evolved significantly for commercial applications, and calculations by programs are now accomplished in significantly shorter periods thanks to new technologies. In the automotive industry, designs conducted through FEA lead to cost and time savings as well. Furthermore, computer-aided designs reduce the time required to transition products into mass production. Xia et al. conducted a study on the ground impact of lithium-ion battery packs in electric vehicles by using Abaqus CAE. They used a hypothetical global finite element model and cross-validated the force-displacement response during the indentation process [1]. Biharta et al. conducted research on the design and optimization of a sandwich construction that incorporates an auxetic structure. The purpose of this design is to protect the pouch battery system in electric vehicles from ground impact loads [50].

1.3 Scope of the Thesis

This study focuses on researching an alternate composite material for the battery module casing of electric vehicles.The thesis provides a general and simplified summary, which is depicted in Figure 1.6. Initially, The selection of materials for the investigation was established. The PA6 matrix has been selected due to its convenient accessibility and compatibility with extrusion and injection molding techniques. The utilization of h-BN has enhanced the thermal characteristics of the battery module casing. GnPs have been utilized to improve the thermal and mechanical characteristics. Furthermore, the utilization of these two complementary components has been examined to observe the occurrence of synergistic effects when employed in conjunction. SEBS has been utilized to enhance the impact strength characteristics. The utilization of MAPE as a coupling agent has been employed to strengthen the binding structure between SEBS and the matrix. Recipes have been devised by utilizing these materials in varying ratios, followed by commencing the production process. The initial stage of production involves the utilization of a twin-screw extruder to carry out extrusion, which guarantees the thorough blending of the components. The homogeneous material obtained was then utilized in the injection molding process to produce samples for physical, mechanical, and thermal testing. The generated compositions underwent physical tests including density measurement, FTIR. Additionally, mechanical tests such as tensile, three point bending, and impact strength tests were conducted. Furthermore, thermal tests were performed using DSC, DMA, and thermal conductivity tests. Following the completion of the production step, analytical techniques were subsequently employed to ascertain the thermal conductivity and elastic constants of the compositions. The Halpin-Tsai (HT) model was employed for the computation of the elastic constants, while the Maxwell-Eucken and Cheng-Vachon models were utilized for the analysis of thermal conductivity. In addition, the mechanical and thermal properties of these compositions were assessed using Digimat FE to generate a representative volume element (RVE). The accuracy of these models was verified by comparing them with experimental data. Afterwards, a comprehensive optimization study was conducted to determine the optimal mixture. The composition with the greatest score was eventually selected based on an evaluation of various factors pertaining to mechanical and thermal qualities. The optimization process utilized the Response Surface Method (RSM) and a Python-based algorithm. In the concluding phase of the project, the optimal composite material was chosen and utilized for the examination of ground impact. The investigation was conducted using the simulation application Abaqus CAE. The analysis employed two distinct scenarios and developed a simulation model to replicate the ground impact. In the first example, an aluminium battery module casing was utilized, but in the second case, a battery module casing with a honeycomb structure incorporating PHS30 was employed.

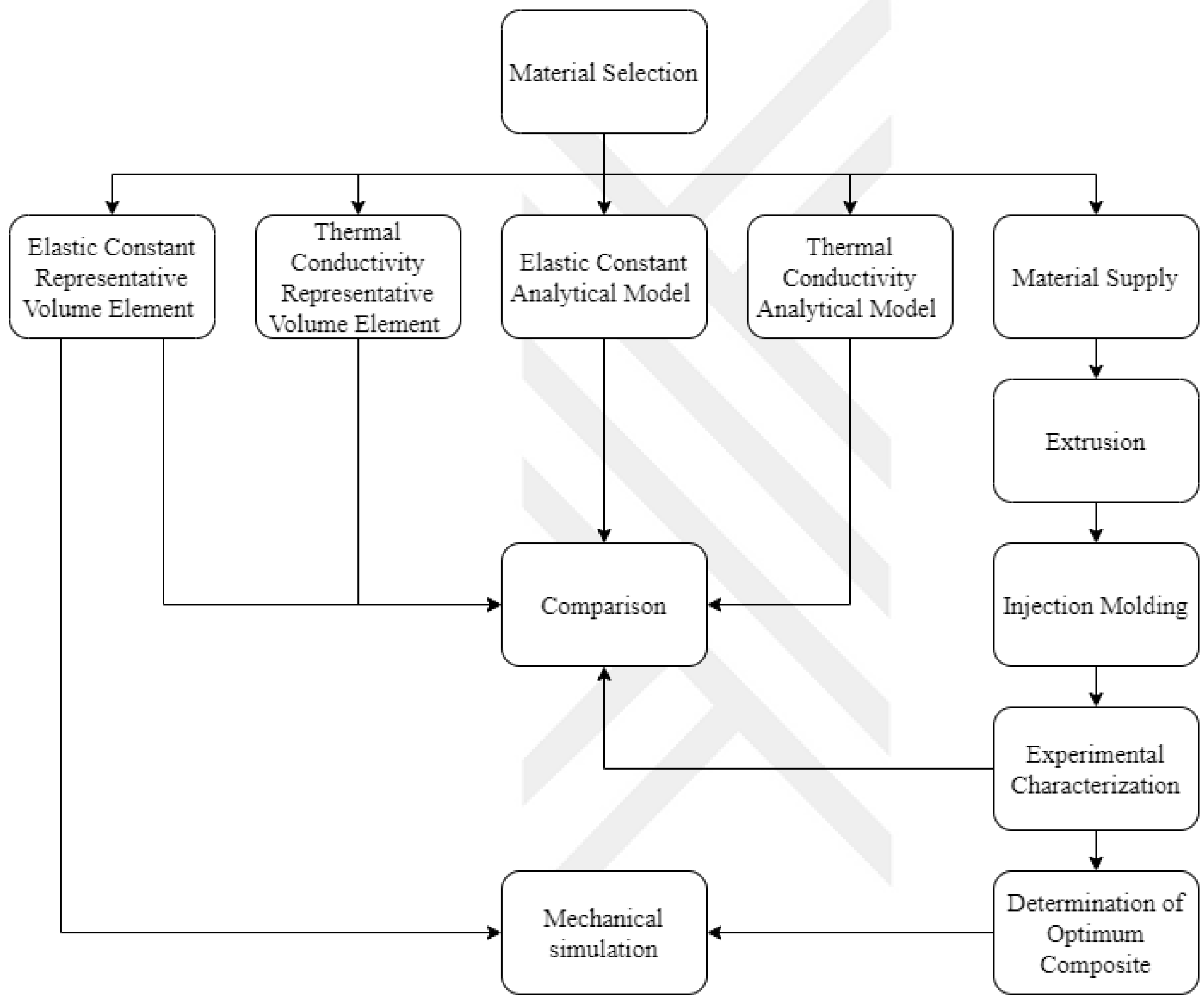

Figure 1.6 : General schematic of thesis.

2. MATERIALS AND METHODS

This section provides details regarding the materials utilized in the thesis study, including the reason for their selection, their specific physical, mechanical, and thermal characteristics, and the origin from which they were supplied. Subsequently, this section clarifies the techniques and equipment employed in the manufacturing process, as well as the procedures used to analyze the resulting samples. As the matrix for the composite material, PA6 has been utilized. Within the composite, three different materials have been employed as fillers. h-BN has been used to enhance the thermal conductivity of the composite material. GnPs have been utilized not only to improve thermal conductivity but also to enhance mechanical properties. To improve impact strength, an elastomeric material named SEBS has been used. Additionally, to enhance the bonding of SEBS with the matrix, a coupling agent named MAPE has been employed. The materials were supplied from reputable companies in the field, ensuring quality and consistency throughout the study. Following material selection, the production process involved specific methods and equipment tailored to composite manufacturing. Subsequently, the produced samples underwent a characterization process to analyze their properties and performance, providing valuable insights into their suitability for the intended application.

2.1 Polyamide 6 (PA6)

Polyamides form an important group among engineering polymers. PA6 is one of the members of this group and is commonly used in sectors such as white goods and automotive. PA6 is a polymer with properties such as processability, ease of manufacturing, and high chemical resistance [45]. These characteristics make it one of the widely used polymers in the engineering polymers group.

PA6 is suitable for extrusion and injection molding methods. Additionally, this material is flame-retardant, with a flame resistance classification of V2 according to the UL94 standard.

The PA6 used in this study was procured from Eurotec under the code NB40 NL FY50. The specifications of the utilized NB40 NL FY50 are provided in the Table 2.1.

Table 2.1 : Properties of PA6.

Property	Standard	Value
Density (g/cm^3)	ISO 1183	1.16
Tensile Strength (MPa)	ISO 527	70
Young's Modulus (MPa)	ISO 527	3250
Izod Notched Impact Strength (kJ/m^2)	ISO 180/1A	6
Flammability	UL94	V2

2.2 Hexagonal Boron Nitride (h-BN)

Hexagonal boron nitride (h-BN) is a two-dimensional material formed by the arrangement of boron and nitrogen atoms into a hexagonal lattice structure. Due to its structural similarity to graphene, it is often referred to as "white graphene" in the literature. It is characterized by its electrical insulation and high thermal conductivity properties. It is particularly utilized for thermal management purposes in electronic systems where effective heat dissipation is crucial and due to its chemical inertness, it is resistant to a wide range of chemicals [51].

The h-BN used in this study was obtained from Nanografi® under the code NG04CO0301. The specifications of the utilized h-BN are provided in the Table 2.2.

Table 2.2 : Properties of h-BN.

Property	Unit	Value
Purity	%	99.7
Size	nm	790
Morphology	-	Hexagonal
True Density	g/cm^3	2.3
Young's Modulus	GPa	14-60
Melting Point	°C	2527
Dielectric Constant	MHz	2.25-3.39
Termal Conductivity	W/mK	29-96

2.3 Graphene Nanoplatelets (GnPs)

Graphene nanoplatelets are formed by the aggregation of numerous layers of graphene. Due to their nanoscale reinforcement, graphene nanoplatelets possess a high surface area [52]. Their high tensile transfer capability, facilitated by the van der Waals bonds and interactions they contain, positively impacts the mechanical strength of composite materials in which they are used [53]. Additionally, their high thermal conductivity makes them suitable for use in thermal management applications. Some characteristic properties include a thermal conductivity of approximately 1.1 TPa Young's modulus, 130 GPa mechanical strength, and 5300 W/(mK) [52]. In order to minimize the likelihood of agglomeration due to high concentrations of graphene, surface-activated GnPs containing COOH were employed [54].

The graphene nanoplatelets used in this study were procured from Nanografi® under the code NG01GNP0109. The specifications of the utilized graphene nanoplatelets are provided in the Table 2.3.

Table 2.3 : Properties of GnPs.

Property	Value
Purity%	99.9
Thickness (nm)	3
Diameter (μm)	1.5
Morphology	Platelet
Relative Density (g/cm^3)	1.9-2.2
Specific Surface Area (m$^2/g$)	14-60
Conductivity (s/m)	1500-1980

2.4 Styrene-Ethylene-Butylene-Styrene (SEBS)

Styrene-Ethylene-Butylene-Styrene (SEBS) is a block copolymer composed of styrene, ethylene, and butylene segments. It is formed by the repetitive arrangement of styrene-ethylene-butylene-styrene monomers.

Elastomers, known for their high energy absorption capabilities, are commonly employed to mitigate the decrease in impact strength. SEBS is a frequently utilized elastomeric material because of its high impact strength.

The SEBS used in this study was obtained from Elastron TR under the code Elastron G401.A82.N. The specifications of the utilized SEBS are provided in the Table 2.4.

2.5 Maleic Anhydride Polyethylene (MAPE)

In this study, MAPE (Maleic Anhydride Polyethylene) was used to improve the interaction between SEBS and PA6 as a coupling agent. MAPE is known for its ability to enhance the compatibility between the matrix and the reinforcement in polymer

Table 2.4 : Properties of SEBS.

Property	Standard	Value
Density (g/cm^3)	ASTM D792	0.89
Tensile Strength at Break (MPa)	ASTM D412	12.5
Young's Modulus %100 (MPa)	ASTM D412	4
Elongation at Break %	ASTM D412	800

blends. By introducing MAPE into the SEBS/PA6 system, it is anticipated that the adhesion and compatibility between the elastomeric SEBS matrix and the rigid PA6 reinforcement are improved, leading to enhanced mechanical properties and overall performance of the composite material.

The MAPE used in this study was obtained from TMB Polymer under the code Elastron ATABOND-1550.

2.6 Compositions of the Composites

In the experimental section of the thesis, the goal was to observe the impact of each filler material used in the composite. Therefore, five different composite samples were prepared. The names and compositions of the prepared composites are provided in the Table 2.5 The first sample was created as a control sample to serve as a baseline, containing 100% PA6. In the subsequent samples, PA6 was used as the matrix in all cases, with the mass percentage of each filler material adjusted accordingly. In

Table 2.5 : Compositions of the composites.

Composition Name	PA6 (wt.%)	h-BN (wt.%)	GnPs (wt.%)	SEBS (wt.%)	MAPE (phr%)
PA6	100	-	-	-	-
PSM	95	-	-	5	5
PHS30	65	30	-	5	5
PHS35	60	35	-	5	5
PHGS30	62.5	30	2.5	5	5

the PSM sample, 5wt.% of SEBS and MAPE were added to observe the effect of SEBS. 5phr.% of SEBS and MAPE was used in all other samples as well. In the third sample, named PHS30, an additional 30wt.% of h-BN was added to assess the effect of h-BN in the composite. With the PHS35 sample, the percentage of h-BN was increased from 30wt.% to 35wt.% to examine the consequences of this change. In the last sample, referred to as PHS30, 2.5wt.% of GnPs reinforcement was added in addition to 30wt% of h-BN. The aim of this sample was to investigate the effect of GnPs in the composite. After determining the sample compositions, the composite production phase commenced.

2.7 Composite Manufacturing

The production process of the composites was carried out in two stages. In the first stage, a twin-screw extruder was used to mix the materials homogeneously and create a compound for each composite. Subsequently, in the second stage, injection molding method was employed to produce the samples using the obtained compounds. The samples were manufactured according to the standards of the tests to be conducted.

2.7.1 Extrusion

The extrusion method is widely employed in the industry to combine two or more materials, particularly for the production of thermoplastic composites. This technique ensures the homogenous mixing of the matrix with reinforcements, such as strength enhancers and colorants.

The core premise of the extrusion process entails the combination and heating of materials within an extruder, then releasing them out the machine in a shaped form. The blending procedure can be conducted utilizing either one or two screws. The necessary heating can be attained by means of friction between the material and the surfaces of the screw, or by utilizing an external heater. The extruder used for extrusion can be divided into three main sections: the feeding zone, where the material is introduced; the melting zone, where the material is mixed and heated until it melts; and the die zone, where the homogeneously mixed material is extruded out of the machine in a profile shape. In the end, the resulting profile is sliced to achieve a uniformly blended content in the form of granules.

The Leistritz ZSE 27 MAXX, a twin-screw extruder, was utilized in the initial phase to achieve uniform mixing of constituents. The twin screw extruder used has a screw diameter of 28.3 mm, a pitch of 28.5 mm, and a screw length of 48 times the screw diameter. The twin-screw extruder contains a total of 11 barrels. The temperature in the initial barrel is 45 °C, while in the subsequent barrels, the temperature ranges from 210 to 280 °C. The nozzle temperature ranges from 260 to 280 °C, depending on composition. Technical specifications provided in the Table 2.6, was used.

Table 2.6 : Technical specifications of the twin-screw extruder.

Property	Value
Screw Diameter (mm)	28.3
Barrel Diameter (mm)	28.5
Screw Length (mm)	1358.4
Drive Power (kW)	33.8
Maximum Motor Speed (rpm)	2400
Maximum Screw Speed (rpm)	1200

2.7.2 Injection molding

Injection molding is a manufacturing method where thermoplastic and some thermoset materials are melted and injected into a mold to obtain the final part. It is commonly used in industry due to its suitability for mass production. Injection molding allows for the production of low unit cost, short cycle time, low scrap generation, and high dimensional accuracy parts. However, disadvantages of plastic injection molding include high setup and machine part costs.

The injection molding machine consists of two distinct units: a clamping unit and an injection unit. The primary operations performed by the clamping unit include the act of both opening and shutting a die, as well as the ejection of materials. The primary functions of the injection unit are to thermally melt plastic and subsequently introduce the melted plastic into a mold.

The manufactured compounds were used for production in the second stage, employing the Bole BL90EKH/C220 injection molding machine. The plastic injection machine employs a screw with a diameter of 28.4 units and a screw length-to-diameter ratio of 20. The temperature range for the melting furnace during injection was set at 205 to 210 °C. Technical specifications provided in the Table 2.7, was used.

Table 2.7 : Technical specifications of the injection molding machine.

Property	Value
Screw Diameter (mm)	28.3
Screw L/D Ratio	20
Theoretical Injection Capacity (cm^3)	129
Shot Weight (g)	118
Injection Pressure (MPa)	177
Maximum Injection Speed (g/s)	162
Maximum Screw Speed (rpm)	331

2.8 Experimental Characterization of Manufactured Composites

After the production stages were completed, characterization was conducted on the obtained test specimens. Density measurement, Fourier transform infrared spectroscopy (FTIR), three-point bending test, tensile test, and Izod impact strength test, differential scanning calorimetry (DSC) analysis, dynamic mechanical analysis (DMA), and thermal conductivity test were performed on the samples. All tests were conducted at room temperature. The densities of the materials have been measured according to ISO 1181-1. The MatsuHaku GP-300E model instrument was employed for the density measurement. FTIR is used to examine the molecular composition and chemical bonds of materials. This method involves the examination of vibrations corresponding to different vibration modes absorbed by the chemical bonds of molecules. During the analysis, infrared light is sent to the sample, and the absorbed and transmitted light is detected. The obtained spectrum provides information about the chemical composition of the material. The FTIR analyses were performed using a BRUKER Alpha Platinum ATR-type device. The three-point bending test was conducted at a velocity of 50 mm/min using specimens manufactured following the ISO 178 standard (length: 80 mm, width: 10 mm, thickness: 4 mm). Beam-shaped specimens are placed on support points from two end points. Load is applied from the midpoint on the top. The purpose of this test is to determine the bending behavior and strength of the material. As a result of the test, the flexural strength, flexural modulus, and strain at break values of the material are determined. The Hegewald & Peschke model testing machine was used for the three-point bending test. Three sets of samples were used to conduct the three-point bending test for each composition. The tensile test was performed at a consistent rate of 50 mm/min by applying force to a dogbone-shaped sample manufactured in accordance with the ISO 527 standard, as depicted in Figure 2.1. The goal of the tensile test is to ascertain the material's level of resistance to tensile force. Consequently, the exam measures and records the levels of stress and strain. This data is utilized to derive the stress-strain curve of the material. This curve facilitates the estimation of the material's elastic modulus, tensile strength, and elongation at break values. The Hegewald & Peschke type testing machine was utilized for conducting the tensile test. For each composition, three sets of samples were utilized to carry out the tensile test. The Izod impact

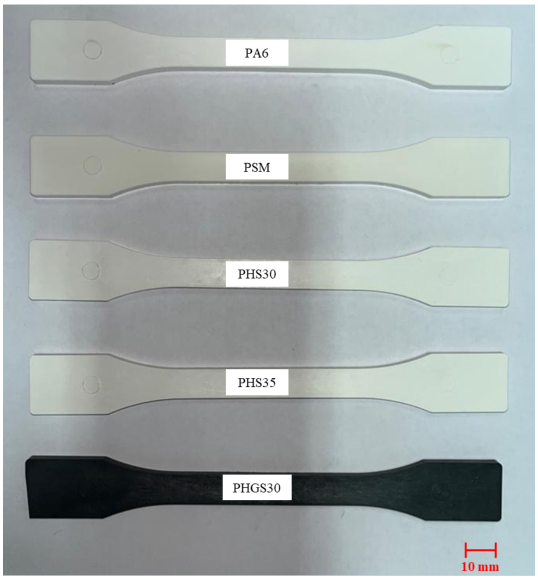

Figure 2.1 : Dogbone-shaped tensile test specimens (ISO 527) [4].

strength test was conducted with specimens conforming to ISO 180 standard, as shown in Figure 2.2. The Izod impact test varies depending on whether the specimen is notched or unnotched. In this study, a notched Izod impact strength test was performed. During the test, an impact hammer is used. The hammer is released freely, and the specimen is fractured. The impact strength of the material is determined by examining the amount of energy lost in the hammer. The notched Izod impact strength test was conducted using the Instron Ceast 9050 model testing machine. Three sets of samples were used to conduct the notched Izod impact strength test for each composition. Following the completion of the mechanical characterization, Tescan Vega 3 scanning electron microscopy (SEM) was used to investigate the fracture surfaces of the failed samples. DSC is a technique used to examine the thermal properties and behavior of a material. The prepared sample is being compared to a reference sample. The DSC device allows for control of the temperature difference between two samples by adjusting the temperature either upwards or downwards. The device provides a graph that illustrates the temporal variations in temperature. This graph facilitates the identification of the melting, crystallization, and glass transition temperatures of the material.The instrument produced a heat flux-temperature curve, illustrating the variation of thermal energy with temperature. To determine the glass transition temperature using this curve, draw a line connecting the starting and ending points of the region where the slope visibly changes for the first time, starting from room temperature. The temperature corresponding to the midpoint of this line on

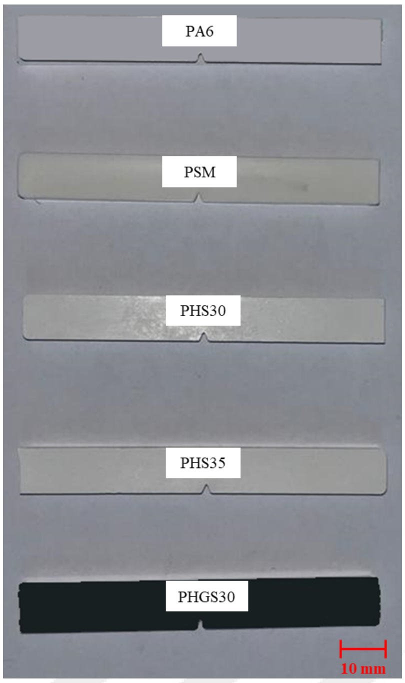

Figure 2.2 : Notched Izod impact strength test specimens (ISO 180) [5].

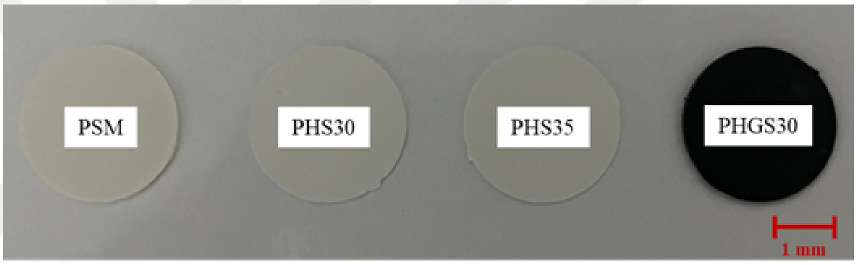

Figure 2.3 : Thermal conductivity test specimens.

the curve is the glass transition temperature. DMA is performed to determine the thermomechanical properties of materials using a TA Instruments Q800 system. The experiment utilized the single cantilever bending mode, and data was gathered at a frequency of 1 Hz with a strain of 0.1% in the temperature range of 45°C to 130°C. The dimensions of the samples were 10 mm in width, 60 mm in length, and 3 mm in thickness [55] The glass transition temperature (T_g) of the material is determined from this analysis. To find the T_g value, the temperature at which the tan value peaks can be examined. The thermal conductivity test was conducted on disc-shaped samples, as shown in Figure 2.3. Samples have a diameter of 25.4 mm and a thickness of 1 mm. The thermal conductivity test was conducted using the TA-Discovery Xenon Flash DXF 200 model test instrument. Three sets of samples were used to conduct the thermal conductivity test for each composition.

3. EXPERIMENTAL CHARACTERIZATION OF COMPOSITES

This section presents the experimental characterizations that were conducted as part of the investigation. The characterizations were analyzed based on three categories: physical, mechanical, and thermal. In the physical characterization section, the results of density measurement and FTIR were presented. In the mechanical characterization section, the results of the three-point bending test, tensile test, notched Izod impact strength test and SEM results were shared. Lastly, in the thermal characterization section, the results of , DSC, DMA and thermal conductivity tests were presented.

3.1 Physical Characterization

In this section, the results and interpretations of the conducted physical characterizations are presented. The density measurement and FTIR applied to composites under the category of physical testing have been outlined.

3.1.1 Density measurement

The densities of the produced samples were measured according to ISO 1181-1 standard. The obtained results are as shown in Table 3.1. The density of sample

Table 3.1 : Density of the composites.

Sample Name	Density (g/cm³)
PA6	1.16 ± 0.01
PSM	1.12 ± 0.01
PHS30	1.25 ± 0.02
PHS35	1.27 ± 0.02
PHGS30	1.27 ± 0.03

PA6, which was produced using only PA6, was measured as 1.16 g/cm³. In sample PSM, where 5wt.% SEBS was added, the density decreased due to the addition of SEBS. An increase in density was observed in samples PHS30 and PHS35, where 30wt.% and 35wt.% h-BN were used, respectively. However, there was no significant change in density in sample PHGS30, where 2.5wt.% GnPs was used, likely due to the lower proportion of GnPs. The observed variations in densities are typically directly proportional to the densities and mass ratios of the supplements that are added.

Theoretical density values for the compositions were determined as 1.16, 1.15, 1.49, 1.55, and 1.52 g/cm³ for PA6, PSM, PHS30, PHS35, and PHGS30, respectively. The obtained values exhibit a comparable relationship with the theoretical values in terms of both increase and decrease.

3.1.2 Fourier-transform infrared spectroscopy (FTIR)

After conducting density measurements, three groups, namely PSM, PHS30, and PHGS30, were subjected to FTIR analysis and Figure 3.1 displays the results. From the obtained graphs, it is clear that all composites have similar characteristic bands. The bands are located at 2916 cm¹ (C-H), 1636 cm¹ (Amide I, C=O stretching), and 1535 cm¹ (Amide II, N-H bending). The presence of hydrogen bonding within the molecular chains is shown by the different bands observed in PA6 [41]. Upon comparing the analysis results of groups PHS30 and PHGS30, it was observed that both samples exhibited a peak at a wavelength of 1400 $cm^{-}1$. Covalent bonding between the h-BN filler material and the composite matrix has been confirmed [56].

3.2 Mechanical Characterization

In this section, the results and interpretations of the conducted mechanical characterizations are presented. The the three-point bending test, tensile test, notched Izod impact strength test, and SEM applied to composites under the category of mechanical characterization have been outlined.

3.2.1 Three point bending test

In order to ascertain the mechanical characteristics, a series of three-point bending tests were conducted on five different compositions: PA6, PSM, PHS30, PHS35, and PHGS30. The test provided measurements for the flexural strength, flexural modulus, and strain at break of the materials. The resulting values are presented in Table 3.2. Due to the low strength and stiffness properties of the SEBS material, which is characterized by its rubber-like nature, the composite experiences a 39.6% reduction in flexural strength, a 55.9% reduction in flexural modulus, and a 19% increase in strain at break, as reported in reference [38]. By including 30wt.% h-BN, the composite exhibited a significant improvement in its properties. Specifically, there was a 22%

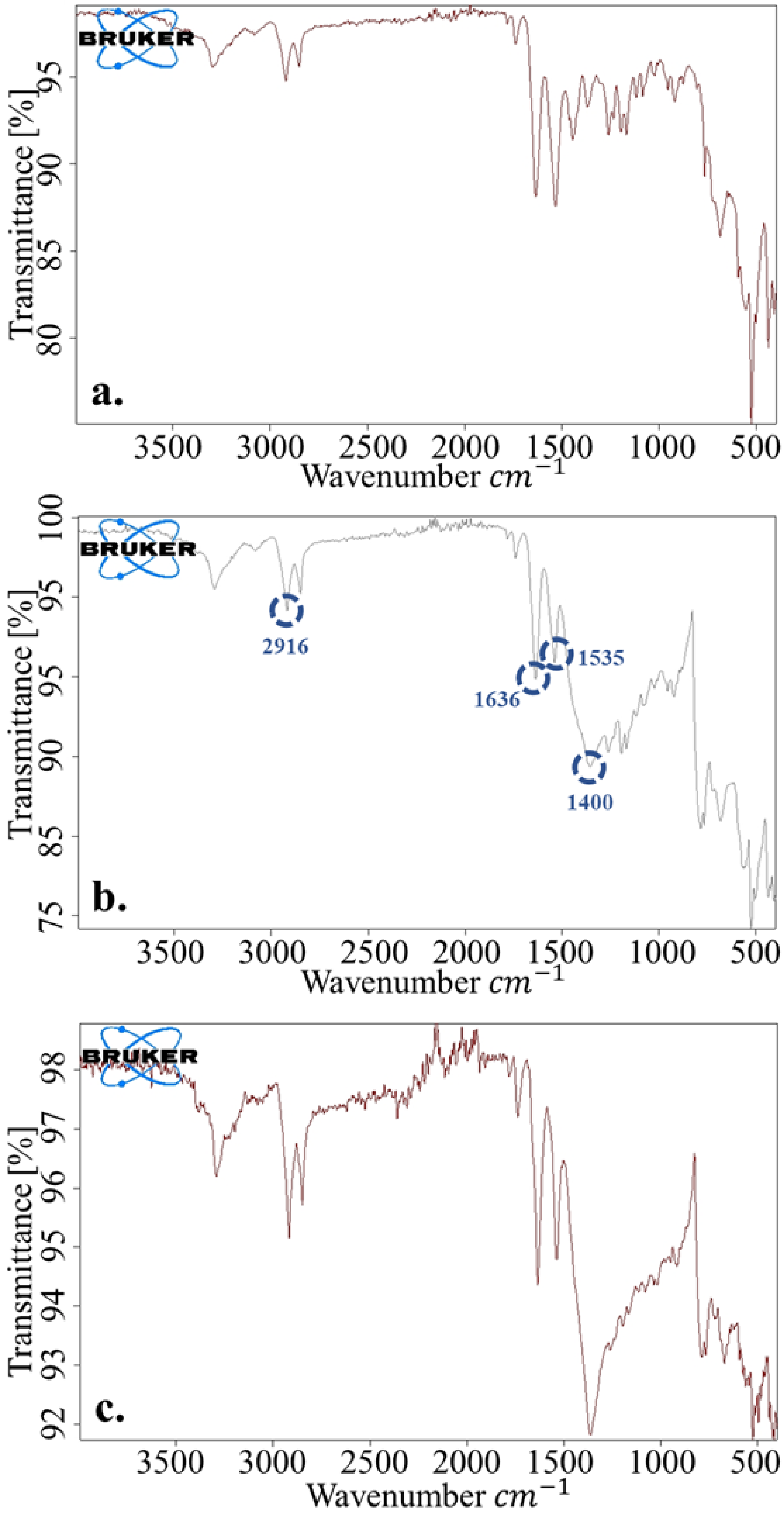

Figure 3.1 : FTIR results of (a) PSM, (b) PHS30, and (c) PHGS30.

Table 3.2 : Flexural strength, flexural modulus and strain at break values of the composites.

Composition Name	Flexural Strength (MPa)	Flexural Modulus (MPa)	Strain at Break (%)
PA6	88 ± 0.3	2749 ± 35	20.94 ± 0.04
PSM	53.13 ± 1.7	1210.99 ± 50	24.98 ± 0.12
PHS30	64.83 ± 0.73	2435.41 ± 68.96	7.72 ± 0.05
PHS35	59.95 ± 0.17	2418.35 ± 56.60	7.37 ± 0.16
PHGS30	74 ± 0.6	3789 ± 60	5.53 ± 1.01

increase in flexural strength, a 101.1% rise in flexural modulus, and a 69% decrease in strain at break compared to the PSM composition. According to PSM, when 35wt.% of h-BN was utilized, the composite showed a 12.8% increase in flexural strength, a 99.7% rise in flexural modulus, and a 70.4% drop in strain at break. This growth can be primarily due to multiple factors. The primary elements that impact the strengthening of the composite material are the ratio of hBN length to thickness, the dispersion of hBN particles, the efficient transmission of stress between hBN and the polymer, and the orientation of hBN within the nanocomposite matrix. The transfer of stress between hBN and polymer materials is a crucial characteristic for ensuring the efficient transmission and distribution of the externally imposed load [57]. In addition, the presence of robust covalent connections within the h-BN layers and the interactions between BN and the polymer, such as van der Waals forces, facilitate the efficient transfer of stress from the polymer matrix to the h-BN. This delays the formation of cracks and enhances the flexural strength of the material [58]. However, the decrease in flexural strength is attributed to the formation of hBN clusters (agglomeration) resulting from the increased amount of hBN from 30wt.% to 35wt.% (see Figure 3.4) [59, 60]. The decrease in the unit strain at break, attributed to the influence of hBN, is believed to be a result of the brittle nature of hBN [59]. When 2.5wt.% GnPs were added, the composite exhibited a 14.1% increase in flexural strength, a 55.6% rise in flexural modulus, and a 25% decrease in strain at break. When polymeric materials are strengthened with rigid inorganic particles, these particles serve as a structural support inside the matrix. The introduction of interfacial reinforcing agents during manufacturing restricts the molecular chain movement of the polymer through the formation of physical cross-links between the matrix and GnPs. This leads to an increase in the stiffness of composite materials [61]. When using thin, plate-like inorganic particles (such as GnPs) to reinforce a material, the matrix will experience deformation in relation to the particles, while the particles themselves will stay undeformed due to their great strength. Consequently, the interface that is at a right angle to the load will sustain the tensile force, whereas the contact that is parallel to the load will sustain the shear force. Due to the increased surface area of nano reinforcements, the stress within the internal structure, which is the force per unit area, will decrease. As a result, the composite material will exhibit greater strength without fracturing [62, 63]. A study found that the incorporation of varying amounts of graphene nanoplatelets (GnPs) with poly(lactic acid) (PLA) resulted in a reduction in the strain at break value [64]. Similarly, this study reported a reduction in this parameter upon the introduction of GnPs.

3.2.2 Tensile test

Tensile tests were conducted on five samples, namely PA6, PSM, PHS30, and PHGS30, in accordance with ISO 527-2 standard. These tests were used to obtain stress-strain curves in Figures A.1 and A.2 for the composites. The obtained curves can be found in Appendix A. Based on these curves, the tensile strength, elastic modulus, and elongation at break values were determined and are presented in Table 3.3. SEBS, a type of highly flexible rubbery particle, can improve the stretch ability of

Table 3.3 : Tensile strength, elastic modulus, and elongation at break values of composites.

Sample Name	Tensile Strength (MPa)	Elastic Modulus (Mpa)	Elongation at Break (%)
PA6	59.95 ± 0.33	2925.65 ± 231.17	32.17 ± 0.37
PSM	50.89 ± 0.16	2322 ± 225.55	51 ± 6.62
PHS30	47.77 ± 0.33	3187.95 ± 102.86	4.26 ± 3.83
PHS35	50.82 ± 0.4	1745.15 ± 210.94	5.09 ± 0.76
PHGS30	49.81 ± 1.49	3508.54 ± 313.23	1.66 ± 0.34

composites when there is strong compatibility between the constituents [65]. Based on this assumption, the modification of the matrix with SEBS led to a rise in the elongation at break of the composites while concurrently decreasing the tensile strength. In addition, the low stiffness of the SEBS resulted in a reduction in the elastic modulus of the composites, as indicated by the findings of the PSM group.

The addition of composite h-BN led to a significant 38.7% increase in the elastic modulus. The primary reason for its expansion can be ascribed to a multitude of variables. The primary determinants that impact the reinforcement efficiency of the composite are the aspect ratio of h-BN (the ratio of its length to thickness), the dispersion of h-BN, the interface between h-BN and the polymer, and the alignment of h-BN within the nanocomposite matrix. The interface between h-BN and polymer materials is a crucial factor that ensures the stress transfer from the matrix to h-BN when the external load applied [57]. Moreover, the strong covalent bonds between the h-BN layers and the interactions between the BN and the polymer, such as van der Waals forces, induce a delay in the formation of cracks. This delay facilitates the effective transmission of stress from the polymer's matrix to h-BN [58]. However, the elastic modulus experienced a decrease as a consequence of the agglomeration of h-BN, which occurred due to the increase in the h-BN from 30wt.% to 35wt.% [59,60]. The reduction in elongation at break caused by the influence of h-BN can be attributed to the brittleness of the h-BN [59].

GnPs led to an 8.9% increase in the elastic modulus and a 4.97% enhancement in the value of tensile strength. GnPs, with their high elastic modulus, can increase the elastic modulus of composites when they are evenly dispersed. When hard inorganic particles are introduced into the polymer, the physical cross-links between the matrix and the GnPs limit the motion of molecular chains, leading to increased stiffness of the composite materials [66]. The tensile strength of polymer composites reinforced with inorganic particles is strongly influenced by the interfacial adhesion between the inclusions and the matrix. The adhesion between composites under tensile loading is primarily influenced by the lateral area of thin sheet-like inorganic particles, such as GnPs. This area is dictated by the length and width of the particle, which lies between the matrix and the inclusions. When a polymer composite with thin sheet-like inorganic reinforcement is pulled, the matrix will undergo deformation with regard to the particles, while the particles themselves will remain unchanged in shape. The interface that is perpendicular to the load will experience the tensile force, whereas the interface that is parallel to the load will experience the shear force. Therefore, if the particle has a bigger specific surface area, the composite will have higher strength given the same interfacial bonding condition [66].

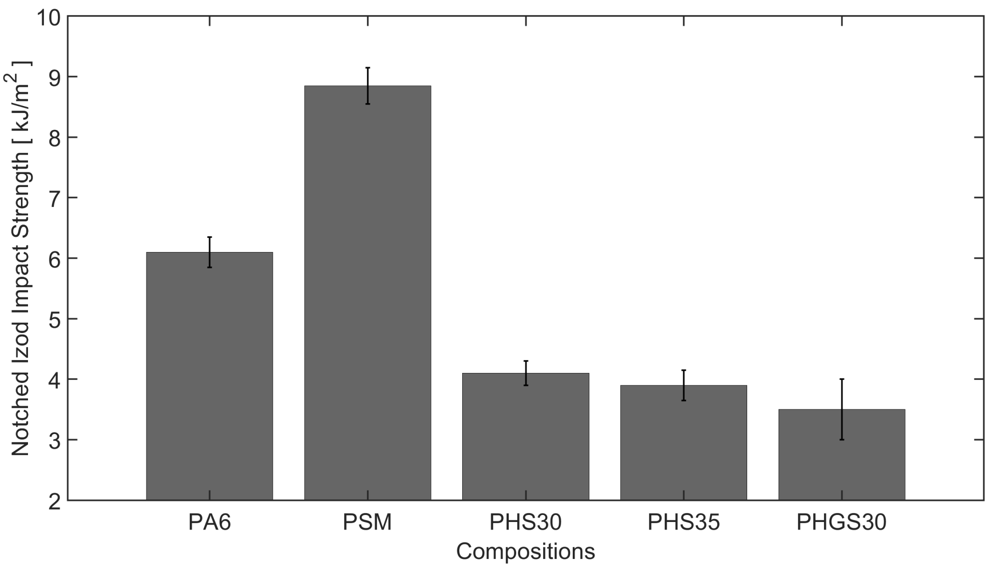

Figure 3.2 : Notched Izod impact strength test results.

3.2.3 Notched izod impact strength test

Notched Izod impact strength tests were conducted on five samples, namely PA6, PSM, PHS30, and PHGS30, following ISO 180 standard. The obtained values are depicted in Figure 3.2. According to the results, the use of SEBS resulted in a 45% increase in the impact strength of the composite. Since SEBS is an elastomeric material, it positively influenced the amount of energy absorbed during impact [38]. When 30% h-BN was used, there was a 53.6% decrease in impact strength, and with 35% h-BN, a 55.9% decrease was observed. h-BN, not being an elastomeric filler material, caused the composite to become more brittle [59]. It was also observed that the increased amount of h-BN reduced the impact damping property of the composite. In composites where GnPs was used, better stress transfer is achieved, thereby positively affecting the composite's capacity to dampen impacts [42]. In this study, the use of 2.5% GnPs resulted in a 14.6% decrease in impact strength. This decrease is believed to be due to the heterogeneity within the composite sample. If a better interface quality is achieved between GnPs and the matrix, it could contribute to higher energy absorption.

3.2.4 Scanning electron microscope (SEM)

After mechanical tests, scanning electron microscopy (SEM) analysis was conducted in order to support the hypotheses put forth during the interpretation of the experimental results. Fracture surfaces provide evidence that the elongation at break is greater in PSM group, as illustrated in Figure 3.3. This surface is rough and comprises irregularly elongated regions. Surface irregularities indicate the presence

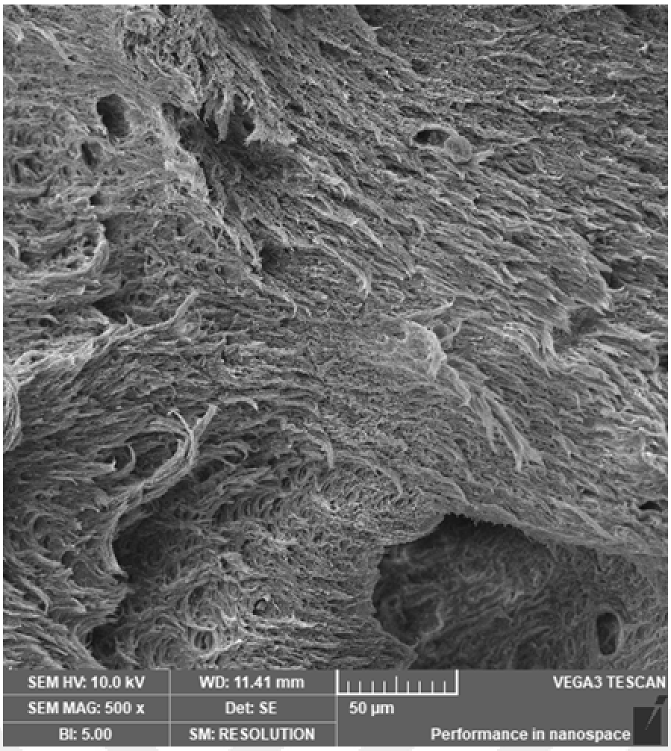

Figure 3.3 : Fracture surface of PSM composition.

of a fracture type that can withstand stretching without breaking, as well as a larger extent of stretching preceding failure. In the field of fracture mechanics, the presence of rough surfaces indicates a more substantial surface area, and the production of further surfaces requires a greater amount of surface energy. The energy present in the initial fissure is counterbalanced by strain energy, which reduces the available energy for its further propagation and ultimately leads to fracture. As a result, the failure of the sample is delayed, causing an increase in the stress at which it ultimately fractures. Furthermore, the elongated sections, namely the elongated fracture patterns or fibrils depicted in Figure 3.3, indicate that ductile damage is occurring inside the matrix as a result of localized plastic deformation [67]. Figure 3.4 displays an image obtained from the fracture surface of the PHS35 sample. The figure shows a localized accumulation of thin plate-shaped h-BNs, shown by red arrows, in a limited area. The existence of these clusters causes the build-up of tension and can lead to the development of micro cracks in the adjacent regions of the h-BN clusters. Under stress, tiny cracks known as micro cracks can propagate and result in early damage, resulting in a reduction in the structural integrity of composites.

Figure 3.5 presents the SEM picture of the PHS30 group at comparable magnifications. The image displays hBNs, which are highlighted by green arrows. However, the image

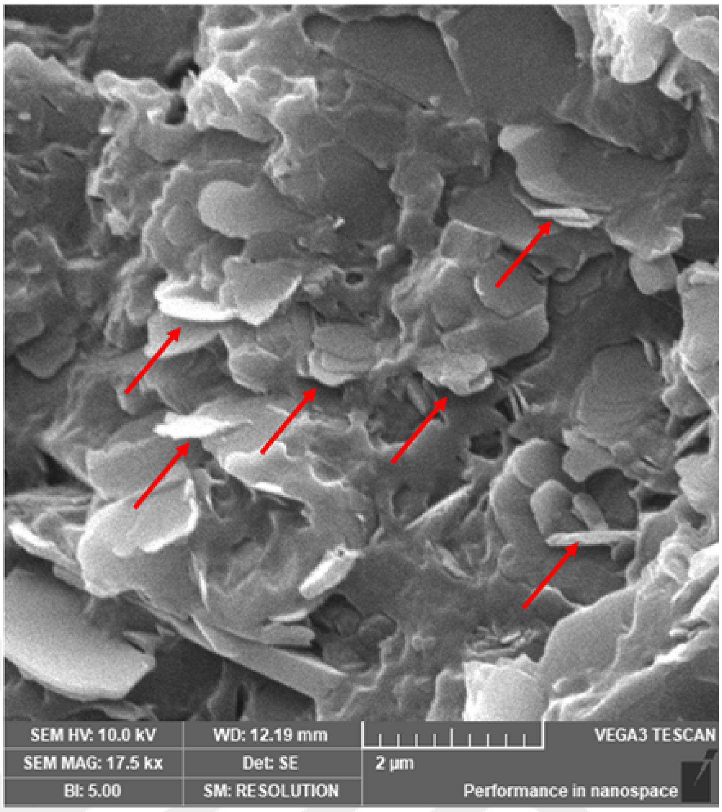

Figure 3.4 : Fracture surface of PHS35 composition.

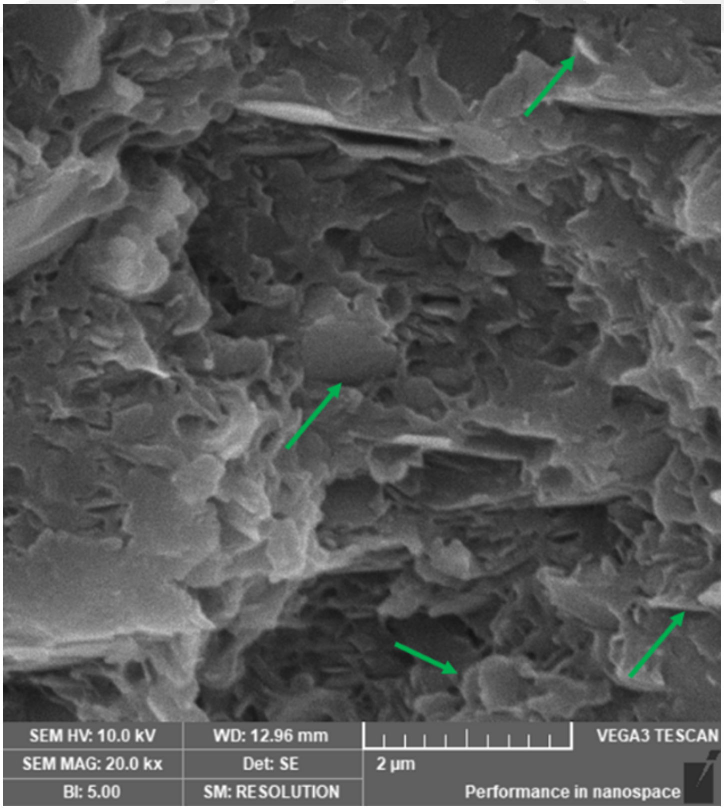

Figure 3.5 : Fracture surface of PHS30 composition.

does not show the existence of several hBNs densely packed in a compact region, as was observed in the PHS35 composition. This indicates that there is no significant clustering in the PHS30 group.

3.3 Thermal Characterization

In this section, the results and interpretations of the conducted thermal characterizations are presented. The DSC, DMA, and thermal conductivity test applied to composites under the category of thermal characterization have been outlined.

3.3.1 Differential scanning calorimetry (DSC)

PA6, PSM, PHS30, PHS30, and PHGS30, underwent DSC analysis. The glass transition temperatures (T_g) of these compositions were determined from the acquired results as in the Table 3.4. The glass transition in polymers is the transformation from

Table 3.4 : Glass transition temperature values of the composites.

Sample Name	Glass Transition Temperature (°C)
PA6	75.45
PSM	73.37
PHS30	90.50
PHS35	92.03
PHGS30	92.27

a hard state to a rubbery state due to heating. This transition specifically happens in the amorphous phase of semi-crystalline materials. Enhanced polymer chain mobility leads to alterations in material characteristics. For instance, changes in temperature can lead to a reduction in the stiffness of the material, while simultaneously causing an increase in both the coefficient of thermal expansion and heat capacity. The augmentation in heat capacity enables the determination of the glass transition temperature. The device provided a heat flow-temperature curve, illustrating the relationship between thermal energy and temperature. To determine the glass transition temperature from this curve, draw a line connecting the starting and ending points of the region where the slope visibly changes for the first time from room temperature. The temperature value corresponding to the midpoint of this line on the curve represents the glass transition temperature. It was conclusively determined. The glass transition temperature values derived from DSC measurements in this investigation are presented in Table 3.4. Simultaneously, Figures B.1, B.2, B.3, B.4, and B.5 in

Appendix B present graphs of DSC measurements that indicate the glass transition temperatures. The DSC results showed that the composites exhibited higher glass transition temperatures when reinforced with h-BN and GnPs. The primary factor responsible for this condition is the higher concentration of particles in the matrix, which hinders the mobility of PA6 chains and consequently leads to an elevation in T_g. The upward trajectory of T_g persisted with the addition of GnPs supplementation. This is associated with the large interfacial area between the GnPs and the polymer. The utilization of nanoplates results in an expanded surface area, which hinders the mobility of polymer chains during the transition to a rubbery state. Consequently, the chains must possess greater energy in order to overcome this constraint. The increase in temperature (raising T_g) also contributes to this high energy [68, 69]. The addition of SEBS resulted in a drop in the T_g of PA6. In this instance, the correlation can be attributed to the low T_g of SEBS and the great mobility of its polymer chains.

3.3.2 Dynamic mechanical analysis (DMA)

The thermomechanical characteristics of the composites were examined using DMA. The T_g obtained from DMA is a critical threshold that determines the suitability of composites for structural applications and T_g results are displayed in Figure 3.6. Once the temperature reaches the T_g, the mechanical strength of these composites significantly decreases. This element should be taken into account during the design phase. DMA analysis is widely regarded as an effective approach for comprehending the underlying factors that influence thermomechanical behavior [70]. In addition, the inclusion of h-BN and GnPs resulted in an increase in the glass transition temperature. The glass transition temperatures of the compositions, which surpass the range of 15 to 40 °C, the recommended working temperature for batteries, indicate that the compositions are in a thermomechanically safer state.

3.3.3 Thermal conductivity test

After DMA analyses, the thermal conductivity measurements were performed to ascertain the influence of h-BN and GnPs on thermal conductivity, and the results collected are presented in Figure 3.7.

The anisotropy of the thermal conductivity of h-BN has been firmly established as a result of its layered structure. h-BN platelets consist of multiple single-layer BN nanosheets that are stacked together through the Van der Waals force. The thermal

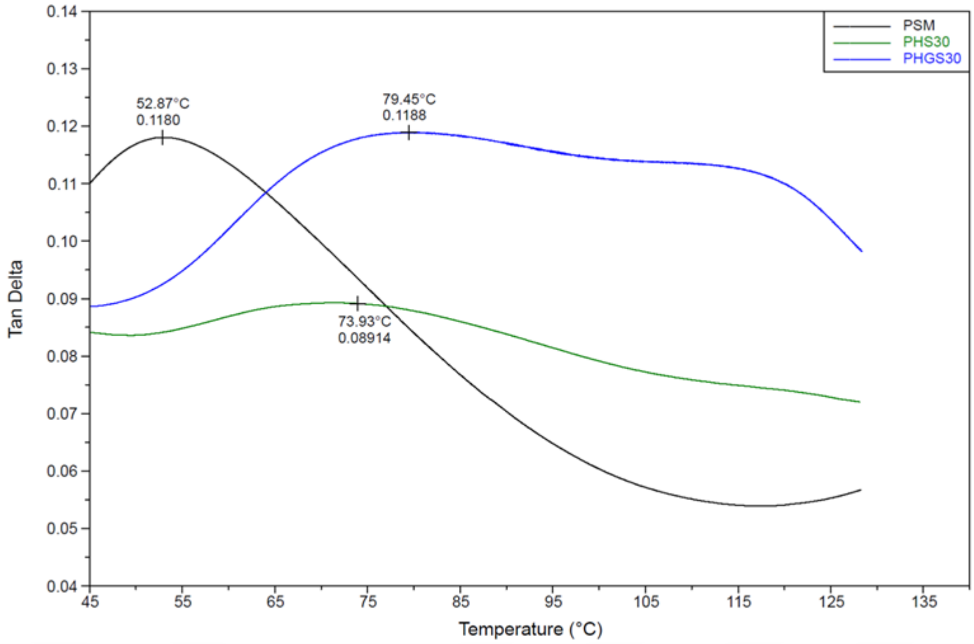

Figure 3.6 : Tan Delta curves for the PSM, PHS30, and PHGS30 composites.

conductivity of h-BN in the in-plane (002 plane) direction is around 600 W/mK due to the strong covalent connections between B atoms and N atoms. On the other hand, the thermal conductivity in the through-plane (100 plane) direction is roughly 1.5–2.5 W/mK due to interlayer phonon scattering [71]. The results indicate that the thermal conductivity of the SEBS modified matrix increased by 194.3% when 30 wt.% h-BN was added. The formation of thermal channels that align with the heat flux is the key aspect of improving thermal conductivity. When BN plates are randomly dispersed inside the polymer matrix, they establish contact with each other, forming a heat pathway due to their high aspect ratio. The thermal conductivity is adversely affected by the large reduction in thermal contacts between vertically oriented BN plates. Consequently, there is minimal interaction between h-BN platelets during heat transfer, and the thermal conductivity of the composites is dominated by the polymer matrix [71]. The thermal conductivity decreased by 15.3% when the mass concentration of h-BN increased from 30% to 35%. The presence of clustered BN platelets throughout the thickness is assumed to have resulted in a decrease in heat conductivity. This is because heat transfer is limited to a particular area due to the matrix's influence. Moreover, when examining the theoretical and experimental densities in the PHS35 composition, it was seen that the disparity was more pronounced in comparison to other compositions. There is an accepted notion that an increase in the amount of void

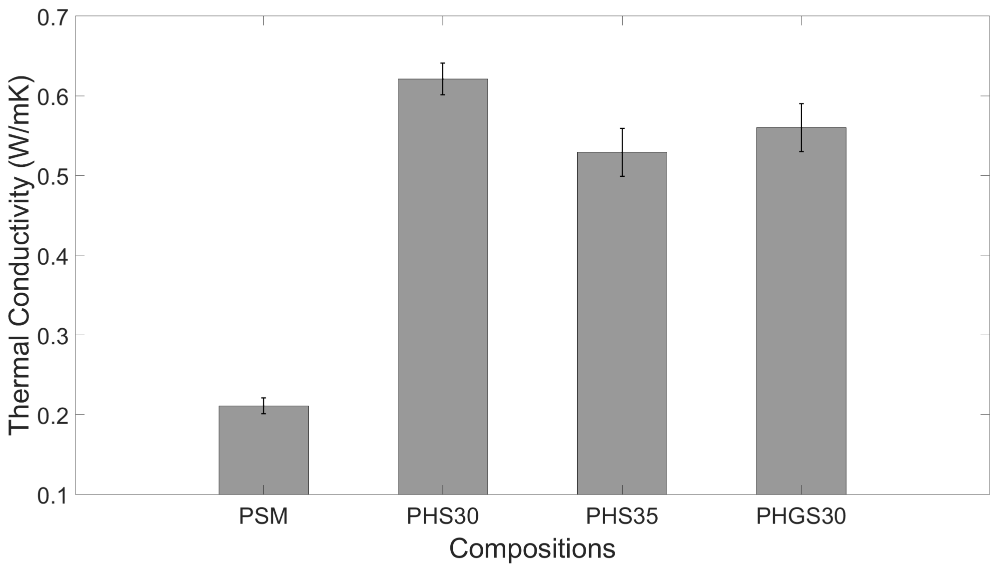

Figure 3.7 : Thermal conductivity of compositions.

space within the composition negatively affects its thermal conductivity as well. The thermal conductivity of composites is substantially influenced by several aspects, such as the form, alignment, waviness, content, dispersion, and thermal contact resistance of the particles at the interface between the matrix and the nanofillers [72]. The main factor contributing to effective heat transfer in GnPs is the diffusion of phonons. Therefore, an appropriately organized network of nanofillers inside the polymer matrix can lead to a reliable improvement in heat conductivity in the composites [73]. However, the interfaces within the GnPs in the particle network also influence the thermal conductivity of the resulting composites. Networks consisting of smaller particles may have a lower improvement in thermal conductivity as a result of increased contact resistance and phonon dispersion caused by numerous contacts [72]. Thermal conductivity of a thin film (or paper) created from small graphene nanoplatelets (1 μm in diameter) is 60.8% lower than the film made from bigger particles (15 μm in diameter) [74]. The presence of GnPs in the composition resulted in a reduction of thermal conductivity approximately 9.82%. Due to the small diameter (1.5 μm) of the GnPs utilized in this investigation, it is possible that the anticipated rise in contact resistance and thermal conductivity due to phonon dispersion may not have been observed. Furthermore, the presence of possible agglomeration in the 30wt.% h-BN utilized in this composition could lead to a reduction in thermal conductivity. The test results revealed a notable disparity between the expected and actual thermal conductivities of the composites. It was aimed to explore an intermediate solution that

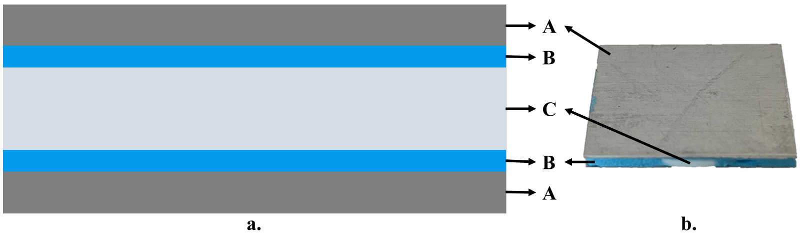

Figure 3.8 : (a) Representative view of the designed sandwich structure (b) test sample of sandwich structure.

aims to enhance heat conductivity while maintaining lightweightness. In this study, a sandwich structure is designed using aluminium and composite, as shown in Figure 3.8a. Figure 3.8b is the real test sample for sandwich structure. According to the data acquired, PHS30 exhibits the highest thermal conductivity, making it the preferred choice for the core structure. In Figure 10a, the component denoted as A is aluminium from the 2024-T351 series, the component designated as B is thermal paste, and the component designated as C is PHS30. A, B, and C have respective thicknesses of 0.5 mm, 0.25 mm, and 1 mm. By using the sandwich structure, the thermal conductivity was increased to 1.15 W/m.K. An impressive rise of 85.4% in thermal conductivity was noted, whereas the sandwich structure experienced a noteworthy 68.6% increase in weight. Optimizing the thickness

4. DESIGN OF A COMPOSITE BASED BATTERY CASING: NUMERICAL ANALYSIS OF MECHANICAL PROPERTIES

In this section, the elastic constants and thermal conductivity of the compositions were determined utilizing analytical methods. The Maxwell-Eucken and Cheng-Vachon models were employed for the analysis of thermal conductivity, while the Halpin-Tsai (HT) model was utilized to determine the elastic constants. Furthermore, the mechanical and thermal characteristics of these compositions were assessed by creating a representative volume element (RVE) using Digimat FE. To verify the accuracy of these models, they were compared to empirical data. In the end, the compositions were evaluated based on several qualities, resulting in the selection of the most suitable composition. The optimization study utilized the response surface method (RSM) in combination with a Python-based optimization tool. Properties of optimum composite were then utilized in the ground effect simulation conducted using Abaqus CAE in the subsequent step.

4.1 Determination of Equivalent Material Properties of the Developed Composites

Analytical methods were used to determine the elastic constants and thermal conductivity of the compositions in this section. The Maxwell-Eucken and Cheng-Vachon models were used to analyze thermal conductivity, while the Halpin-Tsai (HT) model was used to calculate the elastic constants. In addition, the mechanical and thermal properties of these compositions were evaluated by generating a representative volume element (RVE) using Digimat FE.

4.1.1 Determination of equivalent elastic constants

Following a series of experimental investigations, the mechanical properties of the composites were determined using micromechanical models. Within this framework, multiple models exist for predicting the elastic properties of composite materials reinforced by nanoparticles. These models take into account the geometry and orientation of the additive as well as the elastic properties of the matrix. The Halpin-Tsai (HT) model is one of these models. The revised HT model for GnP supplementation is represented by equations 4.1, 4.2, 4.3, 4.4, 4.5, and 4.6 [75–77]. The elastic modulus of the composite, matrix, and reinforcement material were denoted as E_c, E_m, and E_f, respectively. V_f and ξ represent the proportion of volume occupied by the reinforcement material and the shape factor, respectively.

$$E_c = \frac{3}{8}E_L + \frac{5}{8}E_T \tag{4.1}$$

$$E_L = E_m\left(\frac{1+\xi\eta_L V_f}{1-\eta_L V_f}\right) \tag{4.2}$$

$$E_T = E_m\left(\frac{1+2\eta_T V_f}{1-\eta_T V_f}\right) \tag{4.3}$$

$$\eta_L = \frac{E_f/E_m - 1}{E_f/E_m + \xi} \tag{4.4}$$

$$\eta_T = \frac{E_f/E_m - 1}{E_f/E_m + 2} \tag{4.5}$$

$$\xi = \frac{2D_f}{3t_f} \tag{4.6}$$

The elastic modulus values of the composites were determined based on the provided formulas and composite compositions. The rule of mixtures for PSM composition was utilized for the calculation of the elastic modulus [78]. The HT model that accounted for platelet-shaped supplements was utilized for the remaining components. There are two distinct methods to consider the random orientation of reinforcements in both two-dimensional (2D) and three-dimensional (3D) scenarios for the corrected HT model. The HT model, which describes the random orientation in two dimensions as stated in equation 4.1, was chosen because to its superior convergence properties [77]. In this equation, E_L and E_T represent the modulus of elastic in the longitudinal and transverse directions, respectively. These values were calculated using equations 4.2 and 4.3. The ξ function, as defined in equation 4.6 [75], was utilized for platelet-shaped reinforcements. The ξ value was calculated using the diameter (D_f) and thickness (t_f) of the reinforcement material [79]. h-BN and GnP were included in the software using a geometric representation in the form of platelets, as shown in Figure 4.1. When determining the elastic modulus of the PHS30 and PHS35 composition, the value obtained for PSM from the rule of mixtures was utilized as E_m.

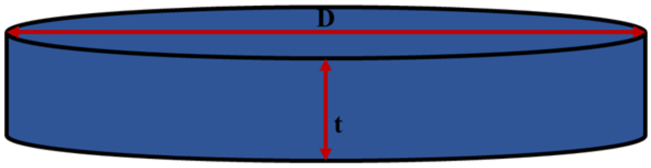

Figure 4.1 : Geometric representation of h-BN and GnPs.

The values of D_{h-BN} and t_{h-BN} for h-BN were obtained from Table 4.1. The elastic modulus values for PHS30 and PHS35 were determined by varying the quantities of h-BN and volumetric ratios. The data acquired from the HT model for PHS30 was utilized as the value for E_m in the formulation of PHGS30. The D_{GnP} and t_{GnP} values of GnP were recorded according to the data shown in Table 4.1. This section

Table 4.1 : D_f and t_f values of h-BN and GnPs.

Materials	D_f (nm)	t_f (nm)
h-BN	790	98.75
GnPs	1500	3

discusses the creation of a composite RVE (Representative Volume Element) with the PHS30,PHS35, and PHGS30 using Digimat and the mechanical homogenization process. Mechanical properties such as elastic modulus, shear modulus, and Poisson ratio of the RVE were determined.

Digimat FE is a simulation program used in material modeling and analysis. This program enables understanding the behaviors of complex materials, facilitating optimization studies. Its capability to model complex behaviors of various materials (metals, polymers, ceramics, composites, etc.) makes it applicable across different industries. It is used for particularly prevalent in cost reduction and process optimization efforts. In this study, the mechanical properties of the PHS30, PHS35, and PHGS30 compositions were calculated. The material inputs used in the simulation were shared in Table 4.2. The initial step in the program involved introducing the materials. PA6 and SEBS were designated as the matrix of the composite, and their Young's modulus, Poisson's ratio, and density were determined using the rule of mixture formula. GnPs and h-BN were assumed to be distributed randomly in three dimensions as platelets. A convergence of the parameters of a RVE has been observed, with a size estimated to be around 17–18 times the diameter of the inclusions, in the context of elastoplastic behaviour [80]. An RVE with dimensions of 13.5x13.5x13.5

Table 4.2 : Mechanical simulation inputs of the materials.

Property	PA6	h-BN	GnPs	SEBS
Young's Modulus (MPa)	2800	37000	10^6	1.4
Poisson's ratio	0.43	0.21	0.2	0.499
Density (g/cm^3)	1.16	2.3	2.25	0.89
Inclusion shape	-	Platelet	Platelet	-
Aspect ratio	-	1:8	1:500	-
Size (nm)	-	790	1.5	-

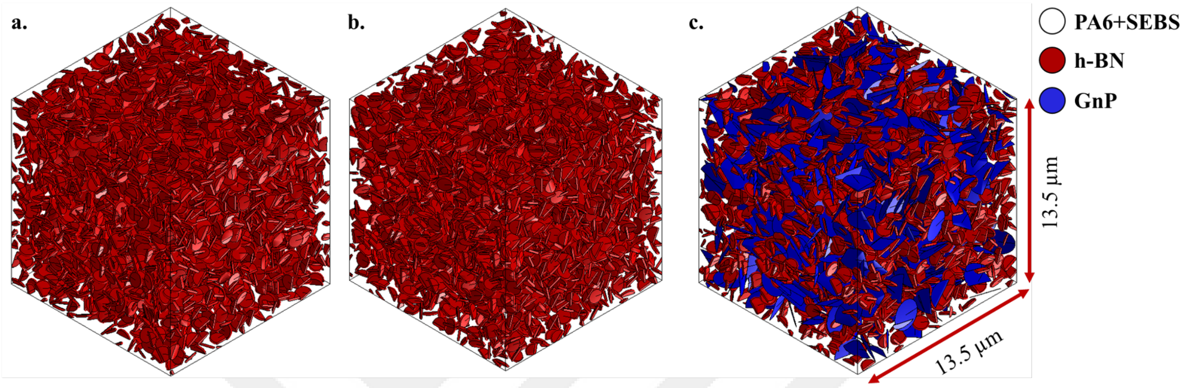

Figure 4.2 : RVE of (a) PHS30, (b) PHS35, and (c) PHGS30.

µm, depicted in Figure 4.2, was generated. Following that, a non-conforming (voxel) mesh consisting of a total of 125,000 elements was applied to this RVE geometry. The obtained results were displayed in Figure 4.3. The results revealed that the elastic modulus values obtained by the HT model and RVE were greater than the experimental values. The discrepancy was believed to arise from the assumption that the reinforcements in the RVE and HT model are precisely aligned and uniformly distributed [75]. PHS35 exhibited a notable disparity in composition when compared to the other compositions. The decline in experimental findings can be attributed to the clusters depicted in Figure 3.4, thus elucidating this phenomenon. Ultimately, the HT model disregards the quality of the interface between the matrix and the reinforcement. While interface healing agents were employed in this investigation, any interface issues could potentially result in variations in the experimental outcomes.

4.1.2 Determination of equivalent thermal conductivity

After a series of experiments, the thermal properties of composites have been determined using micro-mechanical models. In order to examine the impact of h-BN and GnPs on the thermal conductivity of composites numerically, the Maxwell model [81] and Cheng-Vachon model [82] were utilized. Maxwell model was given in

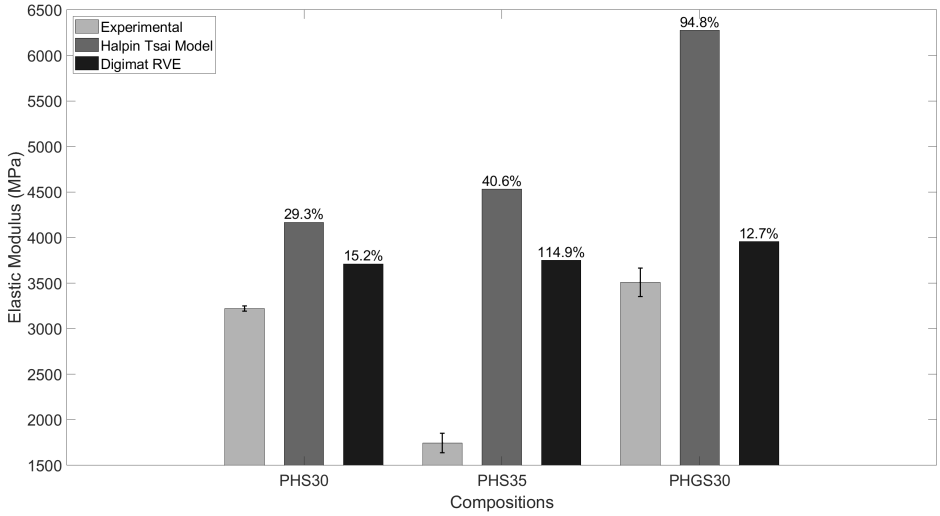

Figure 4.3 : Elastic modulus comparison of experimental, HT model, and Digimat RVE.

Equation 4.7, Cheng-Vachon model was given in Equations 4.8-4.12. k_p, k_f, d_p, d_c, V_f and W_f are thermal conductivity of polymer matrix, thermal conductivity of reinforcement, density of polymer matrix, density of composite, volume fraction of reinforcement, and mass fraction of reinforcement, respectively. The properties of the material listed in Table 4.3 were utilized.

$$k = (2k_p + k_f + 2V_f(k_f - k_p))/(2k_p + k_f - 2V_f(k_f - k_p)) \tag{4.7}$$

$$D = \frac{2((k_p + B(k_f - k_p)))^{(0.5)} + B(C(k_f - k_p))^{(0.5)}}{(2((k_p + B(k_f - k_p)))^{(0.5)} - B(C(k_f - k_p))^{(0.5)})} \tag{4.8}$$

$$\frac{1}{k} = \frac{(1-B)}{k_p} \frac{1}{(C(k_f - k_p)(k_p + B(k_f - k_p)))^{(0.5)})} \ln[D] \tag{4.9}$$

$$B = ((3V_f)/2)^{(1/2)} \tag{4.10}$$

$$C = (2/(3V_f))^{(1/2)} \tag{4.11}$$

$$V_f = 1 - d_c/d_p(1 - W_f) \tag{4.12}$$

In order to determine the thermal properties of PHS30, PHS35, and PHGS30, the RVE was developed utilizing Digimat FE and the simulation parameters were presented in Table 4.3. The initial step in the Digimat software involved introducing the materials.

PA6 and SEBS together were designated as the matrix of the composite, and their thermal conductivity, specific heat capacity, and density were determined using the rule of mixtures. RVEs shown in Figure 4.2 with dimensions of 13.5x13.5x13.5 μm were generated. Non-conforming (voxel) mesh consisting of a total of 125,000 elements

Table 4.3 : Thermal simulation inputs of the materials.

Property	PA6	SEBS	h-BN	GnPs
Thermal Conductivity (W/mK)	0.23	0.46	96	5000
Specific heat capacity (J/kgK)	1940	1900	1610	643
Density (g/cm^3)	1.16	0.89	2.3	2.25

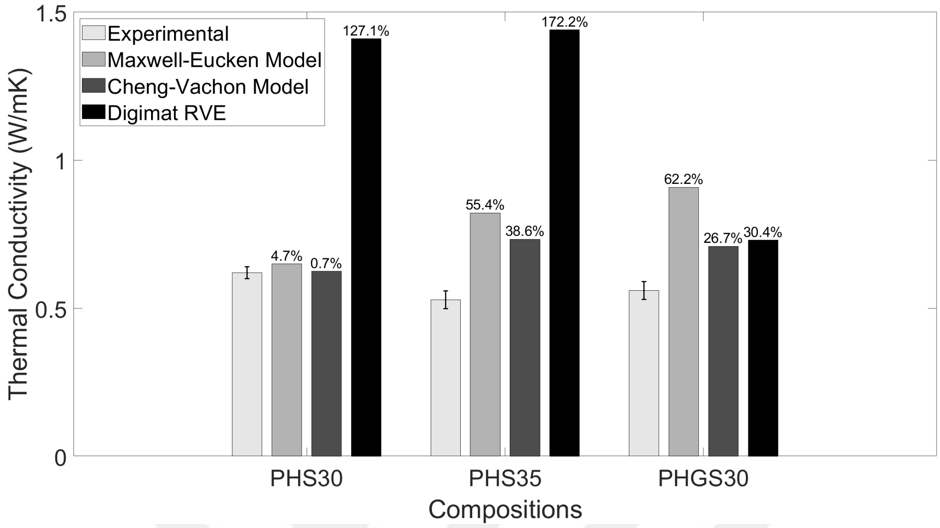

Figure 4.4 : Thermal conductivity comparison of experimental, Maxwell-Eucken model, Cheng-Vachon model, and Digimat RVE.

was applied to this RVE geometry. As a result of the analysis, the thermal conductivity of the composites was determined as K_{11}, K_{22} and K_{33}. The obtained values were given comparatively in Figure 4.4. There was a discrepancy between the estimations of the analytical models and the experimental data. The reason for this difference was due to the assumption made by analytical models that the reinforcing particles are spherical in shape. h-BN possesses a multilayer structure characterized by hexagonal symmetry [83]. The thermal conductivity values derived using Digimat for PHS30 and PHS35 showed discrepancies compared to the experimental data. The emergence of this disparity may be attributed to the simulation's attempt to replicate reinforcements in a perfectly uniform and homogeneous distribution.

4.2 Determination of the Optimum Composite Composition

In this section, the composites produced will be evaluated from different aspects to select the optimal composite. The PHS30, PHS35, and PHGS30 composites were evaluated based on parameters such as tensile strength, elastic modulus, Izod notched impact strength, thermal conductivity, and price. The parameter values used during the evaluation were provided in Table 4.4. Tensile strength, elastic modulus, Izod notched impact strength, and thermal conductivity values were obtained from mechanical and thermal tests. The price represents the cost corresponding to per kilogram of composite material. The objective of the optimization study was to improve the thermal conductivity, tensile strength, and elastic modulus of the material while simultaneously reducing its cost. Two different approaches were used to determine

Table 4.4 : Optimization parameters of the composites.

Composition Name	Tensile Strength (MPa)	Elastic Modulus (MPa)	Impact Strength (kJ/m^2)	Thermal Conductivity (W/mK)	Price ($/kg)
PHS30	47.77	3221.68	4.10	0.62	49.61
PHS35	50.82	1745.15	3.90	0.53	57.56
PHGS30	49.81	3508.54	3.5	0.56	66.16

the optimum combination. The initial approach employed was Response Surface Methodology (RSM). The RSM is a specialized subset of Design of Experiments (DOE) approaches. This is a highly effective statistical tool used for planning, developing, improving, and optimizing product designs and processes. This tool simplifies the process of identifying the composite material that demonstrates the most favorable qualities. The RSM can be utilized to ascertain the most advantageous combination of input variables by considering their corresponding outcomes. The RSM is a reliable technique for generating a model. The coefficients of the function in this model were selected with the objective of minimizing error. Thus, by utilizing the least squares method, a polynomial function is approximated with little error, resulting in the best possible results. Nowadays, computer simulation technologies can be used to improve materials, particularly with the help of the RSM, eliminating the need for real prototypes. It is commonly used in work contexts where multiple input variables (factors) might affect the outputs (responses) of a product or process. As a result, this accelerates the process of developing materials and thereby lowers the expenses associated with trial-and-error studies [84]. The weight (importance) of the composites' parameters were assigned based on their relative importance to the objectives. The values for tensile strength, elastic modulus, Izod notched impact strength, thermal conductivity, and price were determined to be 0.1, 0.1, 0.2, 0.35 and 0.25 respectively. When establishing these numbers, the utmost importance was given to the improvement of thermal conductivity as it was the main goal of the project.

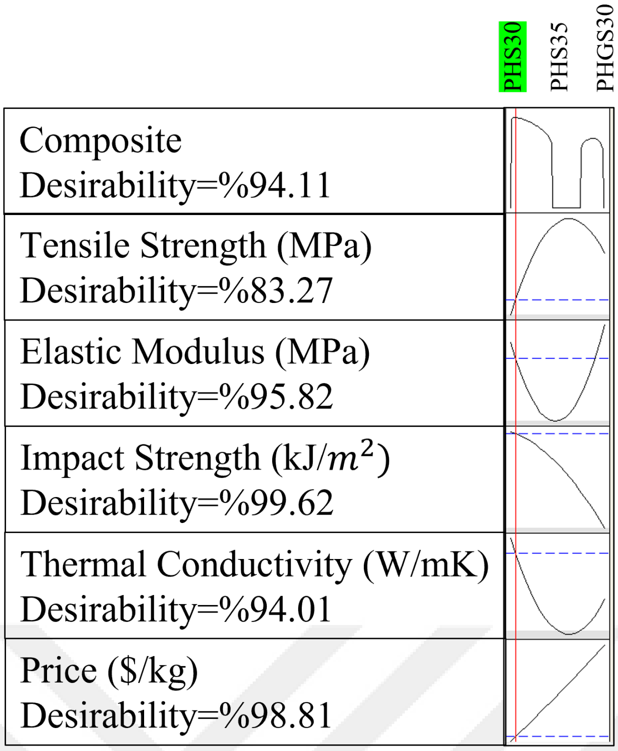

Figure 4.5 : The optimization curves obtained with Minitab.

Given that the cost associated with producing samples was a critical aspect for their adoption, the second most significant parameter was identified as impact strength. The mechanical properties, namely tensile strength and elastic modulus, were shown to be equally significant.Upon thorough analysis of the collected data, desirability of tensile strength, elastic modulus, impact strength, thermal conductivity, and price are 83.27%, 95.82%, 99.62%, 94.01%, and 98.81%, respectively as in Figure 4.5. It was determined that the composition PHS30 exhibited the highest level of desirability, with a rating of 94.11%. An alternative optimization strategy was used to obtain the optimal composite by executing a Python based algorithm. The algorithm based on Python is given in the Appendix C. In the Python algorithm-based application, the user provides inputs such as compositions, parameters, parameter values, parameter importance coefficients, and the parameter target (whether it is for maximization or minimization). After defining the inputs, an initial computation was conducted to ascertain the weighted value allocated to each parameter. The weighted value was determined by comparing the parameter value of a specific composition to the total parameter value of all compositions. Equation 4.13 was employed to determine the weighted value. The evaluated parameter can be maximized or minimized using 4.14

and Equation 4.15 respectively. The scores derived from solving these two equations with various parameters were summed to generate the composition's score.

$$\text{Weighted value} = \frac{\text{Parameter value of the composition}}{\text{Total parameter value of the compositions}} \tag{4.13}$$

$$\text{Score=Importance coefficient x Weighted value} \tag{4.14}$$

$$\text{Score=Importance coefficient x (1-Weighted value)} \tag{4.15}$$

The input values obtained from Table 4.4 were utilized in conjunction with the parameter weights specified in the RSM approach. The values were categorized as either maximizing or minimizing, and the goals were chosen accordingly to achieve the desired results. The scores for PHS30, PHS35, and PHGS30 were found to be 44.65, 39.80, and 40.55, respectively. The results indicate that the scores were ranked in the following sequence: PHS30, PHGS30, and PHS35. According to the findings, PHS30 was identified as the most appropriate composite material for the study, with similar characteristics to Minitab.

4.3 Investigation of the Ground Impact

This section presents the simulation study conducted to determine the ground effect. The simulation conducted utilizing the finite element method utilized ABAQUS CAE. The analysis followed the Abaqus CAE process phases. The initial phase involved the modeling of the parts. There are two distinct alternatives for modelling parts. The first option can be executed in the parts space within the Abaqus CAE. The second choice was to use a different modelling software to create the parts and then import them into Abaqus CAE. This approach facilitates the creation of complex geometrical shapes with less difficulty. Due to the complex geometry of the model required in the part section of Abaqus CAE, the modelling process was conducted using the Siemens NX CAD software. The components of the battery module (battery casing, battery module casing, and batteries) and the object impacting the battery module were designed using the Siemens NX. The battery casing has dimensions of 315 x 500 x 4 mm and was positioned at the bottom. The battery module casing was composed of two separate components, an upper and a lower section, each measuring 315 x 500 x 35.5 mm in size. The thickness of the side and bottom walls was determined to be 3 mm. Two distinct situations were utilized for the simulation investigation. The utilization of aluminium was depicted in Figure 4.6, whereas the utilization of PHS30 composition was depicted in Figure 4.7. The PHS30 battery module casing was 26.9% lighter than aluminium when compared in terms of weight, despite variations in design and material. In the given situation, a composite material was utilized, specifically a honeycomb design for the battery module casing. The thickness of the walls of these constructions was determined to be 1.5 mm. The upper battery module casing does not utilize a honeycomb shape. In the case of using aluminium, the honeycomb structure was not employed for the upper and lower casings of the battery module. There are two methods to simulate the battery casing and battery module casing. One method involves importing it into the Abaqus CAE software as a solid model, while the other method involves importing it as a shell geometry. While the solid model provides more detailed results for stress and deformation, the shell geometry offers faster computation times for larger structures. Given that the significance of transverse shear deformation is minimal in components with a thickness/length (h/L) ratio below 0.3, employing shell structure models is appropriate for conducting this research [85]. While these structures, designed as solids, were transferred to Abaqus CAE, their middle surfaces were created and converted into shell geometry. Additionally, the mesh structure was defined using the Siemens NX pre/post module. The battery module casing and the battery casing shell geometry in the simulation model consist of triangular and quadrilateral element architectures. The conventional large-strain shell elements (S3R and S4R) are suitable for most analyses. S4R is a versatile and durable quadrilateral element that may be used for various applications. S3R is a triangle element that has the potential to experience minor shear locking [86]. The S4R element type was selected for these structures for this reason. In order to determine the number of elements of battery module bottom casing, it is investigated the relationship between the strain energy and the number of elements [87]. Figure 4.8 provides the relationship between the strain energy and analysis time for different elements. Therefore, the 24745-element (element size = 6 mm) mesh structure from the 3th analysis, which exhibits stable strain energy and consistent analysis time, was utilized for further study.

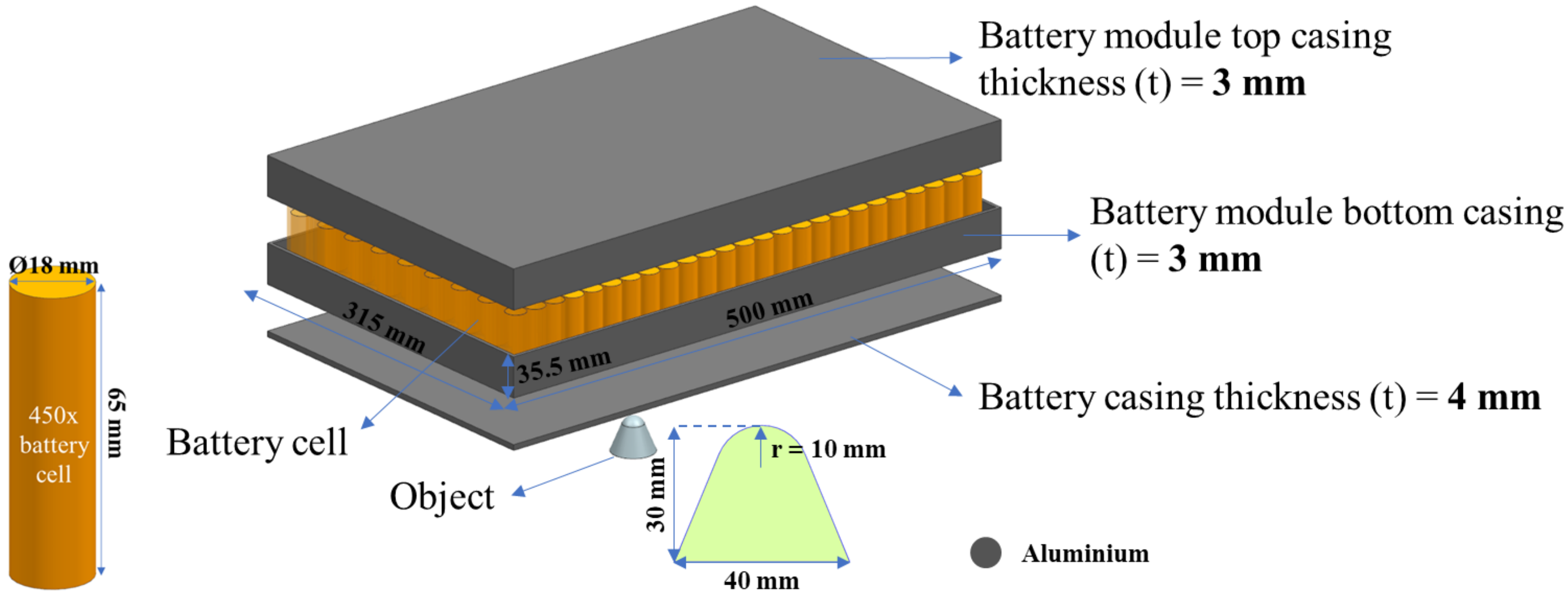

Figure 4.6 : Details in the case of utilizing aluminium battery module casing.

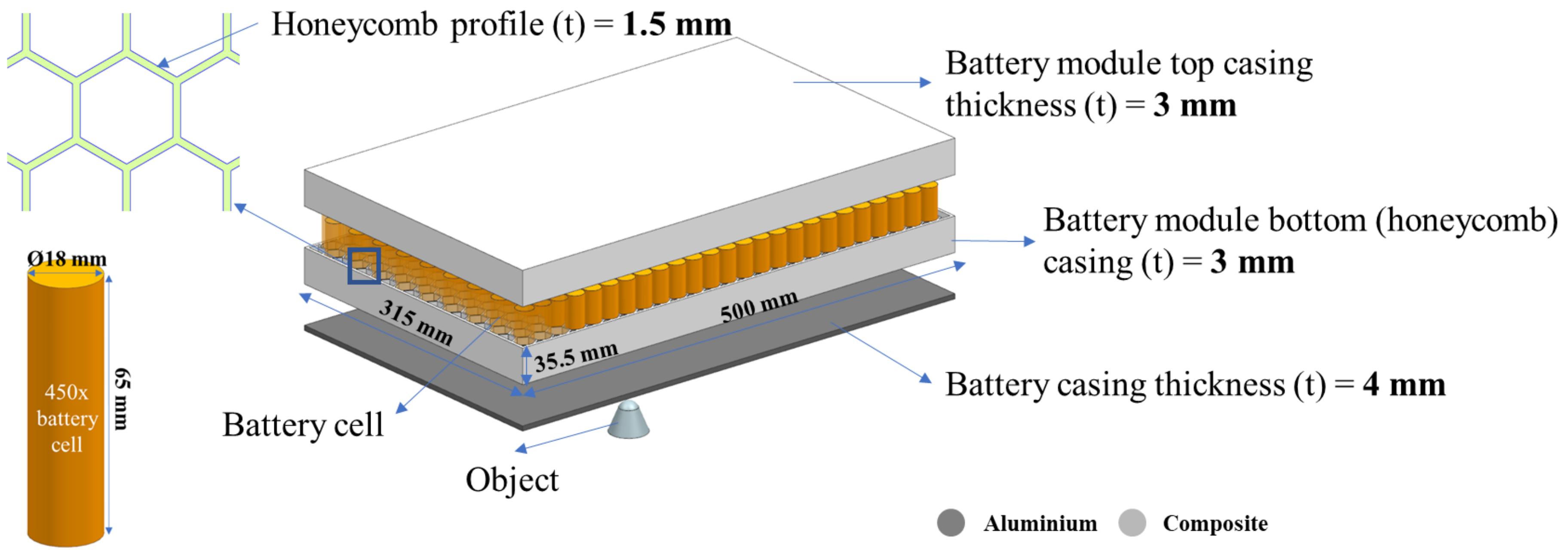

Figure 4.7 : Details in the case of utilizing composite battery module casing.

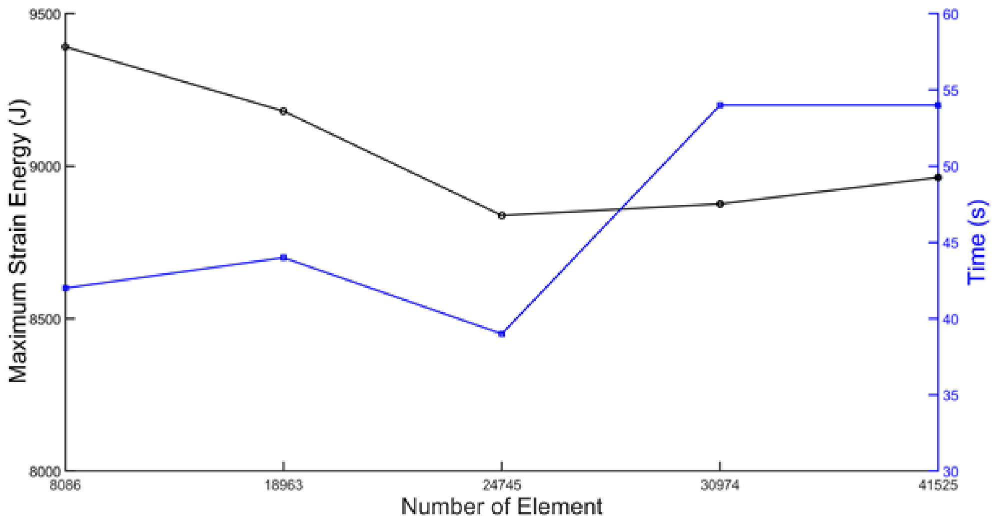

Figure 4.8 : Relationship between number of element - maximum strain energy - time.

The element size utilized in all geometries was established at 6 mm. Battery casing has 4452 elements, battery module casing with honeycomb geometry has 24745 elements, and battery module casing without honeycomb geometry has 5936 elements. The battery cells were designed using the specifications of the conventional 18650 battery cells, which have a diameter of 18 mm and a length of 65 mm [88]. A battery module contains a collective sum of 450 battery cells. Batteries were modeled as beams in Figure 4.9a to simplify the calculation process when imported into Abaqus CAE. Once again, the batteries were integrated using the Siemens NX pre/post module. Initially, a circular profile was defined for the batteries. Then, linear beam element (B31: a 2-node linear beam in space) was selected for the wire discretization. Each node of a three-dimensional beam has six degrees of freedom [89]. The dimension of the element was specified as 2 mm. Figure 4.9b displays a solid visual representation of the batteries' mesh structure, which was characterized as a beam. The object was represented as a solid entity. The dimensions shown in Figure 4.6 were used to simulate the object that struck the battery system, which was classified as discrete rigid [1]. In the property stage, the initial determination was made regarding the materials that will be utilized in the creation of the models. Aluminium has a density of 2.7 g/cm^3, a modulus of elastic of 70 GPa, and a Poisson's ratio of 0.33 [90]. The material of battery cells has a density of 2.8 g/cm^3, a modulus of elastic of 1500 MPa, and a Poisson's ratio of 0.15 [91]. The engineering constants, and density for PHS30 in Table 4.5 were defined in the reference. The thickness and material details of the models utilized in both cases may be found in Figure 4.6-4.7. Furthermore, in this

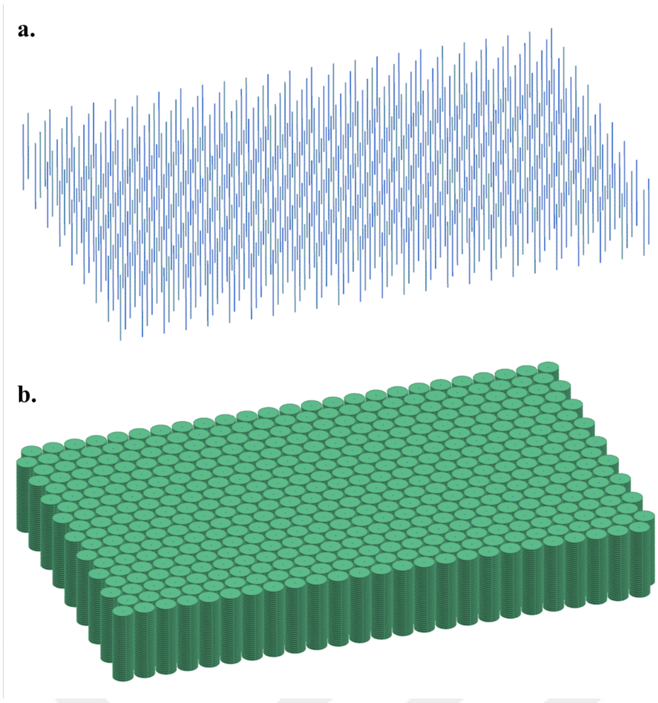

Figure 4.9 : (a) Batteries modelled as beams and (b) representative solid mesh of batteries modelled as beams.

portion, the assignment of a reference point for the object impacting the battery system was conducted. An object was assigned a mass of 30 g with respect to this reference point [1]. During the assembly stage, the positional arrangement of the components

Table 4.5 : Mechanical properties of the RVE of PSH30.

Property	Value
E_{11} (MPa)	3712
E_{22} (MPa)	3710.67
E_{33} (MPa)	3714
E_{12} (MPa)	1238.97
E_{13} (MPa)	1241.3
E_{23} (MPa)	1240.13
ν_{12}	0.41
ν_{13}	0.41
ν_{23}	0.41
Density (g/cm^3)	1.34

was established. The model consists of cells located within the module, with the battery module attached to the battery shell. To minimize processing time, a 0.5 mm clearance was maintained between the object and the battery casing. During step phase, the specific sort of analysis to be conducted was chosen. Due to the time-dependent displacement involved in the crash test, a dynamic/explicit analysis was chosen as

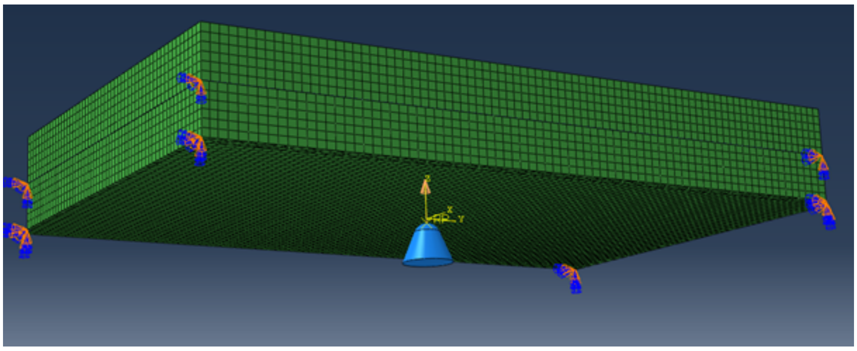

Figure 4.10 : The boundary condition type of the battery system.

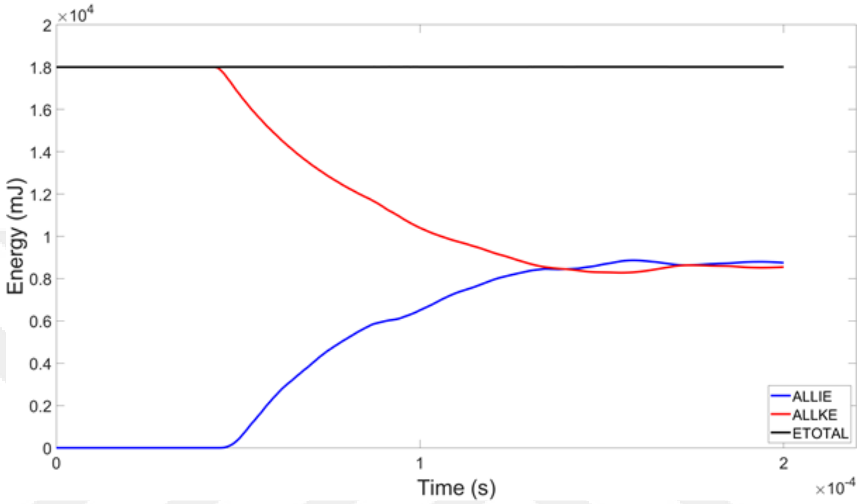

Figure 4.11 : The total energy, kinetic energy, and internal energy curves of the aluminium battery module casing scenario.

the preferred method [92]). The analysis was completed in 0.2 milliseconds. The objective of the following section was to collect data with a frequency of 3000 intervals for both the field output and historical output, ensuring that two different outputs were obtained. Furthermore, the default output types were maintained without any alterations. Following this stage, there is an option called nonlinear geometry (NLGEOM) that allows the user to determine whether the component is linear or exhibits non linearity. This option can be toggled between the "on" and "off" states. The NLGEOM option was expressly chosen due to the performance of a dynamic and high-deformation simulation [93]. During interaction stage, the relationships and connections between the components in the assembly were identified and analyzed. To facilitate the impact, a tangential friction coefficient of 0.3 was universally applied to all surfaces, and the interaction between the components was simulated [94].

During the load stage, the boundary conditions were established. In this analysis, the object impacting the battery system was constrained to move only on the z-axis

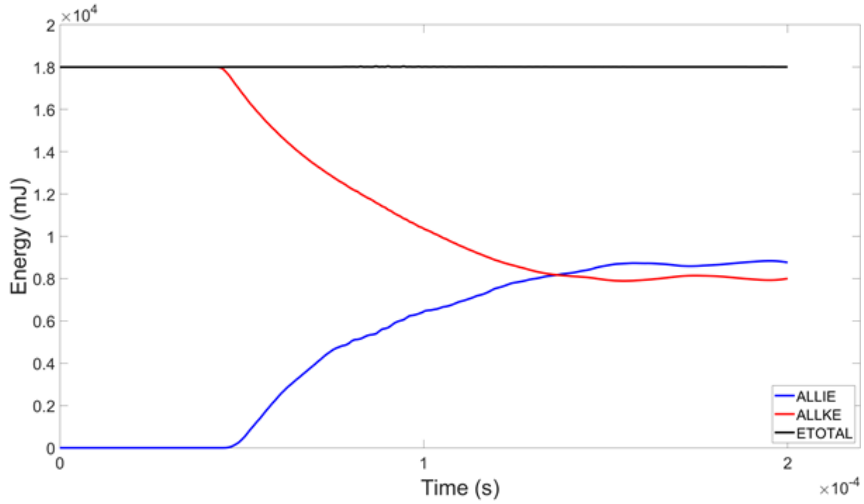

Figure 4.12 : The total energy, kinetic energy, and internal energy curves of the PHS30 battery module casing scenario.

while the battery system remains stationary. Subsequently, the velocity of the object was determined. The speed was defined as a constant of 10 m/s [1]. The boundary condition type was established such that the battery casing and battery module casing were encastre shown in Figure 4.10. During job stage to expedite the computation time, the analysis was conducted utilizing multiple cores. The energy balance of the system was verified to ensure the accuracy of the analysis. Given the presence of a starting velocity in the system, it is necessary for the total energy to remain constant when considering energy transformations inside the system [95]. Upon scrutinizing the analysis results, it was established that the overall energy remained unchanged. The information was presented in Figure 4.11-4.12. Upon analyzing the outcomes of scenarios PHS30 and aluminium battery module bottom case, the deformation results are depicted in Figure 4.13-4.14. Figure 4.13 shows the displacements when using the PHS30 battery module case. It was observed that the maximum deformation was 1.57 mm. Figure 4.14 shows the displacements when using the aluminium battery module case. It was observed that the maximum stress on the battery cell was 1.52 mm. The disparity between the two outcomes is insignificant.

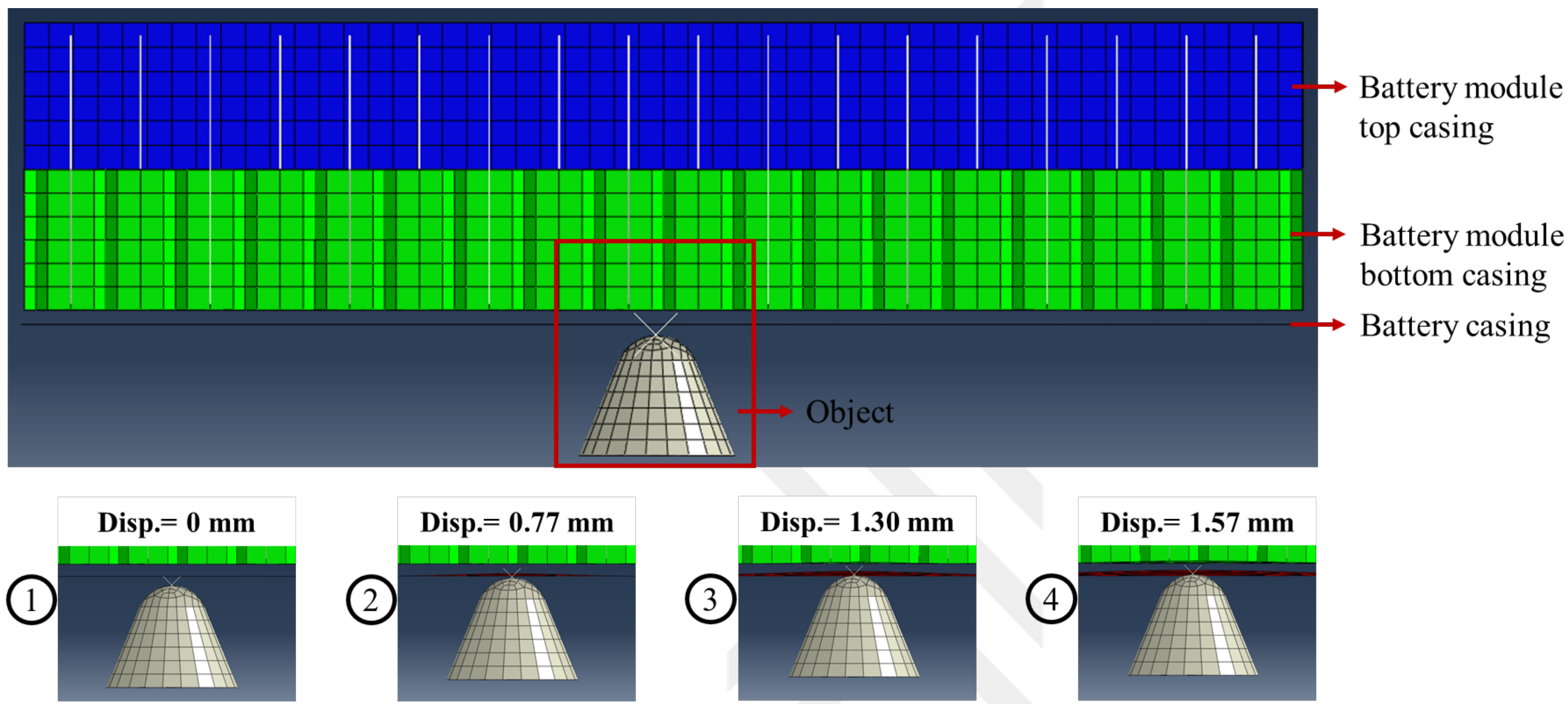

Figure 4.13 : Deformations when using PHS30 battery module casing.

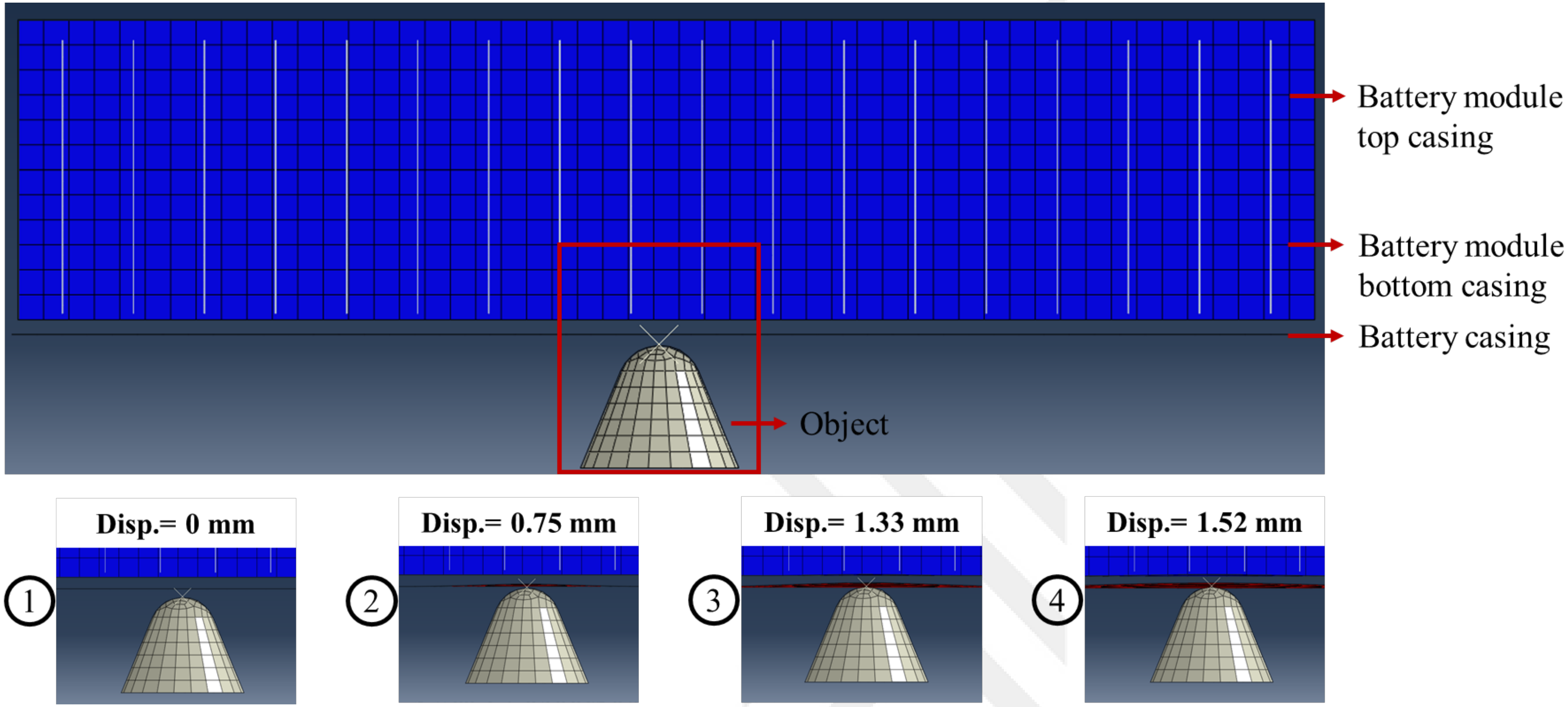

Figure 4.14 : Deformations when using aluminium battery module casing.

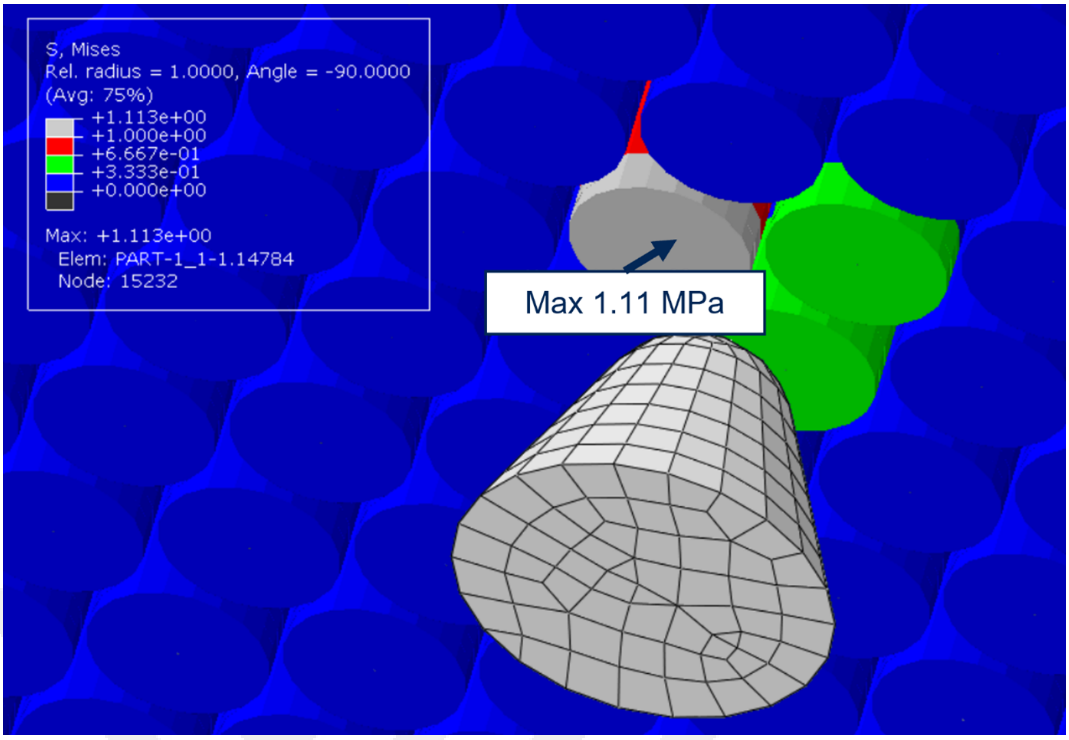

Figure 4.15 : Maximum von Mises stress when using PHS30 composite battery module casing.

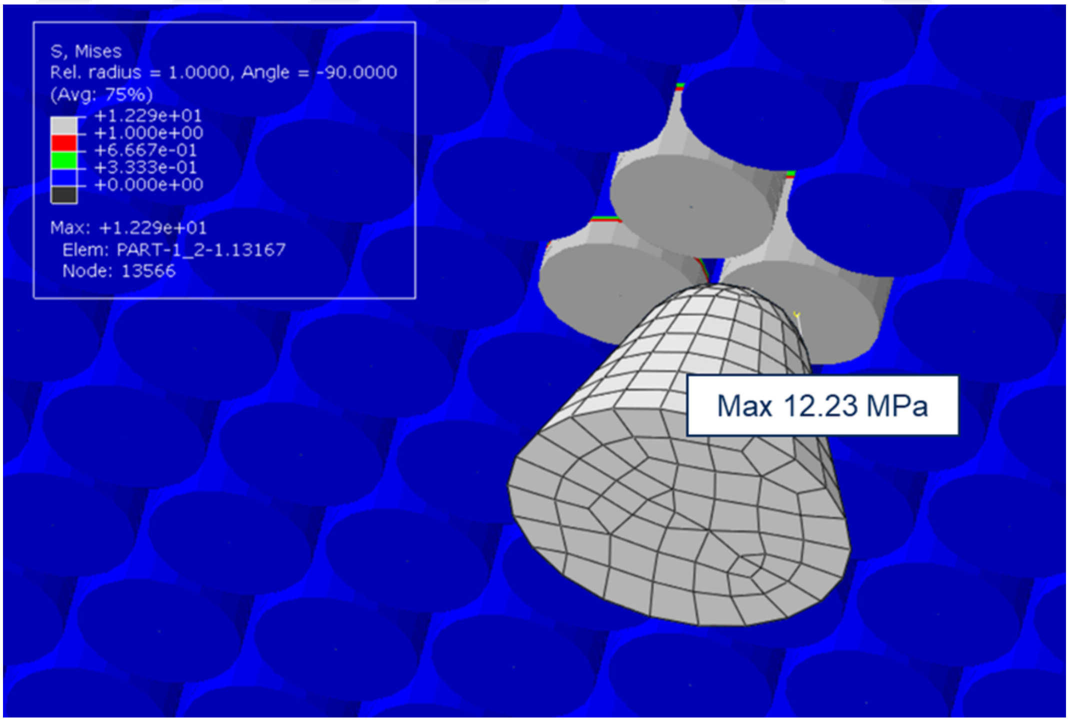

Figure 4.16 : Maximum von Mises stress when using aluminium battery module casing.

5. CONCLUSIONS AND RECOMMENDATIONS

Electric vehicles are essential for promoting sustainable transportation and significantly reducing air pollution. Nevertheless, the limited battery performance continues to impede widespread adoption of electric vehicles due to the Joule effect, which raises the temperature of batteries and reduces their efficiency. Current research is investigating the thermal management of batteries, specifically aiming to find materials that can effectively distribute heat throughout the battery. This research aimed to develop a polymer-based hybrid composite material that enhances both thermal conductivity and impact strength. This material is intended to be used in the production of electric vehicle battery boxes. The selection of polyamide 6 (PA6) as the matrix material was based on its favorable characteristics for manufacture. Thermal conductivity was enhanced by using h-BN and GnPs. Additionally, a SEBS was included to provide protection against damage caused by ground impact. Additionally, a SEBS elastomer supplement was included to provide protection against damage caused by ground impact. Following manufacture, mechanical characterizations showed that GnPs resulted in an 8.9% enhancement in the elastic modulus and a 4.97% enhancement in the tensile strength. The addition of 5 wt% SEBS led to a significant 45% enhancement in the impact strength of the composite. The thermal conductivity had a significant rise of 194.3% when 30% of h-BN was added, considering the weight. By using a sandvich structure that includes PHS30 and aluminium, the thermal conductivity value was increased to 1.15 W/m.K. An 85.4% enhancement in thermal conductivity was observed. The study employed the Maxwell-Eucken and Cheng-Vachon models to examine thermal conductivity and the Halpin Tsai model to determine elastic constants. The Cheng-Vachon model has demonstrated superior convergence to experimental data. The mechanical and thermal properties were evaluated using Digimat FE, and their precision was confirmed through comparison with experimental results. Following the completion of the characterization operations, a distinct analysis was carried out to find the optimal composite using factors such as tensile strength, elastic modulus, impact strength, thermal conductivity, and pricing. The study discovered the best composition by employing two separate methods: RSM and a Python-based optimization algorithm. The compositions were evaluated using weighted values depending on the parameters in the Python-based optimization method. Upon comparing the resulting result with the findings obtained via RSM, it was established that the optimal composition was PHS30 in both ways. Ultimately, a comprehensive crash analysis was conducted to simulate the ground impact, utilizing the PHS30 model that was chosen based on the optimization research. In this study, a battery system was simulated, and the condition of the batteries was assessed in two distinct scenarios. In the initial scenario, the simulation was conducted utilizing aluminum with a box-shaped structure, while in the subsequent scenario, a battery module casing with a honeycomb geometry was employed. Based on the acquired data, the battery was subjected to a stress beyond the damage threshold in the first scenario, but in the second situation, the stress remained below the damage threshold. Furthermore, a significant decrease of 26.9% in weight was achieved for the battery module casing, leading to a design that effectively protects the batteries from damage.

In brief, the thermally improved hybrid composites developed at the laboratory scale in this study exhibit various intriguing characteristics. The unanticipated mechanical properties that arise from the agglomeration of nanoparticles can be alleviated through the utilization of cutting-edge manufacturing facilities. Subsequently, the composites created could potentially capture the attention of electric car manufacturers and enhance the competitive edge of automotive sector companies.

REFERENCES

[1] **Xia, Y., Wierzbicki, T., Sahraei, E. and Zhang, X.** (2014). Damage of cells and battery packs due to ground impact, *Journal of Power Sources*, *267*, 78–97.

[2] **Gong, Y., Zhou, W., Kou, Y., Xu, L., Wu, H. and Zhao, W.** (2017). Heat conductive h-BN/CTPB/epoxy with enhanced dielectric properties for potential high-voltage applications, *High Voltage*, *2*(3), 172–178.

[3] **Omairey, S.L., Dunning, P.D. and Sriramula, S.** (2019). Development of an ABAQUS plugin tool for periodic RVE homogenisation, *Engineering with Computers*, *35*, 567–577.

[4] **Fahrenholz, H.** (2018). The 2012 version of ISO 527 plastics: determination of tensile properties, *Zwick/Roell*.

[5] **STANDARD, B. and ISO, B.** (2001). Plastics Ð Determination of Izod impact strength.

[6] **Farzaneh, F. and Jung, S.** (2023). Lifecycle carbon footprint comparison between internal combustion engine versus electric transit vehicle: A case study in the US, *Journal of Cleaner Production*, *390*, 136111.

[7] **Boden, T., Andres, B. and Marland, G.** (1751). Global co2 emissions from fossil-fuel burning, *Cement manufacture, and gas flaring*, *2006*, 37831–6335.

[8] **Umbraco.Web.PublishedModels.TeamMember**, (2024), Benefits of electric vehicles for you and your business, `https://www.hwca.com/accountants-chester/opinion`.

[9] **Abnett, K.** (2023). EU countries approve 2035 phaseout of CO2-emitting cars, *Reuters, Mar*, *29*.

[10] **Tolmaç, S.**, (2024), Türkiye'nin ilk batarya fabrikasının inşasına Bursa'da başlanacak, `https://www.aa.com.tr/tr/bilim-teknoloji/`.

[11] **Zhang, Y. and Park, S.J.** (2018). In situ shear-induced mercapto group-activated graphite nanoplatelets for fabricating mechanically strong and thermally conductive elastomer composites for thermal management applications, *Composites Part A: Applied Science and Manufacturing*, *112*, 40–48.

[12] **Olabi, A.G., Abbas, Q., Shinde, P.A. and Abdelkareem, M.A.** (2023). Rechargeable batteries: Technological advancement, challenges, current and emerging applications, *Energy*, *266*, 126408.

[13] **Hussein, A.A.H. and Batarseh, I.** (2011). A review of charging algorithms for nickel and lithium battery chargers, *IEEE Transactions on Vehicular Technology*, *60*(3), 830–838.

[14] **van de Kaa, G.**, **Fens, T. and Rezaei, J.** (2019). Residential grid storage technology battles: a multi-criteria analysis using BWM, *Technology Analysis & Strategic Management*, *31*(1), 40–52.

[15] **Wang, Z.**, **Zhang, K.**, **Zhang, B.**, **Tong, Z.**, **Mao, S.**, **Bai, H. and Lu, Y.** (2022). Ultrafast battery heat dissipation enabled by highly ordered and interconnected hexagonal boron nitride thermal conductive composites, *Green Energy & Environment*, *7*(6), 1401–1410.

[16] Range of full electric vehicles | Electic Vehicle Database, `https://ev-database.org/cheatsheet/range-electric-car`.

[17] **Börner, M.**, **Friesen, A.**, **Grützke, M.**, **Stenzel, Y.**, **Brunklaus, G.**, **Haetge, J.**, **Nowak, S.**, **Schappacher, F. and Winter, M.** (2017). Correlation of aging and thermal stability of commercial 18650-type lithium ion batteries, *Journal of Power Sources*, *342*, 382–392.

[18] **Pesaran, A.A.**, **Vlahinos, A.**, **Burch, S.D.** *et al.* (1997). *Thermal performance of EV and HEV battery modules and packs*, National Renewable Energy Laboratory Golden, CO, USA.

[19] **Wadhwani, P.**, (2023), Fundamentals of Cell Balancing amp; Its Types, `https://bacancysystems.com/blog/cell-balancing-and-its-types`.

[20] **Zhao, G.**, **Wang, X.**, **Negnevitsky, M. and Li, C.** (2023). An up-to-date review on the design improvement and optimization of the liquid-cooling battery thermal management system for electric vehicles, *Applied Thermal Engineering*, *219*, 119626.

[21] **Bala, A. and Chaitanya Kamaraju, M.** (2020). Design and optimization of battery housing in electric cars.

[22] **Li, C.**, **Zhang, H.**, **Zhang, X.**, **Zhang, Z.**, **Li, N.**, **Liu, Y.**, **Zheng, X.**, **Gao, D.**, **Wu, D. and Sun, J.** (2022). Construction of bi-continuous structure in fPC/ABS-hBN (GB) composites with simultaneous enhanced thermal conductivity and mechanical properties, *Composites Science and Technology*, *223*, 109437.

[23] **Patel, M.**, **Pardhi, B.**, **Chopara, S. and Pal, M.** (2018). Lightweight composite materials for automotive-a review, *Carbon*, *1*(2500), 151.

[24] **Pickering, S.J.** (2006). Recycling technologies for thermoset composite materials—current status, *Composites Part A: applied science and manufacturing*, *37*(8), 1206–1215.

[25] **Yang, D.**, **Huang, S.**, **Ruan, M.**, **Li, S.**, **Yang, J.**, **Wu, Y.**, **Guo, W. and Zhang, L.** (2018). Mussel inspired modification for aluminum oxide/silicone

elastomer composites with largely improved thermal conductivity and low dielectric constant, *Industrial & Engineering Chemistry Research*, *57*(9), 3255–3262.

[26] **Gu, J.**, **Meng, X.**, **Tang, Y.**, **Li, Y.**, **Zhuang, Q. and Kong, J.** (2017). Hexagonal boron nitride/polymethyl-vinyl siloxane rubber dielectric thermally conductive composites with ideal thermal stabilities, *Composites Part A: Applied Science and Manufacturing*, *92*, 27–32.

[27] **Nazir, M.T.**, **Phung, B.**, **Hoffman, M.**, **Yu, S. and Li, S.** (2017). Micro-AlN/nano-SiO2 co-filled silicone rubber composites with high thermal stability and excellent dielectric properties, *Materials Letters*, *209*, 421–424.

[28] **Kim, C.Y.**, **Dang, T.M.L.**, **Zhang, Y.**, **Yang, J.F. and Wang, B.** (2019). The alignment of AlN platelets in polymer matrix and its anisotropic thermal properties, *Journal of Materiomics*, *5*(4), 679–687.

[29] **Wu, W. and Wang, J.** (2018). Effect of KH550 on the preparation and compatibility of carbon fibers reinforced silicone rubber composites, *Silicon*, *10*, 1903–1910.

[30] **Dai, P.**, **Jiao, Y.**, **Ma, H.**, **Zeng, X.**, **Lu, Y.**, **Wang, L.**, **Bao, M. and Zhai, M.** (2019). Radiation synthesis of polysilane-modified graphene oxide for improving thermal conductivity and mechanical properties of silicone rubber, *Journal of Applied Polymer Science*, *136*(29), 47776.

[31] **Kong, J.**, **Tong, Y.**, **Sun, J.**, **Wei, Y.**, **Thitsartarn, W.**, **Jayven, C.C.Y.**, **Muiruri, J.K.**, **Wong, S.Y. and He, C.** (2018). Electrically conductive PDMS-grafted CNTs-reinforced silicone elastomer, *Composites Science and Technology*, *159*, 208–215.

[32] **Temel, U.N.** (2019). Passive thermal management of a simulated battery pack at different climate conditions, *Applied Thermal Engineering*, *158*, 113796.

[33] **Khan, M.O.**, **Leung, S.N.**, **Chan, E.**, **Naguib, H.E.**, **Dawson, F. and Adinkrah, V.** (2013). Effects of microsized and nanosized carbon fillers on the thermal and electrical properties of polyphenylene sulfide based composites, *Polymer Engineering & Science*, *53*(11), 2398–2406.

[34] **Meng, Z.**, **Dai, Z.**, **Chen, K. and Wang, S.** (2021). Investigation on preparation, thermal, and mechanical properties of carbon fiber decorated with hexagonal boron nitride/silicone rubber composites for battery thermal management, *International Journal of Energy Research*, *45*(3), 4396–4409.

[35] **Raman, C. and Meneghetti, P.** (2008). Boron nitride finds new applications in thermoplastic compounds, *Plastics, Additives and Compounding*, *10*(3), 26–31.

[36] **Yuan, C.**, **Li, J.**, **Lindsay, L.**, **Cherns, D.**, **Pomeroy, J.W.**, **Liu, S.**, **Edgar, J.H. and Kuball, M.** (2019). Modulating the thermal conductivity in

hexagonal boron nitride via controlled boron isotope concentration, *Communications physics*, *2*(1), 43.

[37] **Zhou, W.**, **Zuo, J.**, **Zhang, X. and Zhou, A.** (2014). Thermal, electrical, and mechanical properties of hexagonal boron nitride–reinforced epoxy composites, *Journal of Composite Materials*, *48*(20), 2517–2526.

[38] **Okan, C.**, **Kaya, R.**, **Irez, A.B. and Cebe, E.** (2022). Effect of the Graphene Nanoplatelets (GnPs) on the Mechanical Properties in Recycled PP-Based Hybrid Composites, *Mechanics of Composite, Hybrid and Multifunctional Materials, Fracture, Fatigue, Failure and Damage Evolution, Volume 3: Proceedings of the 2021 Annual Conference on Experimental and Applied Mechanics*, Springer, pp.23–28.

[39] **Savadekar, N. and Mhaske, S.** (2010). The effect of vulcanized thermoplastics and SEBS on the impact strength of PPT, *Polymer-Plastics Technology and Engineering*, *49*(15), 1499–1505.

[40] **Gao, X.**, **Qu, C. and Fu, Q.** (2004). Toughening mechanism in polyoxymethylene/thermoplastic polyurethane blends, *Polymer international*, *53*(11), 1666–1671.

[41] **Ishak, Z.M.**, **Chow, W.**, **Takeichi, T.** *et al.* (2008). Influence of SEBS-g-MA on morphology, mechanical, and thermal properties of PA6/PP/organoclay nanocomposites, *European Polymer Journal*, *44*(4), 1023–1039.

[42] **Irez, A.B.**, **Okan, C.**, **Kaya, R. and Cebe, E.** (2022). Development of recycled disposable mask based polypropylene matrix composites: Microwave self-healing via graphene nanoplatelets, *Sustainable Materials and Technologies*, *31*, e00389.

[43] **Al-Maqdasi, Z.**, **Gong, G.**, **Nyström, B.**, **Emami, N. and Joffe, R.** (2020). Characterization of wood and Graphene Nanoplatelets (GNPs) reinforced polymer composites, *Materials*, *13*(9), 2089.

[44] **Suresha, B.**, **Hemanth, G.**, **Hemanth, R. and Lalla, N.** (2020). Role of graphene nanoplatelets and carbon fiber on mechanical properties of PA66/thermoplastic copolyester elastomer composites, *Materials Research Express*, *7*(1), 015325.

[45] **Seyhan, A.**, **Irez, A.B. and Polat, Y.** (2022). Development of a Polyamide 6-Based Composite Material for UAV Propellers, *Society for Experimental Mechanics Annual Conference and Exposition*, Springer, pp.73–77.

[46] **Sun, C.T. and Vaidya, R.S.** (1996). Prediction of composite properties from a representative volume element, *Composites science and Technology*, *56*(2), 171–179.

[47] **Wan, L.**, **Ismail, Y.**, **Zhu, C.**, **Zhu, P.**, **Sheng, Y.**, **Liu, J. and Yang, D.** (2020). Computational micromechanics-based prediction of the failure of unidirectional composite lamina subjected to transverse and in-plane shear stress states, *Journal of composite materials*, *54*(24), 3637–3654.

[48] **Mio, A. and Fermeglia, M.** (2022). Multiscale modelling techniques in Life Cycle Assessment: application to product design, *Procedia CIRP*, *105*, 688–693.

[49] **Orban, Y.A.**, **Manea, D.L. and Aciu, C.** (2018). Study of methods for simulating multiphase construction materials, *Procedia Manufacturing*, *22*, 256–261.

[50] **Biharta, M.A.S.**, **Santosa, S.P.**, **Widagdo, D. and Gunawan, L.** (2022). Design and optimization of lightweight lithium-ion battery protector with 3D auxetic meta structures, *World Electric Vehicle Journal*, *13*(7), 118.

[51] **Engler, M.**, **Lesniak, C.**, **Damasch, R.**, **Ruisinger, B. and Eichler, J.** (2007). Hexagonal boron nitride (hBN): applications from metallurgy to cosmetics, *CFI. Ceramic forum international*, volume 84, Göller.

[52] **Shokrieh, M.**, **Esmkhani, M.**, **Shahverdi, H. and Vahedi, F.** (2013). Effect of graphene nanosheets (GNS) and graphite nanoplatelets (GNP) on the mechanical properties of epoxy nanocomposites, *Science of Advanced Materials*, *5*(3), 260–266.

[53] **Nazari, B.**, **Ranjbar, Z.**, **Moghaddam, A.R.**, **Momen, G.**, **Ranjbar, B.** *et al.* (2019). Dispersing graphene in aqueous media: Investigating the effect of different surfactants, *Colloids and Surfaces A: Physicochemical and Engineering Aspects*, *582*, 123870.

[54] **Ka Wei, K.**, **Leng, T.P.**, **Keat, Y.C.**, **Osman, H.**, **Sullivan, M.**, **Hong, V.C.**, **Ying, L.B. and Rasidi, M.S.M.** (2021). Comparison study: The effect of unmodified and modified graphene nano-platelets (GNP) on the mechanical, thermal, and electrical performance of different types of GNP-filled materials, *Polymers for Advanced Technologies*, *32*(9), 3588–3608.

[55] **Irez, A.B.**, **Bayraktar, E. and Miskioglu, I.** (2019). Flexural fatigue damage analyses of recycled rubber-modified epoxy-based composites reinforced with alumina fibres, *Fatigue & Fracture of Engineering Materials & Structures*, *42*(4), 959–971.

[56] **Muratov, D.**, **Kuznetsov, D.**, **Il'Inykh, I.**, **Burmistrov, I. and Mazov, I.** (2015). Thermal conductivity of polypropylene composites filled with silane-modified hexagonal BN, *Composites Science and Technology*, *111*, 40–43.

[57] **Rasul, M.G.**, **Kiziltas, A.**, **Arfaei, B. and Shahbazian-Yassar, R.** (2021). 2D boron nitride nanosheets for polymer composite materials, *npj 2D Materials and Applications*, *5*(1), 56.

[58] **Madarvoni, S. and Sreekanth, R.P.** (2022). Mechanical characterization of graphene—hexagonal boron Nitride-Based kevlar–carbon hybrid fabric nanocomposites, *Polymers*, *14*(13), 2559.

[59] **Gul, S.**, **Arican, S.**, **Cansever, M.**, **Beylergil, B.**, **Yildiz, M. and Saner Okan, B.** (2022). Design of highly thermally conductive hexagonal boron nitride-reinforced PEEK composites with tailored heat conduction through-plane and rheological behaviors by a scalable extrusion, *ACS Applied Polymer Materials*, *5*(1), 329–341.

[60] **Saha, M.**, **Tambe, P.**, **Pal, S.**, **Kubade, P.**, **Manivasagam, G.**, **Anthony Xavior, M. and Umashankar, V.** (2015). Effect of non-ionic surfactant assisted modification of hexagonal boron nitride nanoplatelets on the mechanical and thermal properties of epoxy nanocomposites, *Composite Interfaces*, *22*(7), 611–627.

[61] **Bilisik, K. and Akter, M.** (2022). Polymer nanocomposites based on graphite nanoplatelets (GNPs): a review on thermal-electrical conductivity, mechanical and barrier properties, *Journal of Materials Science*, *57*(15), 7425–7480.

[62] **Inuwa, I.M.**, **Hassan, A.**, **Samsudin, S.A.**, **Mohamad Kassim, M.H. and Jawaid, M.** (2014). Mechanical and thermal properties of exfoliated graphite nanoplatelets reinforced polyethylene terephthalate/polypropylene composites, *Polymer Composites*, *35*(10), 2029–2035.

[63] **Irez, A.**, **Miskioglu, I. and Bayraktar, E.** (2018). Mechanical characterization of epoxy–scrap rubber based composites reinforced with nano graphene, *Mechanics of Composite and Multi-functional Materials, Volume 6: Proceedings of the 2017 Annual Conference on Experimental and Applied Mechanics*, Springer, pp.45–57.

[64] **Gao, Y.**, **Picot, O.T.**, **Bilotti, E. and Peijs, T.** (2017). Influence of filler size on the properties of poly (lactic acid)(PLA)/graphene nanoplatelet (GNP) nanocomposites, *European Polymer Journal*, *86*, 117–131.

[65] **Hu, K.**, **Kulkarni, D.D.**, **Choi, I. and Tsukruk, V.V.** (2014). Graphene-polymer nanocomposites for structural and functional applications, *Progress in polymer science*, *39*(11), 1934–1972.

[66] **Liang, J.Z.**, **Du, Q.**, **Tsui, G.C.P. and Tang, C.Y.** (2016). Tensile properties of graphene nano-platelets reinforced polypropylene composites, *Composites Part B: Engineering*, *95*, 166–171.

[67] **Nakhaei, M.R.**, **Naderi, G. and Ghoreishy, M.H.R.** (2021). Fracture mechanisms and failure analysis of PA6/NBR/graphene nanocomposites by essential work of fracture, *Iranian Polymer Journal*, *30*(9), 975–987.

[68] **Cui, S.**, **Wei, P. and Li, L.** (2018). Preparation of poly (propylene carbonate)/graphite nanoplates-spherical nanocrystal cellulose composite with improved glass transition temperature and electrical conductivity, *Composites science and technology*, *168*, 63–73.

[69] **Ma, J.**, **Meng, Q.**, **Zaman, I.**, **Zhu, S.**, **Michelmore, A.**, **Kawashima, N.**, **Wang, C.H. and Kuan, H.C.** (2014). Development of polymer composites

using modified, high-structural integrity graphene platelets, *Composites Science and Technology*, *91*, 82–90.

[70] **Irez, A.B.** (2024). Development of sunflower husk reinforced polypropylene based sustainable composites: An experimental investigation of mechanical and thermal performance, *Journal of Polymer Science*.

[71] **Pan, C.**, **Zhang, J.**, **Kou, K.**, **Zhang, Y. and Wu, G.** (2018). Investigation of the through-plane thermal conductivity of polymer composites with in-plane oriented hexagonal boron nitride, *International Journal of Heat and Mass Transfer*, *120*, 1–8.

[72] **Qiu, L.**, **Guo, P.**, **Zou, H.**, **Feng, Y.**, **Zhang, X.**, **Pervaiz, S. and Wen, D.** (2018). Extremely low thermal conductivity of graphene nanoplatelets using nanoparticle decoration, *ES Energy & Environment*, *2*(9), 66–72.

[73] **Yang, S.Y.**, **Ma, C.C.M.**, **Teng, C.C.**, **Huang, Y.W.**, **Liao, S.H.**, **Huang, Y.L.**, **Tien, H.W.**, **Lee, T.M. and Chiou, K.C.** (2010). Effect of functionalized carbon nanotubes on the thermal conductivity of epoxy composites, *Carbon*, *48*(3), 592–603.

[74] **Xiang, J. and Drzal, L.T.** (2011). Thermal conductivity of exfoliated graphite nanoplatelet paper, *Carbon*, *49*(3), 773–778.

[75] **Kalaitzidou, K.**, **Fukushima, H.**, **Miyagawa, H. and Drzal, L.T.** (2007). Flexural and tensile moduli of polypropylene nanocomposites and comparison of experimental data to Halpin-Tsai and Tandon-Weng models, *Polymer Engineering & Science*, *47*(11), 1796–1803.

[76] **İrez, A.B. and Kaya, R.** (2022). Geri Dönüştürülmüş PP Bazlı Nano Grafen Takviyeli Hibrit Kompozitlerin Geliştirilmesi ve Mekanik Özelliklerinin Mikromekanik Yöntemler ile Belirlenmesi, *International Journal of Advances in Engineering and Pure Sciences*, *34*(4), 569–579.

[77] **King, J.A.**, **Klimek, D.R.**, **Miskioglu, I. and Odegard, G.M.** (2013). Mechanical properties of graphene nanoplatelet/epoxy composites, *Journal of applied polymer science*, *128*(6), 4217–4223.

[78] **Mokoena, T.**, **Magagula, S.**, **Mochane, M. and Mokhena, T.** (2021). Mechanical properties, thermal conductivity, and modeling of boron nitride-based polymer composites: A review, *Express Polymer Letters*, *15*(12), 1148–1173.

[79] **Ahmadi-Moghadam, B. and Taheri, F.** (2014). Effect of processing parameters on the structure and multi-functional performance of epoxy/GNP-nanocomposites, *Journal of materials science*, *49*, 6180–6190.

[80] **Hoang, T.**, **Guerich, M. and Yvonnet, J.** (2016). Determining the size of RVE for nonlinear random composites in an incremental computational homogenization framework, *Journal of Engineering Mechanics*, *142*(5), 04016018.

[81] **Wu, H. and Kessler, M.R.** (2015). Multifunctional cyanate ester nanocomposites reinforced by hexagonal boron nitride after noncovalent biomimetic functionalization, *ACS applied materials & interfaces*, *7*(10), 5915–5926.

[82] **Cheng, S.C. and Vachon, R.** (1969). The prediction of the thermal conductivity of two and three phase solid heterogeneous mixtures, *International Journal of Heat and Mass Transfer*, *12*(3), 249–264.

[83] **Liu, L.**, **Feng, Y. and Shen, Z.** (2003). Structural and electronic properties of h-BN, *Physical Review B*, *68*(10), 104102.

[84] **Jahan, A.**, **Edwards, K. and Bahraminasab, M.** (2016). 6-Multiple objective decision-making for material and geometry design, *Multi-criteria decision analysis for supporting the selection of engineering materials in product design. Elsevier*, 127–146.

[85] **Kim, J.H. and Kim, Y.H.** (2002). Three-node macro triangular shell element based on the assumed natural strains, *Computational mechanics*, *29*(6), 441–458.

[86] **Akin, J.E.** (2010). *Finite element analysis concepts: via SolidWorks*, World Scientific.

[87] **Gürer, B.**, (2016), Investigating the effects of lightweight recycled bumper and chassis system on vehicle crashworthiness.

[88] **Panchal, S.**, **Mathew, M.**, **Fraser, R. and Fowler, M.** (2018). Electrochemical thermal modeling and experimental measurements of 18650 cylindrical lithium-ion battery during discharge cycle for an EV, *Applied Thermal Engineering*, *135*, 123–132.

[89] **Chen, H.**, **Zhang, D.**, **Chen, P.**, **Li, N. and Perrot, A.** (2023). A review of the extruder system design for large-scale extrusion-based 3D concrete printing, *Materials*, *16*(7), 2661.

[90] `https://www.mit.edu/~6.777/matprops/aluminum.htm`.

[91] **Wang, W.**, **Yang, S. and Lin, C.** (2017). Clay-like mechanical properties for the jellyroll of cylindrical Lithium-ion cells, *Applied energy*, *196*, 249–258.

[92] **Blind, N. and Östlund, R.**, (2009), Analysis of an engine frame subjected to large imbalance loads.

[93] **Dassault Systèmes, S.**, (2009), Abaqus/CAE User's Manual.

[94] **Voyer, J.**, **Klien, S.**, **Velkavrh, I.**, **Ausserer, F. and Diem, A.** (2019). Static and dynamic friction of pure and friction-modified PA6 polymers in contact with steel surfaces: influence of surface roughness and environmental conditions, *Lubricants*, *7*(2), 17.

[95] **Kulkarni, S.S.**, **Hale, F.**, **Taufique, M.**, **Soulami, A. and Devanathan, R.** (2023). Investigation of crashworthiness of carbon fiber-based electric vehicle battery enclosure using finite element analysis, *Applied Composite Materials*, *30*(6), 1689–1715.

APPENDICES

APPENDIX A: Stress-Strain curves of compositions

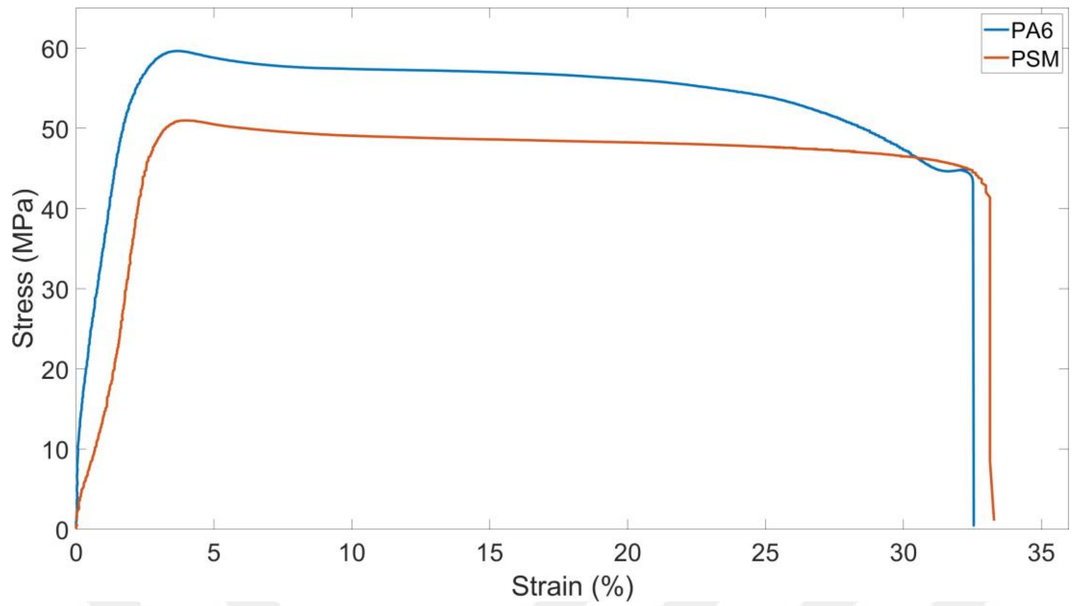

Figure A.1 : Stress-Strain curves of PA6 and PSM

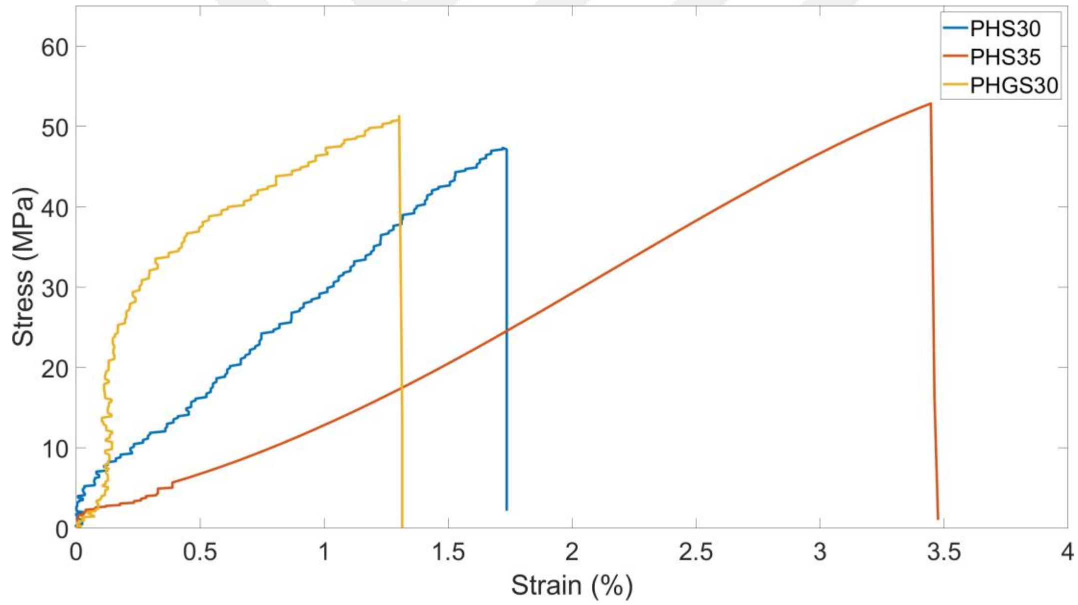

Figure A.2 : Stress-Strain curves of PHS30, PHS35, PHGS30

APPENDIX B: DSC results of PSM, PHS30, and PHGS30 compositions

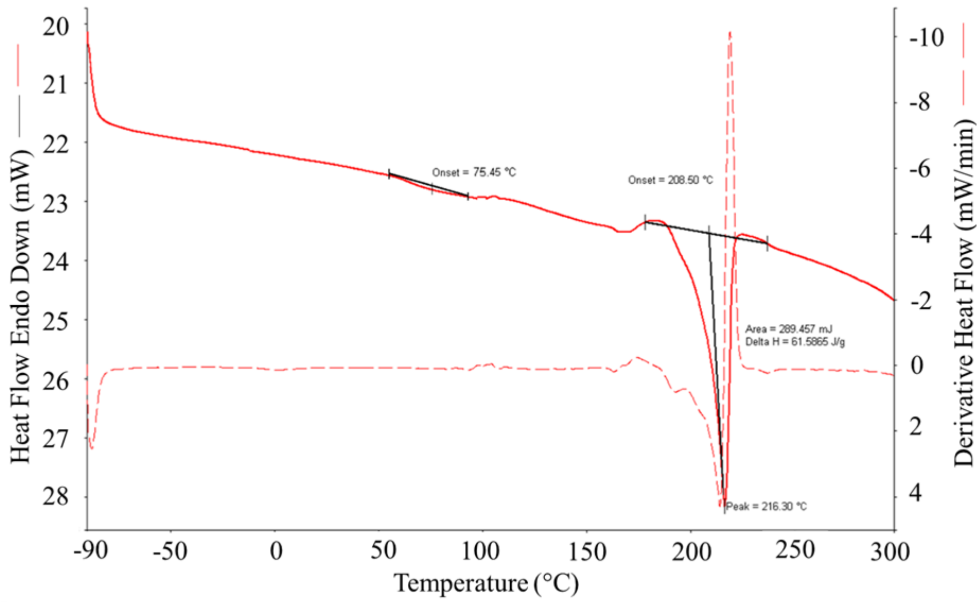

Figure B.1 : DSC results of PA6

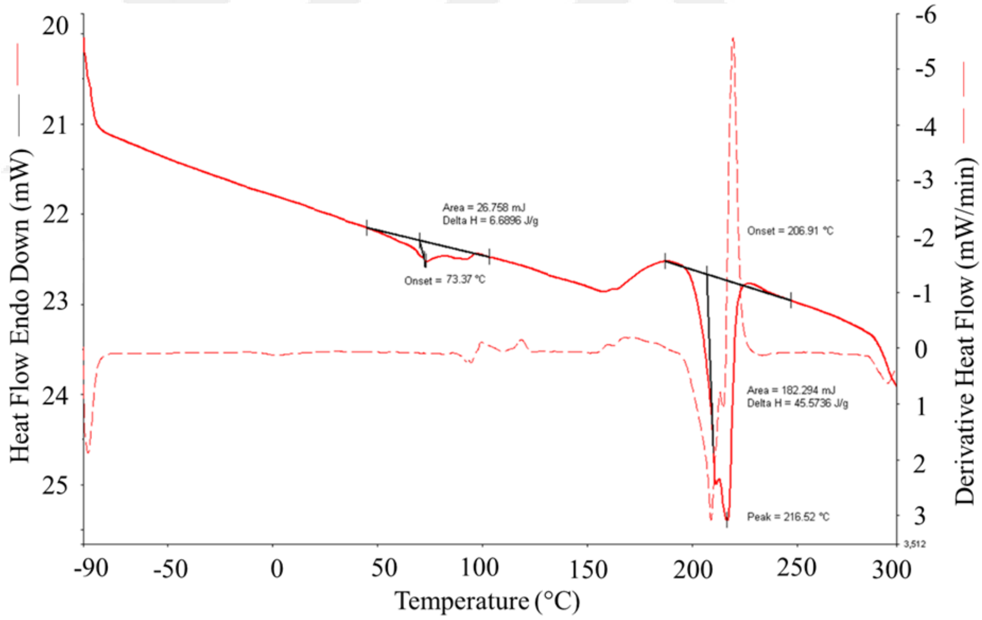

Figure B.2 : DSC results of PSM

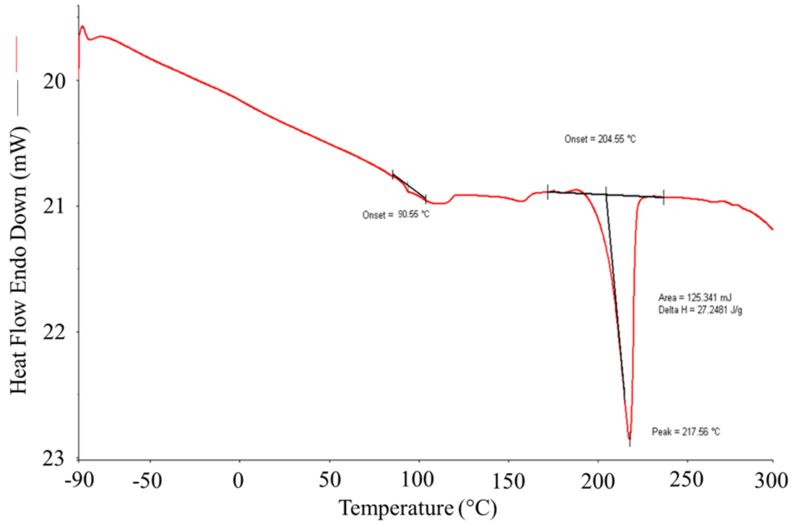

Figure B.3 : DSC results of PHS30

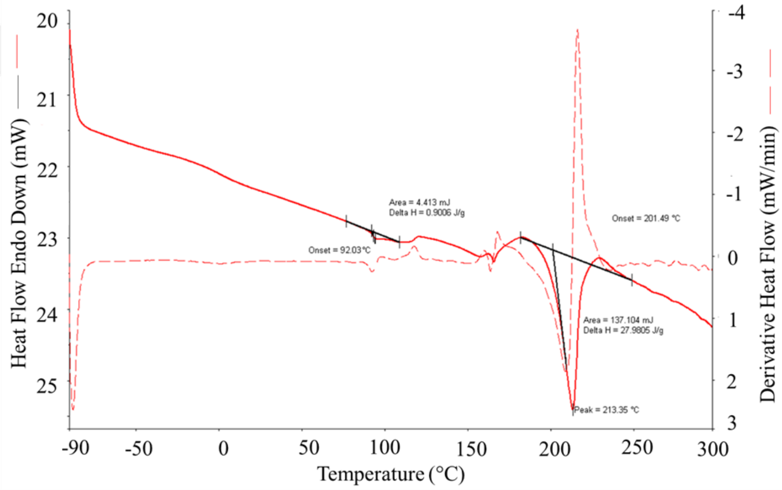

Figure B.4 : DSC results of PHS35

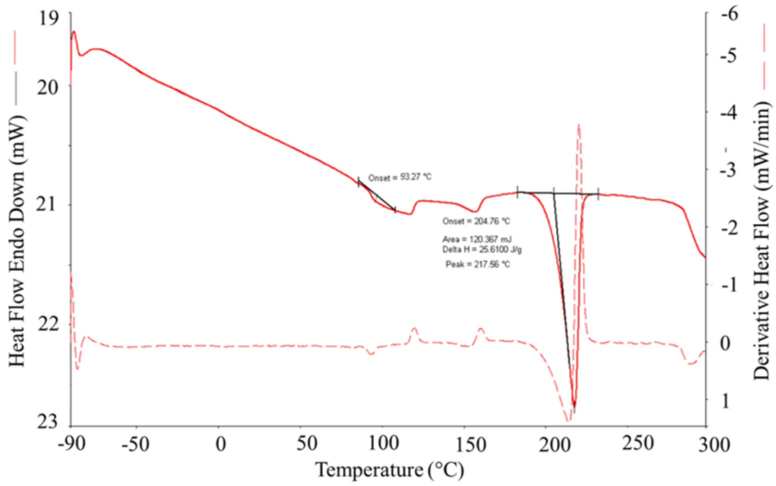

Figure B.5 : DSC results of PHGS30

APPENDIX C : Python based optimization code

```
from tkinter import Tk, Frame, Label, Entry,
Button,
StringVar, DoubleVar, ttk, Menu, messagebox from
matplotlib.backends.backend_tkagg import
FigureCanvasTkAgg import matplotlib.pyplot as plt
class ScoringApp:
definition(self): self.window = Tk()
self.window.title("Scoring Program")
self.window.configure(bg="white") self.a = 0
self.b = 0 self.parameters = [] self.materials =
[]
self.coefficientfactor = [] self.values = [[]]
self.dict = {}
self.entry_dict = {} self.result = []
self.selected_values = [] self.create_widgets()
def merge(self, list):
new_lists = [[] for _ in range(len(list[0]))] for
subset in list:
for i, e in enumerate(subset):
new_lists[i].append(e)
return new_lists
def calculations(self):
self.result = []
self.deger2 = [[] for _ in
range(len(self.parameters))] try:
for x in range(len(self.parameters)):
for y in range(len(self.materials)):
multiplied_value =
self.values[x + 1][y]/sum(self.values[x + 1])
self.deger2[x].append(multiplied_value) except
ZeroDivisionError:
messagebox.showerror("ERROR", "Zero Division
Error") return
lastlist = [] o = 0
for val1, b in zip(self.coefficientfactor,
self.deger2):
sublist =[]
for i, x in enumerate(b):
if self.selected_values[o] == "max":
multiplied_value = val1 * x
elif self.selected_values[o] == "min":
multiplied_value = val1 * (1 - x)
sublist.append(multiplied_value)
lastlist.append(sublist)
o += 1
new_lists2 = self.merge(lastlist)
print("new list:", new_lists2)
```

```
new_lists2 = self.merge(lastlist)
print("new list:", new_lists2)
for h in range(len(new_lists2)):
self.result.append(sum(new_lists2[h]))
print(self.result)
self.plot_results()
def calculate(self):
self.parameters.clear()
self.materials.clear()
self.coefficientfactor.clear()
self.values.clear()
for i in range(4 + self.b):
for j in range(4 + self.a):
if i == 2 and j > 0:
self.dict[(i, j)] = self.entry_dict[(i, j)].get()
self.selected_values.append(self.dict[(i, j)])
elif i > 2 and j == 0:
self.dict[(i, j)] = self.entry_dict[(i, j)].get()
self.materials.append(self.entry_dict[(i, j)].get())
elif i == 0 and not j == 0:
self.dict[(i, j)] = self.entry_dict[(i, j)].get()
self.parameters.append(self.entry_dict[(i, j)].get())
elif i == 1 and not j == 0:
value = self.entry_dict[(i, j)].get()
self.dict[(i, j)] = float(value) if value != "" else None
self.coefficientfactor.append(self.dict[(i, j)])
elif i > 0 and j > 0 and i != 2:
value = self.entry_dict[(i, j)].get()
self.dict[(i, j)] = float(value) if value != "" else None
while len(self.values) <= j:
self.values.append([])
self.values[j].append(self.dict[(i, j)])
if len(self.values) < len(self.materials):
self.values.append([])
print("Parameters:", self.parameters)
print("Materials:", self.materials)
print("Coefficient Factors:", self.coefficientfactor)
print("Values:", self.values)
def printit(self):
self.calculate()
self.calculations()
def create_widgets(self):
yazi = Frame(self.window)
yaziic = Label(yazi, text="Success Comparison Table")
yaziic.grid(row=0, column=0, pady=40, padx=40)
Table = Frame(self.window, bg="white", width=200, height=100)
Table.grid(row=1, column=0, pady=40, padx=40) for i
in range(4 + self.b):
```

```
for j in range(4 + self.a):
if i == 0 and j == 0:
t2 = Label(Table, text="Parameters", fg="black",
background="white")
t2.grid(row=0, column=0)
if i == 1 and j == 0:
t3 = Label(Table, text="Coefficient Factors", fg="black",
background="white")
t3.grid(row=1, column=0)
elif i == 2 and j > 0:
combo = ttk.Combobox(Table,
values=["max", "min"], height=50, justify="center",
state="readonly")
combo.grid(row=i, column=j)
self.entry_dict[(i, j)] = combo
elif i > 2 and j == 0:
STR3 = StringVar()
e = Entry(Table, width=20, borderwidth=5,
textvariable=STR3,
insertbackground="black", fg="black")
e.grid(row=i, column=j)
self.entry_dict[(i, j)] = STR3
elif i == 0 and not j == 0:
STR4 = StringVar()
e = Entry(Table, width=20, borderwidth=5,
textvariable=STR4,
fg="black", background="white")
e.grid(row=i, column=j)
self.entry_dict[(i, j)] = STR4
elif i == 1 and not j == 0:
STR5 = DoubleVar()
e = Entry(Table, width=20, borderwidth=5,
textvariable=STR5,
fg="black", background="white")
e.grid(row=i, column=j)
self.entry_dict[(i, j)] = STR5
elif i == 2 and j == 0:
t = Label(Table, text="materials|increase", fg="black",
background="white")
t.grid(row=2, column=0, padx=2, pady=2)
elif i > 0 and j > 0 and i != 2:
STR6 = DoubleVar()
e = Entry(Table, width=20, borderwidth=5, textvariable=STR6,
fg="black", background="white")
e.grid(row=i, column=j)
self.entry_dict[(i, j)] = STR6
plus = Button(Table, text="+", command=self.inccolumn,
```

```
borderwidth=2,
background="white", fg="black")
plus.grid(row=0, column=j + 1)
plus2 = Button(Table, text="+", command=self.incrow,
borderwidth=2,
background="white", fg="black")
plus2.grid(row=i + 1, column=0)
submit = Button(Table, text="calculate",
command=self.printit,
background="yellow", activebackground="#987654")
submit.grid(row=i + 1, column=j + 1)
submit2 = Button(Table, text="clear", command=self.new,
background="yellow", activebackground="#987654")
submit2.grid(row=i + 1, column=j + 2)
def inccolumn(self):
self.materials.clear()
self.parameters.clear()
self.coefficientfactor.clear()
self.values.clear()
self.a += 1
self.create_widgets()
def incrow(self):
self.materials.clear()
self.parameters.clear()
self.coefficientfactor.clear()
self.values.clear()
self.b += 1
self.create_widgets()
def new(self):
self.create_widgets()
def plot_results(self):
fig, (ax1, ax2) = plt.subplots(1, 2, figsize=(10, 4))
ax1.pie(self.coefficientfactor, labels=self.parameters,
autopct='%1.1f%%', startangle=90)
ax1.set_title("Coefficient Ratio")
if len(self.materials) < len(self.result):
self.materials.extend(["" for _ in
range(len(self.result) - len(self.materials))])
ax2.bar(self.materials, self.result, color='red')
ax2.set_title("success score")
ax2.set_ylim(min(self.result) - 5,
max(self.result) + 5)
plt.show()
def run_app(self):
menu = Menu(self.window, activebackground="blue",
activeforeground="white", activeborderwidth=5,
bg="darkgray", fg="green")
menu.config(bd=3, font="helvetica 12") def
run_new():
```

```
self.window.quit()
ScoringApp().run_app()
self.window.config(menu=menu)
file_menu = Menu(menu, tearoff=0)
menu.add_cascade(label="File", menu=file_menu)
file_menu.add_command(label="Close",
command=self.window.quit, activeforeground="red")
file_menu.add_command(label="New",
command=run_new, activeforeground="red")
self.window.mainloop()
if __name__ == "__main__":
app = ScoringApp()
app.run_app()
\end{minted}
```

CURRICULUM VITAE

Name Surname : Emrullah Cebe

EDUCATION :

- **B.Sc.** : 2021, Istanbul Technical University, Faculty of Mechanical Engineering, Department of Manufacturing Engineering

PUBLICATIONS, PRESENTATIONS AND PATENTS ON THE THESIS:

- **Cebe, E. Irez, A. (2023).** Development of Thermally Improved Hybrid Composites for Electric Car Battery Cases. International Graduate Research Symposium – IGRS'23, May 16-18, 2023 Istanbul, Turkey. (Presented)

- **Cebe, E., İrez, A. B. (2024).** Elektrikli Araçlarda Batarya Kutusu İmali İçin Termal Özellikleri İyileştirilmiş Hibrit Polimer Kompozitlerin Geliştirilmesi ve Mekanik Özelliklerinin İncelenmesi. International Journal of Advances in Engineering and Pure Sciences. https://doi.org/10.7240/jeps.1464667 (Accepted for publication)

- **Cebe, E., İrez, A. B. (2024).** Thermal Performance Improved Hybrid Polymer Composites Development for Battery Module Case Manufacturing in Electric Vehicles. Polymer Composites. (Under review)

- **Cebe, E., İrez, A. B., Kalbaran Ö. (2024).** Development of Hybrid Polymer Composites with Honeycomb Structure for Battery Module Case in Electric Vehicles: a Ground Impact Simulation (Under review)